Heinz - Hermann Adam

Hadronic ^{3}He-η production near threshold

2009

Experimentelle Physik

Hadronic ^{3}He-η production near threshold

Inaugural-Dissertation zur Erlangung des Doktorgrades der Naturwissenschaften
im Fachbereich Physik der Mathematisch-Naturwissenschaftlichen Fakultät der
Westfälischen Wilhelms-Universität Münster

vorgelegt von

Heinz-Hermann Adam

aus Münster

- 2009 -

Dekan:	Prof. Dr. Johannes Wessels
Erster Gutachter:	Priv.-Doz. Dr. Alfons Khoukaz
Zweiter Gutachter:	Prof. Dr. Rainer Santo
Tag der mündlichen Prüfung(en):	8. Mai 2009
Tag der Promotion:	8. Mai 2009

To Richard Glasow,
whose seemingly endless experience and knowledge was the greatest source of inspiration, not only when thinking about the next generation of IT.

Table of contents

1 Abstract

Close-to-threshold data on the pd $\rightarrow$ ^{3}He η reaction are of great interest for studying the strong η–nucleus final state interaction (FSI) at low energies. The possibility to find bound states of a η–^{3}He system requires indepth knowledge of the characteristics of such an η–^{3}He system. The η–^{3}He system produced close to the pd $\rightarrow$ ^{3}He η reaction threshold is ideally suited to study the interaction between η and the ^{3}He. They are produced at almost rest in the center-of-mass system (c.m.s.), making them especially sensitive to FSI effects. To study the FSI effects, additionally a robust understanding of the production reaction itself and its special features is necessary.

As observed close to threshold at the SPES-IV and SPES-II spectrometers at the Saturne laboratory, the η-production cross section in the pd $\rightarrow$ ^{3}He η reaction reveals remarkable features. In addition to the unexpectedly large cross section for this channel, which is in the order of that of pd $\rightarrow$ ^{3}He π^0, the excitation function has a maximum very close to the production threshold. The production amplitude then drops significantly with increasing energy within only a few MeV, which is in complete contrast to expectations based upon phase space. Furthermore, the center-of-mass angular distributions of the η mesons emitted near threshold were reported to be consistent with s-wave production and exhibit no major contributions from higher partial waves. This behavior differs from the corresponding data on the π^0-production cross section, where a strong p-wave contribution is present even very close to threshold.

In order to describe this near-threshold behavior, a classical two-step mechanism was proposed by Kilian and Nann. Quantum mechanical calculations by Fäldt and Wilkin within this model succeeded in reproducing the square of the production amplitude at threshold to within a factor of 2.5. To achieve this level of accuracy, they had to include a strong η–^{3}He final state interaction (FSI) into their model calculation, to describe the observed rapid drop of the production amplitude with increasing energy.

Further measurements, performed at a higher excess energy of Q ~40 MeV by the COSY-GEM collaboration, yielded a highly nonisotropic angular distribution. The two-step/FSI description for the close to threshold data significantly underestimates the value of the total cross section for that measurement. Therefore, a different reaction mechanism, based on the excitation of the $N^*(1535)$ resonance has been suggested. However, this model prediction, scaled to fit the COSY-GEM data point, fails to reproduce the observed shape of the previously determined excitation function in the near-threshold region. Additional studies have also been carried out by the WASA/PROMICE collaboration at η excess energies between Q ~22 MeV and

Q ~120 MeV, yielding anisotropic angular distributions for all their measurements, in agreement with the GEM results. However the total cross sections determined in that measurement can neither be described by the η–^{3}He FSI nor the predicted shape of the resonance model excitation function.

The lack of data in the range of intermediate excess energies impedes any further experimental and theoretical studies to develop a consistent reaction model of the underlying production processes in the pd $\rightarrow$ ^{3}He η reaction. As long as this gap in the excitation function has not been closed and no additional differential cross sections for this region of excess energies are available no progress in the investigation of the pd $\rightarrow$ ^{3}He η is possible.

Measurements of η meson production in proton-deuteron collisions have therefore been performed using the COSY-11 facility at COSY (Jülich). Results on total and differential cross sections for the pd $\rightarrow$ ^{3}He η reaction are presented at five excess energies between Q_η = 5.0 and Q_η = 40.6 MeV. This measurement closes the gap between earlier measurements very close to threshold up to Q_η = 6 MeV, carried out by SPES-II and -IV experiments at Saturne in Saclay and measurements by COSY-GEM (Q_η = 40.3 MeV) and WASA/PROMICE above Q_η = 21.7 MeV. The angular distributions show a transition from an almost isotropic emission close to threshold, as observed in the SPES-II measurements, to a highly anisotropic distribution at higher excess energies, as observed by COSY-GEM. The total cross sections reveal a strong η–^{3}He final state interaction, corresponding to a scattering length of $|\Re(a)|$ = (4.2 ± 0.5) fm and $\Im(a)$ = (0.4 ± 1.9) fm.

1.1 German

Schwellennahe Messungen der Reaktion pd $\rightarrow$ ^{3}He η sind von besonderem Interesse, um die starke η–Kern Endzustandswechselwirkung (final-state-interaction: FSI) bei niedrigen relativ Energien untersuchen zu können. Um in der Lage zu sein gebundene Zustände eines η–^{3}He Systemen zu finden, ist die genaue Kenntniss der Eigenschaften eines solchen Systems vonnöten. Das in der Reaktion pd $\rightarrow$ ^{3}He η schwellennah produzierte η–^{3}He ist das ideale Studienobjekt für die Wechselwirkung von η und ^{3}He. Durch die geringe relativ Geschwindgikeit der Ejektile, die sich im Schwerpunktssystem nahezu in Ruhe zu einander befinden, ist das System besonders empfindlich für FSI-Effekte. Um die FSI-Effekte untersuchen zu können, ist wiederum ein gutes Verständnis der Produktionsreaktion selbst und ihrer Eigenarten notwendig.

Wie zuerst an den SPES-IV und SPES-II Spektrometern am Saturne Labor festgestellt wurde, hat der Wirkungsquerschnitt der pd $\rightarrow$ ^{3}He η-Produktion bemerkenswerte Eigenschaften.

Neben dem unerwartet hohen Wirkungsquerschnitt für diese Reaktion, der in der Größenordnung der Rektion pd $\rightarrow$ ^{3}He π^0 liegt, hat die Anregungsfunktion ein Maximum sehr nahe an der Produktionsschwelle und fällt zu höheren Anregungsenergie hin innerhalb weniger MeV stark ab. Dies weicht deutlich von einem Phasenraumverhalten ab. Desweiteren wurde berichtet, dass die Winkelverteilung der produzierten η-Mesonen im Schwerpunktssystem einem s-Wellenverhalten entspricht und keine wesentlichen Beiträge höherer Partialwellen beobachtet wurden. Im Fall der pd $\rightarrow$ ^{3}He π^0-Produktion war bereits sehr nahe der Produktionsschwelle ein wesentlicher Beitrag von p-Wellen festgestellt worden.

Um das besondere schwellennahe Verhalten bei der pd $\rightarrow$ ^{3}He η-Produktion zu beschreiben haben Kilian und Nann einen klassischen Zwei-Stufen-Mechanismus vorgeschlagen. Quantenmechanische Berechnungen von Fäldt und Wilkin innerhalb dieses Modells konnten das Quadrat der Produktionsamplitude an der Schwelle bis auf einen Faktor 2,5 reproduzieren. Um eine gute Beschreibung der Energieabhängigkeit zu erreichen, mussten sie zusätzlich eine starke η–^{3}He Endzustandswechselwirkung (final-state-interaction: FSI) in ihre Modellrechnungen aufnehmen.

Weitere Messungen oberhalb der Produktionsschwelle bei einer Anregungsenergie von Q ~40 MeV wurden von der COSY-GEM-Kollaboration durchgeführt, hierbei zeigte sich eine stark anisotrope Winkelverteilung. Die Zwei-Stufen/FSI-Beschreibung der schwellennahen Messungen sagt den absoluten Wirkungsquerschnitt bei so hohen Anregungsenergien wesentlich zu niedrig voraus. Daher wurde ein anderer Reaktionsmechnismus, basierend auf der Anregungen der $N^*(1535)$ Resonanz vorgeschlagen. Dieses Modell ist allerdings nur in der Lage die COSY-GEM Messung zu beschreiben für die es entwickelt wurde, nicht jedoch den Verlauf der Anregungsfunktion nahe der Schwelle.

Weitere Untersuchungen der WASA/PROMICE Kollaboration haben gezeigt, dass anisotrope Winkelverteilungen bei Anregungsenergien zwischen Q ~22 MeV und Q ~120 MeV zu finden sind und bestätigen diesen Teil der COSY-GEM Ergebnisse. Allerdings stimmen die ermittelten absoluten Wirkungsquerschnitte weder mit den FSI noch den Resonanz Vorhersagen überein.

Ohne weitere Informationen zum Verhalten bei mittleren Anregungsenergien, sind weder experimentelle noch theoretische Arbeiten zur Untersuchung des der Reaktion pd $\rightarrow$ ^{3}He η zu Grunde liegenden Prozesses möglich oder sinnvoll. Erst wenn die Lücke zwischen den schwellennahen und schwellenfernen Messungen geschlossen ist und differentielle Wirkungsquerschnitte für diesem Energiebereich vorliegen, wird ein Fortschritt bei der Untersuchung von pd $\rightarrow$ ^{3}He η möglich sein.

Hierzu haben Messungen der η-Mesonenproduktion in Proton-Deuteron-Kollision am COSY-11 Experimentierplatz des COSY-Beschleunigers in Jülich stattgefunden. Die Ergebnisse dieser Arbeit, absolute und differenzielle Wirkungsquerschnitte der Reaktion pd $\rightarrow$ ^{3}He η

bei fünf verschiedenen Anregungsenergien zwischen Q_η = 5,0 und Q_η = 40,6 MeV, werden hier vorgestellt. Dadurch wird die Lücke zwischen den sehr schwellennahen Messungen bis zu Q_η = 6 MeV (SPES-II/IV) und den recht schwellenfernen Messungen ab Q_η = 40,3 MeV (COSY-GEM) und Q_η = 21,7 MeV (WASA/PROMICE) geschlossen.

Die Winkelverteilung zeigt dabei einen Übergang von einer vorwiegend isotropen Emission bei den schwellennäheren Messungen, wie auch bei SPES-II, zu einer stark anisotropen Verteilung bei den weiter von der Schwelle entfernten Messungen, ähnlich wie bei COSY-GEM.

Der Verlauf des absolute Wirkungsquerschnitt in der Anregungsfunktion bestätigt eine starke η–^{3}He Endzustandswechselwirkung, es wurde eine Streulänge von $|\Re(a)| = (4{,}2 \pm 0{,}5)$ fm und $\Im(a) = (0{,}4 \pm 1{,}9)$ fm bestimmt.

2 Introduction

2.1 Motivation

2.1.1 First measurements at SPES-II

Early measurements [1] of the dp $\rightarrow$ ^{3}He η reaction at SPES-IV, which were foreseen to be utilized as a ^{3}He-tagged η beam source to investigate rare η decays at the Laboratoire National Saturne at Saclay, France, revealed an unexpectedly large cross section close to the production threshold at 0° in the laboratory [2]. The magnitude of the cross section was thought of to be surprising by that time, as the studies where carried out with the results from similar studies on the dp $\rightarrow$ ^{3}He π^0 reaction [3] in mind.

The η plays a much smaler role in nuclear physiscs than the π, due to its a four times larger mass and weaker coupling constant. It was therefore expected, that the threshold amplitude f_η (Eq. 2.1) is not as strong as for η-production, as it is for the corresponding π^0 reaction at its threshold. However, despite this and the much larger momentum transfer associated with the η reaction, the magnitude is very similar for η and π [4].

The π^0 and the η mesons, identical in spin-parity and only different in isospins (Fig. 2.2, Tab. 2.1), were however expected to exhibit similar behaviour in other aspects, if the same pion exchange process is applicable. In this process (Fig. 2.1), a pion is emitted by one nucleon and then rescattered by a second before emerging.

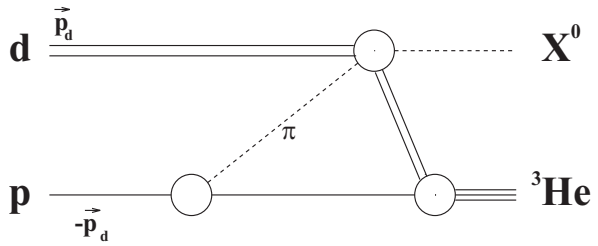

Figure 2.1 One-pion exchange process in a proton deuteron reaction. The pion (π) is emitted by one nucleon (p)and then rescattered by a second (d) before emerging (X^0).

While both excitation functions are vanishing at threshold, the forward-backward cross section ratio remains close to 1 for the η, but the π^0 data soon display a very asymetric behaviour. For the η-production, this isotropic emission of the reaction ejectiles means, that the production

process ist dominated by s-wave close to the production threshold and the contribution of higher partial waves, e.g. d-waves, is negligible. For the π-production however, d-waves contribute significantly to the process, already close to the production threshold. When further looking into the deuteron tensor analyzing power, the two-body process with a pure S-state nuclear wave function, as observed in experiment, would lead to a value $t_{20} = -\sqrt{2}$, while it was actually determined to be -1.3 ± 0.02 [1]. That in turn would only be reproducible inside the one-pion exchange model, if D states, unobserved in experiment, are incorporated.

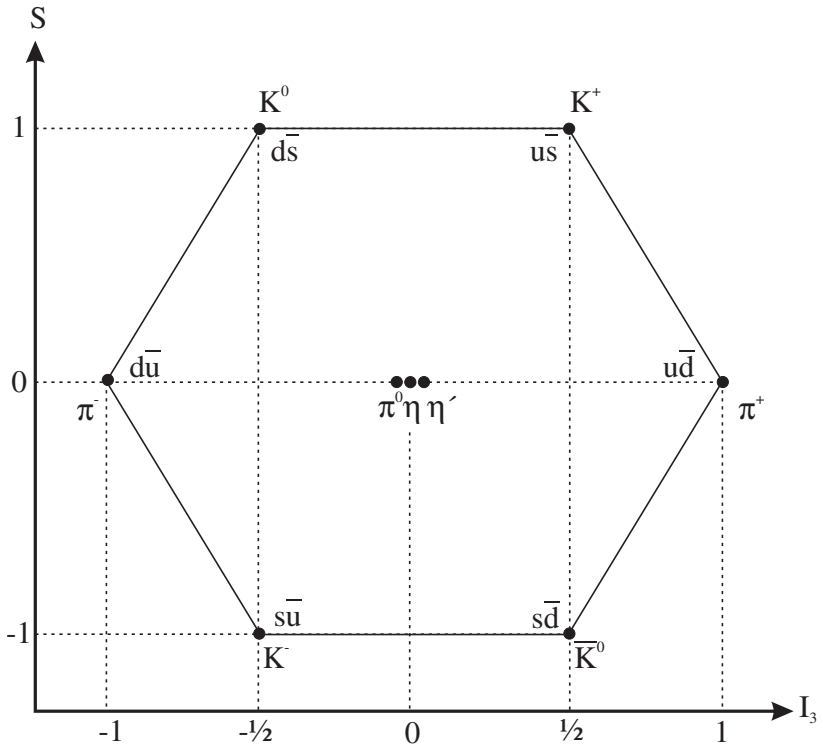

Figure 2.2 SU(3)-nonet of pseudo-scalar mesons. Presented are the quantum numbers of strangeness content (ordinate) and the 3-component of the isospin (abscissa) of the pseudo-scalar mesons, as well as their quark content. For the π^0, η and η' the $q\bar{q}$ quark content is omitted from the presentation

	J^P	I	I_3	S	C
π^0	0^-	1	0	0	+1
η	0^-	0	0	0	+1

Table 2.1 Quantum numbers of π^0 and η mesons. J: spin, P: parity, I: isospin, I_3: 3-component of isospin, S: strangeness, C: charge parity

Therefore a different production mechanism than the one-pion exchange model, had to be introduced to describe the observed behaviour. Due to the large mass of the η, engendering a high-momentum transfer, a three-nucleon process had to be taken into account.

Although the results of [1] showed, that the dp → ^{3}He η reaction close to threshold was an ideal, almost background free source for a ^{3}He-tagged η beam, the reaction itself became of higher interest due to its remarkable features.

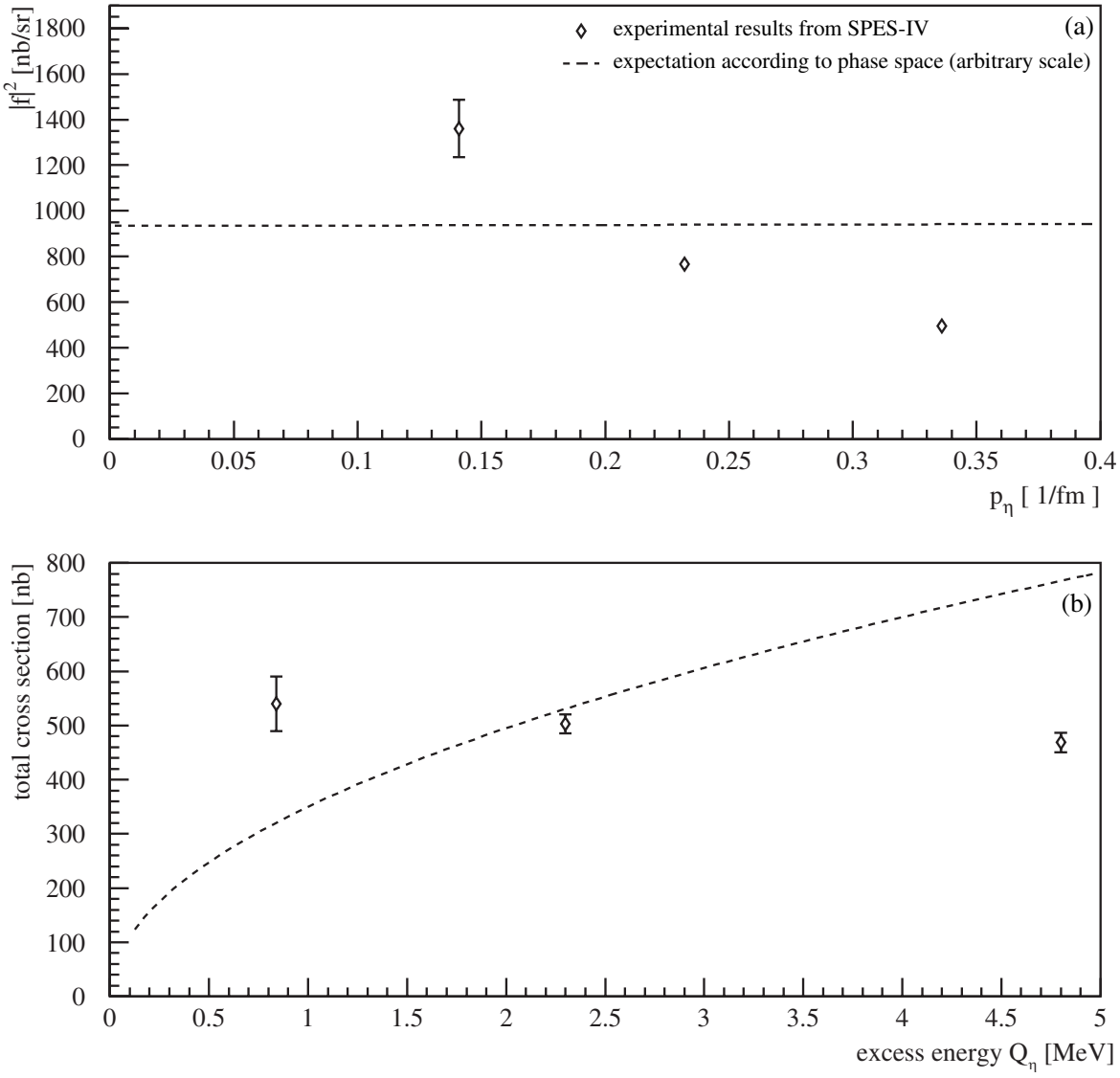

Figure 2.3 Excitation function of the dp → ^{3}He η reaction measured at SPES-IV presented as production amplitude and total cross section plot. (a) Production amplitude $|f|^2$. Within an energy interval corresponding to only a few MeV above the η production threshold, the production amplitude drops by more than a factor of 1:2. The η-momentum is presented in the commonly used 1/fm units, rather than in MeV. The conversion is done by h c = 197 MeV fm with natural units h = c = 1. (b) Total cross section. The shape of the excitation function in both presentations differs significantly from expectations based upon phase space (dashed line, arbitrary scale).

Primarily due to a maximum in the excitation funtion very close to the production threshold (Fig. 2.3) and a following significant drop of the production amplitude within a few MeV (Fig. 2.3, a), in complete contrast to expectations based upon phase space (Fig. 2.3, dashed lines), much interest was put into the pd → ^{3}He η production mechanism.

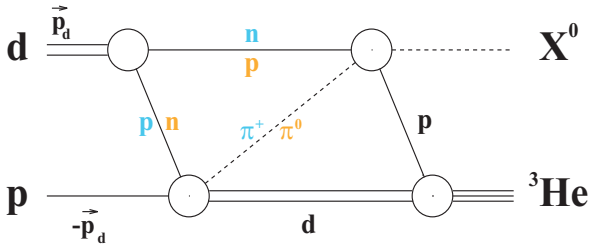

Figure 2.4 Double-scattering diagram for pd → ^{3}He η in terms of the constitutent pp → dπ$^+$ and π$^+$n → ηp amplitudes (blue). There is a similar diagram involving an intermediate π^0 meson in the constituents np → dπ^0 and π^{0}p → ηp (orange).

2.1.2 Two-step mechanism

A classical two-step mechanism was proposed by Kilian and Nann [5] (Fig. 2.4) to describe the near-threshold behaviour. In this model the beam proton interacts with a proton (blue) or neutron (orange) of the target deuteron, producing a virtual pion and a deuteron, in the first step (Tab. 2.2, Step 1). In the second step the virtual pion induces the formation of the η meson on the neutron or proton, leaving a proton (Tab. 2.2, Step 2) for the formation of the ^{3}He by fusing with the residual deuteron from the first step.

	virtual π$^+$ exchange								virtual π^0 exchange							
Step 1	p	+	p	→	d	+	π$^+$		p	+	n	→	d	+	π^0	
Step 2	π$^+$	+	n	→	p	+	η		π^0	+	p	→	p	+	η	
Total	**p**	**+**	**d**	**→**	**^{3}He**	**+**	**η**		**p**	**+**	**d**	**→**	**^{3}He**	**+**	**η**	

Table 2.2 Double scattering process for the pd → ^{3}He η reaction in terms of the constitutent pion exchange reactions presented in Fig. 2.4.

They refered to the kinematics of the total reaction as „magic“, in the sense that for zero Fermi momenta for both the ^{3}He and deuteron nucleus, the intermediate pion is close to its mass shell [6].

2.1.3 More in-depth studies of the close to threshold behaviour at SPES-II

Further studies at SPES-II [2], also at Saturne, in the near-threshold region have been carried out not only to investigate the excitation function, but also the partial waves contributing to the reactions process, visible in the angular distribution of the emitted ^{3}He (Fig. 2.5).

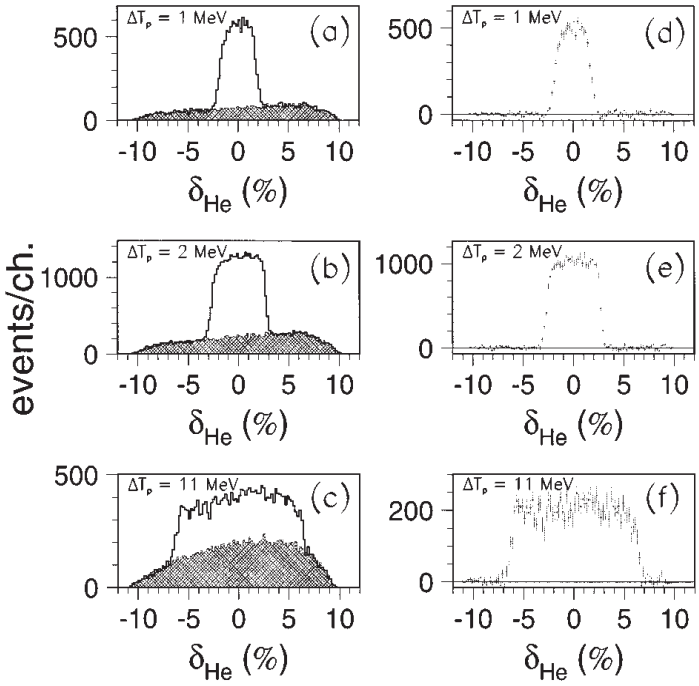

Figure 2.5 Fig. 4 taken from [2]: Angular distribution of the emitted ^{3}He nuclei as function of the normalized ^{3}He momentum δ_{He} (~ cos θ) for three of the eight measured data points (highest and second and third lowest). The δ_{He} spectra are flat over the range of measured beam energies, reflecting an isotropic angular distribution in the center-of-mass system. Data from three different beam energies ΔT_p are presented, one in each row of the figure. (a)-(c) present δ_{he} spectra without background subtraction. In grey a subthreshold measurement, scaled to fit the respective above threshold measurement outside the ^{3}He peak is shown. (d)-(f) present the same spectra after the background subtraction has been performed.

Besides confirmation of the earlier findings at SPES-IV, the more detailed measurements of SPES-II not only added additional data to the excitation function (Fig. 2.6), but also revealed a pure s-wave production in the range of investigated proton energies up to 11 MeV above the reaction threshold. The flat-top found in the spectra of the angular dependend analysis (Fig. 2.5) corresponds to a flat, isotropic angular distribution of the emitted ^{3}He (δHe ~ cosθ), neglecting major contributions of higher partial waves.

In earlier studies of the pd $\rightarrow$ ^{3}He π^0 reaction it was found, that p-wave components contribute significantly to the production process already close to threshold [7], which is not the case for the otherwise similar η reaction.

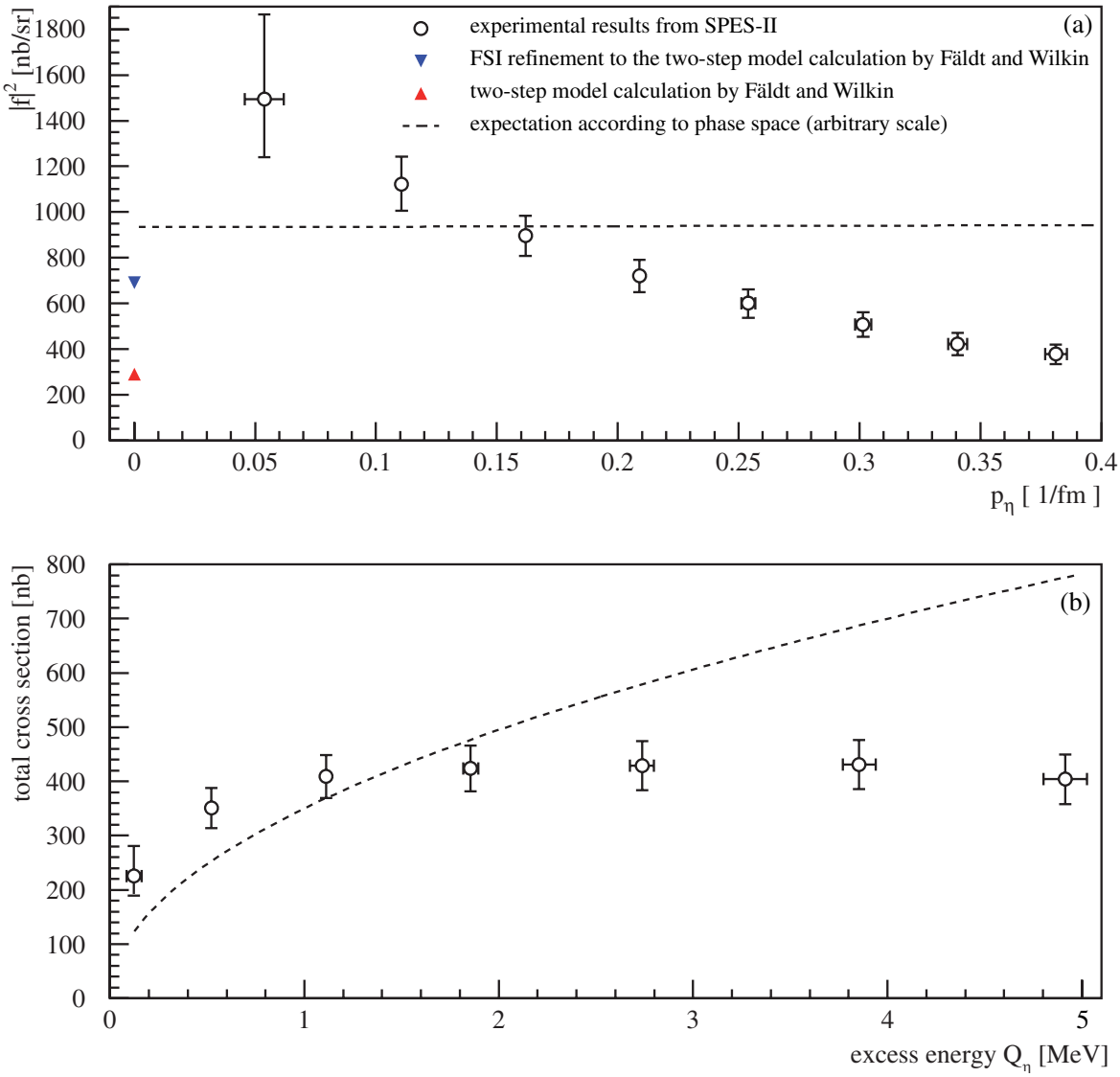

Figure 2.6 Excitation function of the dp → ^{3}He η reaction measured at SPES-II presented as production amplitude and total cross section plot. (a) Production amplitude $|f|^2$. Besides the experimental data [2] shown as open circles, also predictions from model calculation [8] are included as red and blue triangles. For a description of the different model calculation values see section 2.1.4 (b) Total cross section. After a steep rise close to threshold the total cross section reaches a maximum and then drops slightly. The expectations based upon phase space are indicated as a dashed line, the scale is arbitrary.

2.1.4 Final-State-Interaction (FSI)

Quantum mechanical calculations by Fäldt and Wilkin [8] within the two-step model succeeded in reproducing the square of the production amplitude at threshold to within a factor of 5.5 predicting $|f|^2$= 290 nb/sr (Fig. 2.6, red triangle). The production amplitude f is an alternate representation of the reaction cross section (Eq. 2.1), eliminating the phase space factor.

$$\frac{d\sigma}{d\Omega} = \frac{p_\eta^*}{p_p^*}|f|^2 \tag{2.1}$$

p_p^* and p_η^* are the momenta of the initial and final state proton and η-meson in the center-of-mass-system (c.m.s.) respectively.

In the calculation of the two-step model the constituent $NN \rightarrow d\pi$ and $\pi N \rightarrow \eta N$ are not treated indepently as in earlier semi-classical model calculations [5], omitting the almost vanishing denominator of Eq. 2.2 in the threshold situation. In [8] the nuclear matrix element M of the double scattering process depicted in Fig. 2.4 is evaluated:

$$M = \int \frac{m_d}{E_d} d^3k \int \frac{m_n}{E_n} d^3q \frac{1}{(2\pi)^3 2E_\pi} \frac{i}{E_0 - E_{int} + i\varepsilon} M_K . \tag{2.2}$$

Where $E_0 = E_\eta + E_{He}$ is the total energy of the initial (and final) state, E_n and E_d are the energies of the neutron and deuteron in their intermediate state, where the total energy is E_{int} [8]. m_d, m_n, are their masses, respectively and E_π is the energy of the intermediate pion. q and k are the Fermi momenta of the constituent particles. M_K is the product of the individual matrix elements of the constituent reactions;

$$M_K = \sum_{int} M(pd \rightarrow {}^3He_f) M(\pi^+ n \rightarrow p\eta_f) M(d_i \rightarrow p_c n) M(p_i p_c \rightarrow \pi^+ d) , \tag{2.3}$$

where the sum runs over the spin degrees of freedom of the intermediate particles [8].

In addition to the process described by Eq. 2.3, there is a similar contribution from a neutral intermediate pion (Fig. 2.4 and Tab. 2.2, orange), i.e.

$$\tilde{M}_K = \sum_{int} M(pd \rightarrow {}^3He_f) M(\pi^0 p \rightarrow p\eta_f) M(d_i \rightarrow n_c p) M(p_i n_c \rightarrow \pi^0 d) \quad [8]. \tag{2.4}$$

This matrix element is half of the first, so that the resulting cross section should be multiplied by an isospin factor

$$N_T = 9/4 \ [8]. \tag{2.5}$$

One can calculate the differential center-of-mass cross section from the nuclear matrix element M, calculated in Eq. 2.2 through Eq. 2.5:

$$\frac{d\sigma}{d\Omega} = \frac{m_{He} m_p}{4(2\pi)^2 s} \cdot \frac{p_\eta}{p_d} \cdot N_T \cdot \frac{1}{6} \sum_{spins} |M|^2 , \tag{2.6}$$

with $\sqrt{s}$ being the total center-of-mass energy of the $\eta - {}^3$He-system [8].

The production amplitude can then be derived by combining Eq. 2.1 and Eq. 2.6.

As the two-step process alone is not able to described neither the cross section value, nor the shape of the excitation function, the observed rapid drop of the production amplitude with increasing energy, a strong η–^{3}He final state interaction (FSI) with a large η–^{3}He scattering length [10] had to be included into the two-step approach. This modifies the waves emerging from a nucleon, replacing them with effective waves [11]. As the η-nucleon potential is completely unknown, a short range potential, compared to the size of the ^{3}He, is assumed. The ^{3}He potential is simply the non-overlapping group of three scattering centers placed on a equilateral triangle, expressed in terms of individual on-shell amplitudes [12], [13]. As only s-waves play a vital role in the production process [1], only s-wave scattering has to be taken into account inside the wave function. Carrying out these calculations [8], [6] leads to an enhancement factor f (Eq. 2.7) to the slowly varying production amplitude f_B, extracted from the two-step process alone.

$$f = \frac{f_B}{p^* \cdot a \cdot \cot\delta - i \cdot p^* \cdot a} \text{ [10]} \tag{2.7}$$

The enhancement factor of Eq. 2.7 includes the center-of-mass momentum p* of the outgoing particle, the phase shift δ of the underlying s-wave production process and the scattering length a of the η–^{3}He system. Close to theshold, the phase shift δ can be approximated by the scattering length a and the effective range r_0:

$$p^* \cot\delta = \frac{1}{a} + \frac{1}{2} r_0 p^{*2} \tag{2.8}$$

Terms of higher order in p (e.g. p^{*4}) can be neglected due to the low excess energies in the pd $\rightarrow$ ^{3}He η reaction. Furthermore, as energies are low, even effective range effects can be neglected [6], reducing the denominator of Eq. 2.7 by using Eq. 2.8 to:

$$f \approx \frac{f_B}{1 - i \cdot p^* \cdot a} \text{ [10]} \tag{2.9}$$

The complex scattering length a itself is the limes of the scattering amplitude at threshold:

$$a = \lim_{q \rightarrow 0} f_{scat.} . \tag{2.10}$$

When taking into account this final state corrections, the calculated $|f|^2$ grows to 690 nb/sr (Fig. 2.6, blue triangle), which requires then only a scaling factor of 2.5 to fit the predictions of the calculation to experimental data [8].

2.1.5 Consequences of a strong FSI effect

The necessity for a strong η–^{3}He final state interaction to describe the energy variation near threshold [10] opened up another opportunity of interesting physics in the pd $\rightarrow$ ^{3}He η reaction channel, namely the possibility to form an η–^{3}He quasi-bound state.

Assuming the real part of the scattering length $\Re$(a) would become not only large but negative, as indicated by calculation within an optical potential, formation of such a state would become possible. However, the real part of a is not directly accessible in nucleon scattering experiments, such as the pd $\rightarrow$ ^{3}He η production measurements, but rather extracting a correlation between real and imaginary parts, where one of them becomes very large [10]. Therefore, a large scattering length, extracted from such information, is only an indication for a strong effect, but can not decide between an attractive bound or quasi-bound state (negative sign of $\Re$(a)) or a repulsive state (positive sign of $\Re$(a)) between the η and ^{3}He in the exit channel.

2.1.6 Beyond threshold measurements at GEM

An additional measurement by GEM, situated at the COSY facility in Jülich, added a single data point extending the database beyond the close to threshold region upto an excess energy of Q_η = 49.3 MeV.

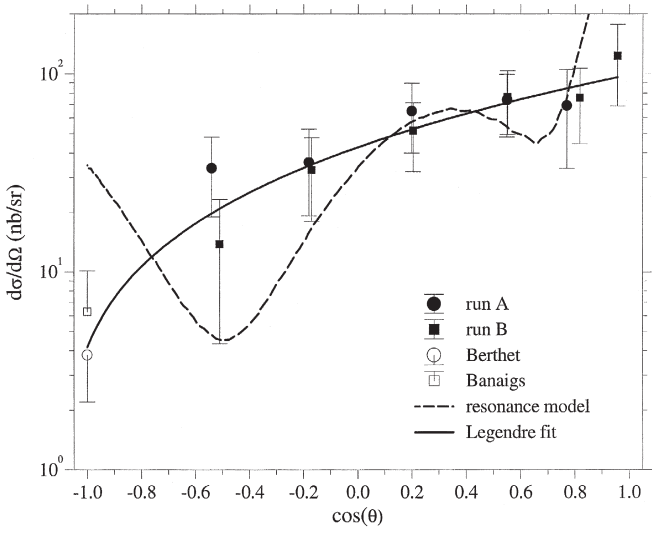

Figure 2.7 Fig. 4 taken from [14]: Angular distribution for the emitted η in the pd $\rightarrow$ ^{3}He η reaction at Q_η=49.3 MeV. At this high excess energy the emission is no longer isotropic, revealing an angular distribition that is not flat. Closed symbols are from the GEM experiment, open symbols are taken from [15] (square) at a 70 MeV higher and [3] (circle) at a 5 MeV lower beam energy. A legendre fit (solid line) was applied to the data to calculate the total cross section from the angular distribution. A calculation within the resonance model, put forward by [14] is included as a dashed line.

Besides a cross section higher than expected from the shape of the excitation function close to threshold, these measurements also revealed a deviation from pure s-wave production in the angular dependend analysis, by exposing a highly anisotropic, forward peaked emission of the produced η mesons (Fig. 2.7).

To reproduce the excitation function including the measured data point, a different model approach was choosen, promoting a purely resonant production of the η meson in a Breit-Wigner fit.

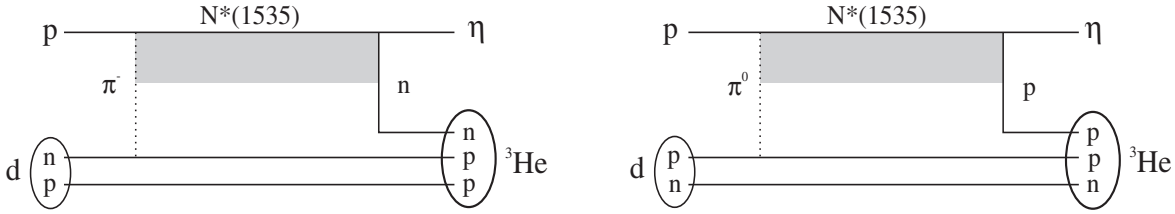

Figure 2.8 Resonant production mechanism for the pd → ^{3}He η reaction. By exchange of a virtual pion, much like in the two-step mechanism, the S_{11}-resonance N*(1535) is excited. In the decay process of the resonance the η is produced and the residual nucleons form the ^{3}He.

This process involves the exchange of a virtual pion between the beam proton and the target deuteron, much like in the two-step process. But it is used to excite the N*(1535) resonance, rather than forming a intermediate nucleon state.

property	**value**
official name	N(1535)
I	1/2
$\mathbf{J^P}$	$1/2^-$
mass	1535 MeV
width	150 MeV

Table 2.3 Properties of the $N^*(1535)$ S_{11} resonance [16]

In the decay of the resonance the η meson is produced and the residual nucleons build the ^{3}He.

decay mode	fraction
N η	45 – 60 %
N π	35 – 55 %
N ππ	1 – 10 %
N(1440) π	<7 %
N ρ	<4 %

Table 2.4 Decay modes of the $N^*(1535)$ S_{11} resonance [16]

More important than the differences between two-step and resonant process is the fact, that this model neglects the presence of an FSI-effect completely. Therefore, such a model is expected to be useful at excess energies comparably high above the production threshold, where the ^{3}He and η ejectiles are emitted with large relative momenta and therefore an FSI-effect is unlikely. A more detailed and hands-on description of a fit inside the resonance model can be found in Section 5.3.1 on page 85.

By incorporating arbitrary data sets of very far from threshold measurements and carefully adjusting their statistical errors, the Breit-Wigner fit of the resonance model describes very roughly most of the data, as presented in Fig. 2.9.

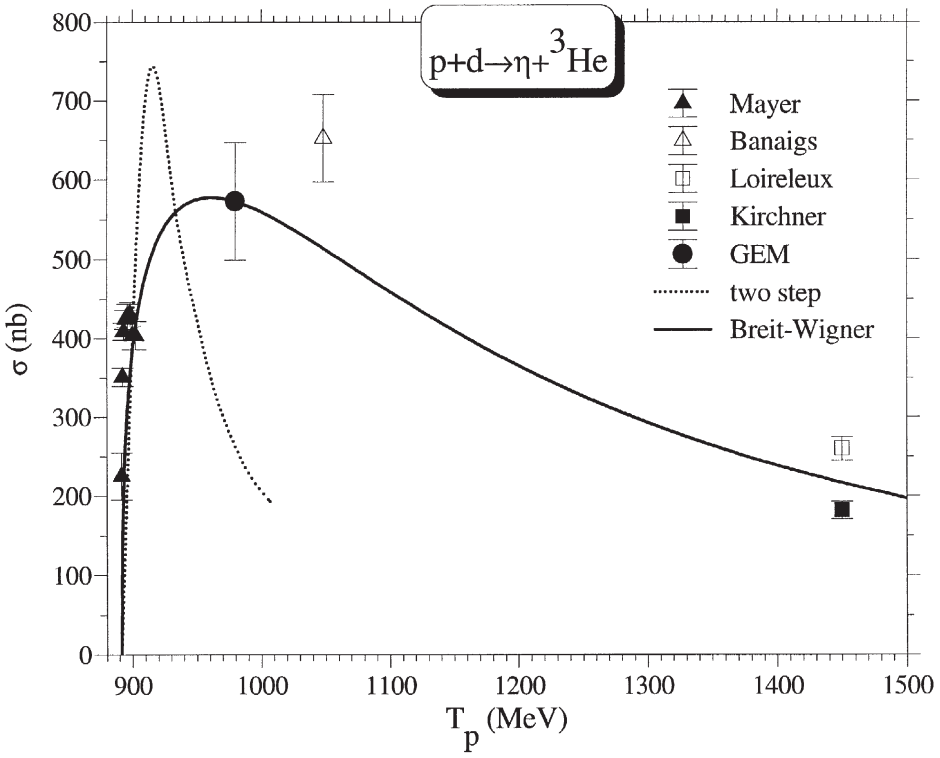

Figure 2.9 Fig. 5 taken from [14]: Total cross section for the pd → ^{3}He η reaction as function of the proton beam energy. Data are differentiated by symbols: Mayer [2], Banaigs [15], Loireleux [17], Kirchner [18]. A normalized [14] calculation for the close to threshold behavior has been plotted beyond the high energy GEM data point as a dotted line, failing to describe any data point beyond the highest Mayer et al. data it was scaled to fit. A calculation inside the resonance model is shown as a solid line, the scale is however arbitrarily scaled to fit the GEM data. Due to the extended scale of the plot up to the Kirchner and Loireleux measurement, this presentation does not do justice to the accuracy of this fit in describing the close to threshold data. For a better presentation of the near threshold region see Fig. 2.10.

However, the magnitude of the Breit-Wigner fit was scaled arbitrarily to fit the GEM data point, and when selecting a different presentation of the data, either using a logarithmic scale of the abscissa or limiting the range of the presented data up to the GEM data point (Fig. 2.10), the improved visibility of the near-threshold region reveals the overall deficiency of the fit to describe almost any other than the GEM data point it was fixed to.

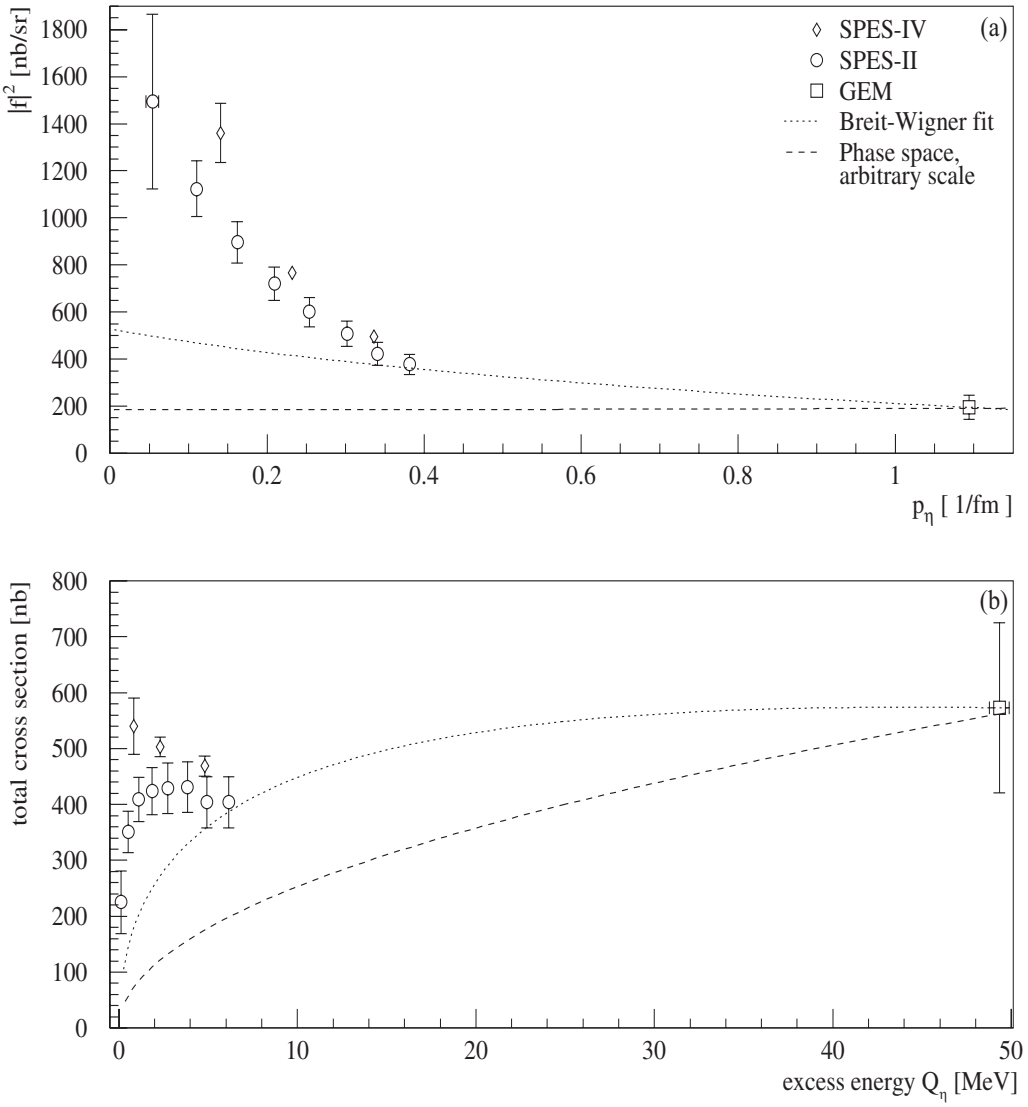

Figure 2.10 Excitation function of the pd $\rightarrow$ ^{3}He η reaction, including the near threshold data measured at SPES-II and SPES-IV, as well as a GEM data point higher above threshold. (a) Production amplitude $|f|^2$. (b) Total cross section. When viewed with enhanced visibility of the near-threshold region, the predictions based on a Breit-Wigner fit to the resonance model (dotted line), no longer describe the data well, as might be anticipated from Fig. 5 in [14] presented in Fig. 2.9. Besides the data point it was scaled to fit, it only touches the two highest data points from SPES-II within the errorbars, underestimating any lower data point significantly. Expectations based upon phase space also at an arbitrary scale fit to the GEM data point have been included in the plots as dashed lines (different scaling factor than in Fig. 2.3 and Fig. 2.6).

Despite the way to describe the excitation function by a model approach only valid for the high-energy data, the results of the measurement rise two important questions: How does the excess energy dependence of the excitation function evolve from the well investigated very close to threshold region to the single high-energy point from GEM? Furthermore how does the under-

lying production process change over the intermediate energy range between the low and high energy measurements, especially in view of the participating partial waves?

2.1.7 Motivation for the measurements at COSY-11

To shed light on these questions COSY-11 started a measurement program at the Forschungszentrum Jülich to investigate the intermediate energy region between the Saturne and GEM measurements. The aim of this effort was to close the gap between the available data points (Fig. 2.11, blue area), by measuring the excitation function at five excess energies of Q_η = 5 MeV, 10.8 MeV, 15.2 MeV, 19.9 MeV and 40.6 MeV, assuming a mass of the η meson of m_η= 547.3 MeV/c^2. In this region, the shape of the excitation function allows to directly decide between the two proposed reaction mechanisms (Fig. 2.11, dashed and dotted lines). A drop of the excitation function supporting the FSI Ansatz of the two-step model calculation (Fig. 2.11, dotted line) and a rise in the excitation function giving additional data to support the resonant production mechanism (Fig. 2.11, dashed line).

The choosen excess energies additionally provide an ideal overlap with the earlier very close to threshold measurements on the one side (Fig. 2.11, open circles) and additional measurements carried out at the Svedberg Laboratory in Uppsala on the other side (Fig. 2.11, open triangles). These measurments were carried out by WASA/PROMICE, covering higher excess energies of Q_η = 21.7 MeV, 41.1 MeV, 80.6 MeV and 114.8 MeV [19], of which the two highest are not coverable by the threshold measurement optimized COSY-11 installation and have been excluded from Fig. 2.11.

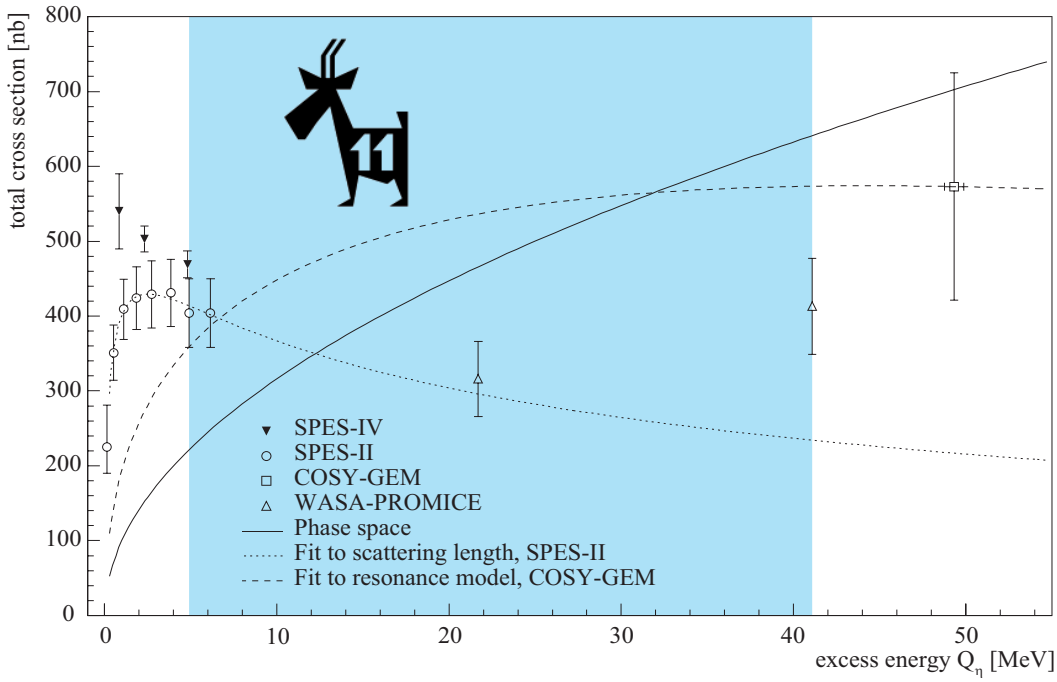

Figure 2.11 Cross sections available from various experimental facilities prior to the COSY-11 measurements on the pd → ^{3}He η reaction. The expectation for the energy dependence of the total cross section, based on an arbitrarily scaled pure phase space behavior is indicated by the solid line. The dashed and dotted lines represent calculations based on the different models. The COSY-11 studies presented in this work cover the range of excess energies indicated by the blue area.

The results of the COSY-11 investigations on the energy dependence of the excitation function and additionally examining the angular distribution of the recorded reaction ejectiles are the subject of the work presented here. This includes the review of all data sets available at the time of the analysis and result publication here [20]. Furthermore, the scattering length of the η–^{3}He system has been extracted from the COSY-11 extended database and the correlation between the real and imaginary part of the scattering length is discussed.

2.2 The η-meson

The η was first predicted (named $\pi^{0\prime}$) in the 1950's as one of the building blocks in the Sakata model [23]. Together with its sister particle, the η′ (then named $\pi^{0\prime\prime}$), it was ment to augment the hitherto only known pseudoscalar mesons pions and kaons, as neutral, isospin=0 mesons, to make the Sakata model consistent. As there was no experimental evidence for such a particle at that time, this was credited as inferiority of the model desciption.

2.2.1 Mesons

Mesons are hadrons, made up of quark/anti-quark pairs ($q\bar{q}$), which differentiates them from baryons, which are hadrons consisting of three quarks (e.g. uud for the proton). The quark content of a special family of mesons, the pseudo-scalar mesons is presented in Tab. 2.5 and Fig. 2.2. Both types of hadrons are subject to the strong interaction, which sets them apart from leptons, such as the electron, which are affected by the weak interaction and do not have quark content.

One can devide mesons by their spin into pseudo-scalar and vector mesons. Pseudo-scalar mesons having rectified spin J=0 and vector mesons having reversed spin J=1 of the quark/ anti-quark pair.

	u	**d**	**s**
$\bar{\mathbf{u}}$	π^0, η, η'	π^-	K^-
$\bar{\mathbf{d}}$	π^+	π^0, η, η'	$\overline{K}^0$
$\bar{\mathbf{s}}$	K^+	K^0	η, η'

Table 2.5 Quark content of the pseudo-scalar mesons, considering only u, d, s-quarks

The term pseudo-scalar is attributed to the negative eigenparity of the mesons with vanishing spin J=0. Besides the η also the η', the kaons ($K^+, K^-, K^0, \overline{K}^0$) and the pions ($\pi^+, \pi^-, \pi^0$) belong to the pseudo-scalar mesons. Being arranged in an SU(3)[1] octet and singlet, this arrangement is commonly refered to as the nonett of pseudo-scalar mesons (Fig. 2.2).

1. three dimensional special unitarian group

	J^P	I	I_3	S	C	mass [MeV/c^2]	lifetime/width
π^0	0^-	1	0	0	+1	134.9766 ± 0.0006	$(8.4 \pm 0.6)\cdot 10^{-17}$ s
π^+	0^-	1	+1	0		139.57018 ± 0.00035	$(2.6033 \pm 0.0005)\cdot 10^{-8}$ s
π^-	0^-	1	−1	0		139.57018 ± 0.00035	$(2.6033 \pm 0.0005)\cdot 10^{-8}$ s
K^+	0^-	1/2	+1/2	+1		493.677 ± 0.013	$(1.2386 \pm 0.0024)\cdot 10^{-8}$ s
K^-	0^-	1/2	−1/2	−1		493.677 ± 0.013	$(1.2386 \pm 0.0024)\cdot 10^{-8}$ s
$\overline{K}^0$	0^-	1/2	−1/2	+1		497.672 ± 0.031	K_L: $(5.17 \pm 0.04)\cdot 10^{-8}$ s
K^0	0^-	1/2	+1/2	−1		497.672 ± 0.031	K_S: $(0.8934 \pm 0.0008)\cdot 10^{-10}$ s
η	0^-	0	0	0	+1	547.3 ± 0.12	1.18 ± 0.11 keV/c^2
η′	0^-	0	0	0	+1	957.78 ± 0.14	0.0203 ± 0.016 MeV/c^2

Table 2.6 Properties and quantum numbers of pseudo-scalar mesons. (J: Spin, P: Parity, I: Isospin, I_3: 3.-component of Isospin, S: Strangeness, C: C-Parity) [24]

2.2.2 The χ^0 meson

In 1961 Gell-Mann developed his theory of strong interaction symmetry – the eight-fold way [25]. A pseudoscalar meson χ^0 (or η) is part of this framework. It decays into 2γ like the π^0, but is heavy enough for hadronic decay into $\pi^+\pi^-\gamma$, 3π or even 4π. The 3π decay however is forbidden by conservation of isospin and charge parity and the 4π decay is hampered by centrifugal barriers. The discovery of the η later the same year [26] passed unnoted, as it decayed into three pions, but was properly identified as the predicted pseudoscalar meson, the η, early in 1962 [27].

2.2.3 Quantummechanical and real ηs

The particles η and η′, observed in experiment, are described as a mixture of the SU(3) singulett η_1 and the SU(3) octett η_8 (eq. 2.12). These quantum mechanical particles are made up of the overlapping wavefunctions of the simple quark/anti-quark combination ($u\bar{u}$), ($d\bar{d}$) and ($s\bar{s}$) (eq. 2.11).

$$\eta_1 = \frac{(u\bar{u} + d\bar{d} + s\bar{s})}{\sqrt{3}} \qquad \eta_8 = \frac{(u\bar{u} + d\bar{d} - 2s\bar{s})}{\sqrt{6}} \tag{2.11}$$

$$\eta = \eta_8 \cos\Theta - \eta_1 \sin\Theta \qquad \eta' = \eta_8 \sin\Theta + \eta_1 \cos\Theta \tag{2.12}$$

The mixing angle Θ of the SU(3) particles in the physical particles has been determined to be in the order of 20° [28].

2.2.4 Decay

The η decays in basically to ways, hadronic decay into pions and radiative decay into γ, both of which are not or almost not detectable by the COSY-11 detection system.

decay channel	fraction
2γ	(39.21 ± 0.34) %
$3\pi^0$	(32.2 ± 0.4) %
$\pi^+\pi^-\pi^0$	(23.1 ± 0.5) %
$\pi^+\pi^-\gamma$	(4.77 ± 0.13) %

Table 2.7 Common decay channels of the η by importance [24]

The γ and π^0 decay products are not detectable, due to the design of COSY-11, to only identify charged particles. The charged decay pions are only detectable with very limited efficiency due to the geometrical acceptance. This is however no limitation to the experiment, as the identification of ^{3}He and the determination of its four-momentum vector, is sufficient to deduce the η in the pd $\rightarrow$ ^{3}He η reaction by means of the missing mass technique.

2.3 η-mesic nuclei, bound or quasi-bound states?

Within the field of particle interaction, the formation of bound or quasi-bound states between an η meson and a nucleon or nucleus, forming so called η-mesic nuclei has attracted a lot of both theoretical and experimental interest. Predicted by Haider and Liu [30], the interaction of the η with a nucleus is expected to be attractive, as in the elementary η–N interaction [40][41][42], and therefore allows for the formation of a bound state. Recently, it was argued that the η bound state will deliver information about the singlet component of the η meson [43]. Although the strength of the attractive potential is supposed to increase with the mass of the nucleus, the answer to the question as to which is the lightest η-mesic nucleus is still unknown. Various predictions of the lowest possible atomic number A of the atom, that is able to form an η-mesic nucleus are presented in Tab. 2.8.

Year	Authors	A	model calculation	Reference
1985	Haider and Liu	≥ 12	optical potential, 3d relativistic wave equation	[30]
1986	Liu and Haider	> 10	optical potential, see above	[31]
1987	Li, Cheng and Kuo	≥ 12	Binding energy, Green's function	[32]
1990	Chian, Oset and Liu	≥ 12	optical potential, N^* decay	[33]
1995	Wycech, Green, Niskanen	≥ 4	optical potential, multiple scattering theory	[34]
1995	Rakityansky et al.	< 12	finite-rank approximation	[35]
1996	Rakityansky et al.	≥ 2	finite-rank approximation	[36]
1998	Tsushima et al.	≥ 6	quark-meson coupling	[37]
1999	Hayano, Hirenzaki, Gillitzer	≥ 7	optical potential	[38]
2002	Haider and Liu	≥ 4	optical potential	[39]

Table 2.8 Predicitions of the lightest η-mesic nuclei. Predictions for η-nucleus bound states found in various model calculations are presented in chronological.

These predictions are based on different model calculations having certain constraints, input assumptions and approximations. Basically five different theoretical model categories have been used to describe the η-nucleus bound system: An optical potential, a Green's function method, multiple scattering, finite-rank approximation and quark-meson coupling.

2.3.1 First prediction and calculation

The initial approach by Haider and Liu to calculate the bound η-system [30] was based on a relativistic three-dimensional wave equation

$$\frac{k'^2}{2\mu}\hat{\psi}(k') + \int dk \langle k'|\hat{V}|k\rangle \hat{\psi}(k) = E\hat{\psi}(k'), \qquad (2.13)$$

where $E=k^2/2\mu$ is the complex eigenenergy of the system and $\mu=m_\eta m_A/(m_\eta+m_A)$ is the reduced mass. With $\Re(k^2) \equiv k_r^2 < 0$ or $\Re(E) < 0$ the condition for a bound state is met. V can be described by an optical potential V.

As a result, Haider and Liu calculated the minimum mass number to allow for the formation of a bound state to be A=12 in 1985, but published revised calculations later in 1986 (A > 10) [31] and 2002, bringing down their limit to A=4 [39].

2.3.2 Microscopic binding energy calculation

Another study by Li, Cheng and Kuo [32] investigates the posibilty of a bound η-system by carrying out a microscopic calculation of the binding energy ε_n of the η-mesic nucleus $^{16}O_\eta$ using a standard Green's function method [44]. By definition

$$\varepsilon_n \equiv E_n(^{16}O_\eta) - E_0(^{16}O) \ , \tag{2.14}$$

where $E_n(^{16}O_\eta)$ and $E_0(^{16}O)$ are the energies of the η-^{16}O system and the ground state energy of the ^{16}O nucleus, respectively. If the energy calculated for ε_n is less than the mass of the η-meson, then the η-meson is bound to ^{16}O; the binding energy E_B of the η-^{16}O bound state being: $E_B=\varepsilon_n-m_\eta<0$. Although the approach is entirely different, it leads to the same conclusion as the initial Haider/Liu calculations [30], that an η-nucleus bound state is possible for minimum mass number of A=12 and depends crucially on the attractive η–N–N^*(1535) interactions in the S_{11} channel [32].

2.3.3 Resonance decays change width of state from narrow to broad

A study by Chiang, Oset and Liu [33] extends the optical potential approach, by taking into account the free decay modes of the N^* and its many-body decay modes up to one-particle-hole excitation. It especially pays attention to the widths of the calculated bound states, finding most of them too large to separate between levels. Thus making it rather unlikely to detect any narrow peaks experimentally, as results from [45] together with earlier calculations [31] suggest. Although this does not change the expectations of the minimum mass number (A = 12), compared to the earlier calculations[30][31][32], it gives an idea why experimental searches [45] failed to find evidence for such a state.

2.3.4 Few-body interactions limit FSI contribution to bound state

Wycech, Green and Niskanen [34] take a different approach to calculate the possibilty of an η-nucleus bound state inside an optical model. Concentrating on the few-body interaction of η mesons, they especially pay attention to the final state interaction and the influence of the interference of free and scattered waves in the final η-helium states of the pd $\rightarrow \eta$ ^{3}He and dd $\rightarrow \eta$ ^{4}He reactions. Hereby they find this interference to be the dominant factor and only minor contributions of the „not very large scattering length" to the strength of bound state, in contrast to [10]. They first calculate the basic η–nucleon scattering length and convert it into the effective η–^{3,4}He scattering lengths which in turn is used to calculate the final state interactions in the pd $\rightarrow \eta$ ^{3}He and dd $\rightarrow \eta$ ^{4}He reactions. The calculation of the effective scattering lengths is

achieved by applying a multiple scattering expansion and using free η–N scattering as a starting point, as an alternate equivalent to the nummerical solvation of the optical model. Furthermore, the refinement of the optical model description by removing multiple collisions on the same nucleon and introducing an off-shell η-nucleon scattering matrix, introduce massive changes to the η-helium scattering lengths. It yields a sizable possitive real part of the scattering length in the η–^{3}He system rather than the large negative part deduced from the simplest optical model. For the η–^{4}He system, that is not the case.

As a result of their calculations they determine the minimum mass number A = 4 to be much smaller than in the calulations from [30],[31],[32],[33].

2.3.5 Finite Rank Approximation accounts external and internal motion separately

Rakityanski et al. [35], [36] chose to replace the optical potential or multiple scattering theory in earlier calculations by a Finite Rank Approximation of the Hamiltonian [46], inside few-body equations with separable η–N amplitudes, to calculate the η–N scattering lengths for ^{2}H, ^{3}H, ^{3}He and ^{4}He. Basically separating the motion of the projectile H_0 and the internal motion inside the nucleus H_A, the Hamiltonian is splitted into:

$$H = H_0 + V + H_A. \tag{2.15}$$

With V being the the sum of the individual η–N-interactions [36]:

$$V = \sum_{i=1}^{A} V_i. \tag{2.16}$$

In a refined calculation of the nuclear wave function inside H_A [46] the simple Gaussian form approximation of [36] is replaced by a more realistic nuclear wave function. This nuclear wave function is obtained via the so-called integro-differential equation approach (IDEA) [46]. The possiblity for the formation of a bound state is found for all the before mentioned nuclei, further decreasing the minimum mass number calculated in [34] to A = 2.

2.3.6 Quark-meson coupling

Tsushima et al. [37] calculated the potentials of the η and other mesons in ^{6}He and heavier nuclei in local density approximation, embedding the mesons in the nucleus described by solving the mean-field equations of motion in the the quark-meson coupling (QMC) model [47]. They propose A = 6 to be the minimum mass number to allow for a bound state.

2.3.7 Combination of the optical potential approach and Green's function method

Hayano et al. [38] leveraged an optical potential based on the available η–N scattering length estimates in conjunction with a Green function method to calculate the formation cross sections of bound states of η and ω in light nucleii. With a first-order potential they calculated the binding energies and widths by solving the Klein-Gordon equation, ommiting the vector part of the potential. They then calculate the reaction cross section from the nuclear response function S(E) as formulated in [50] by using a Green function. As a result, they expect to find experimental evidence for a η–^{7}Li bound state, corresponding to a minimum mass number of A = 7.

2.3.8 Different optical potentials evaluated

Haider and Liu improved their earlier calculations [30], [31] in [39], by comparing three different η–nucleus optical potentials. They find that a large scattering length is not necessarily an indication for a bound state, as the in-medium η–N interaction for a bound state is 30 MeV below the freespace η–N threshold. This substantially reduces the attractive force between the η and a nucleon and scattering length approaches overpredict the binding energy ε_η. Despite that, their newer calculations lead to η–mesic nuclei for as low as $A \geq 4$, while earlier calculations [30], [31] predicted A to be no lower than ten. They however advise to carry out experimental studies at rather heavier nuclei than those indicated by the on-shell scattering length. They furthermore stress, that a scattering length analysis, like it is carried out in this work as a by-product of the main experimental goal, can not provide an unequivocal determination of the existence of the η–nucleus bound state. Rather direct measurements are required to identify such bound states.

3 Experiment

The COSY-11 installation [51] is an internal experimental facility located in an arc section of the cooler synchrotron and storage ring COSY [52] at the Forschungszentrum Jülich, designed for near-threshold meson and hyperon production in proton-proton and proton-deuteron reactions.

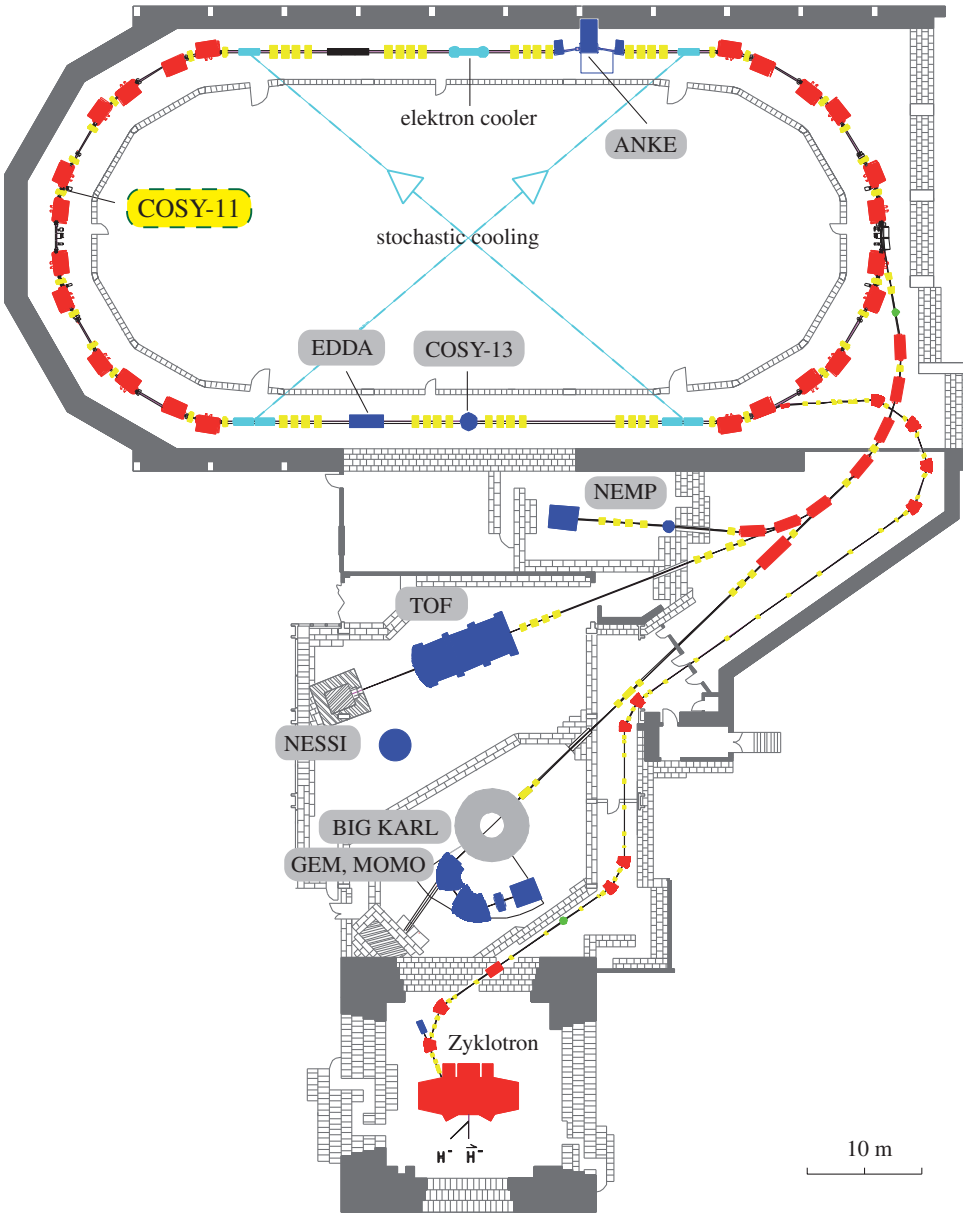

Figure 3.1 Sketch of the cooler synchrotron and storage ring COSY at the Forschungszentrum Jülich. The internal and external experimental facilities are marked by their name. Recent installations, such as WASA-at-COSY are not included.

3.1 Experimental Setup

A cluster target [53], operated with deuterium gas, was used to provide a dense deuteron target for the stochastically cooled, high-precision proton beam of COSY. The COSY-11 facility makes use of one of the accelerator dipoles as a spectrometer magnet to separate the positively charged reaction ejectiles (e.g. ^{3}He nuclei) from the circulating beam and guide them towards the forward detection system (Fig. 3.2).

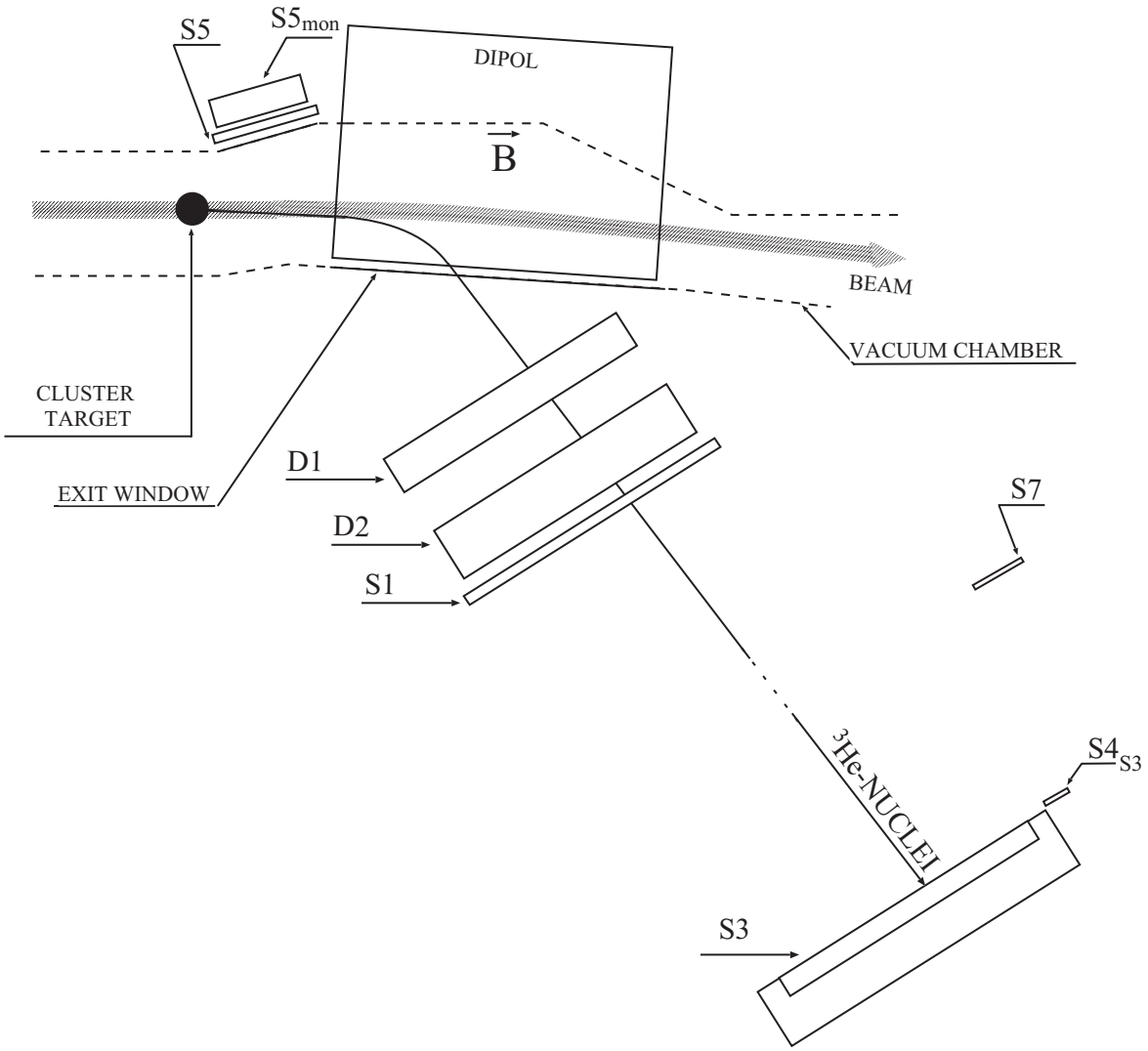

Figure 3.2 Sketch of the COSY-11 installation. The magnetic spectrometer, consisting of drift chambers and scintillation and silicon-pad detectors is located in an arc section of the cooler synchroton COSY at the Forschungszentrum Jülich.

This system consists of a set of two drift chambers (D1, D2), used for track reconstruction, and two large scintillator hodoscopes (S1, S3). Tracing back the tracks through the magnetic field of the spectrometer magnet [54], [55], [56] to the fixed interaction point leads to a momentum

reconstruction with a precision of better than 1% [42]. The scintillation detectors S1 (placed directly behind the second drift chamber) and S3 (placed a distance farther of roughly 9 m) are used as a start and stop combination for time-of-flight measurements. Particle identification can thus be performed by reconstructing the mass of the ejectiles using the momentum and velocity information,

$$m_{reconstructed} = \frac{p}{c \cdot \gamma \cdot \beta} \tag{3.1}$$

yielding a full four-momentum vector reconstruction for all detected positively charged particles. Additionally, the detected particle can be identified independently by the energy loss information ΔE provided by the S1-detector in combination with the reconstructed momentum (Fig. 3.3).

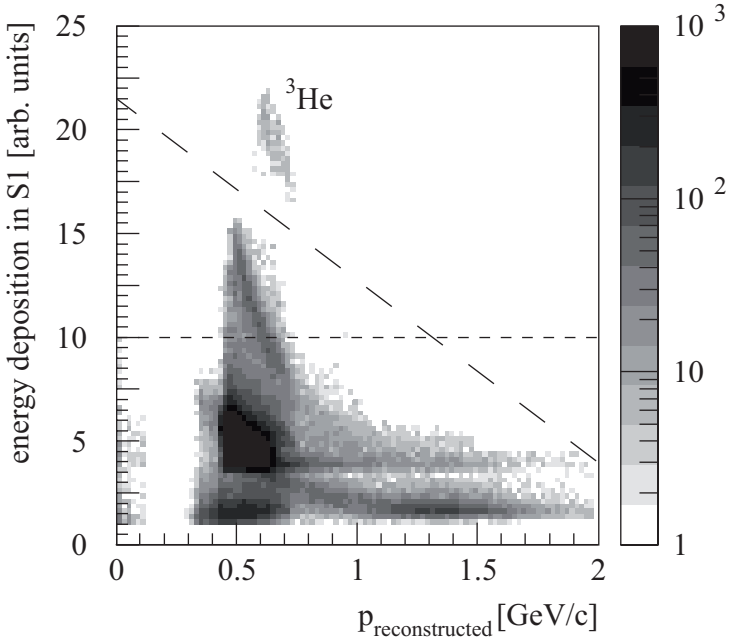

Figure 3.3 ^{3}He selection from events triggered by the detection system for a beam momentum of 1.593 GeV/c (Q_η = 10.8 MeV). Because of the high-energy deposition of the ^{3}He nuclei in the scintillator detector S1, ^{3}He events can be separated from the background consisting of pions, protons, deuterons, and tritons. The dashed lines indicate the cuts on energy loss and the correlation of energy loss to the reconstructed momentum used to select the^{3}He events. The momentum reconstruction in the magnetic field assumes q = 2. For details See "Event Selection" on page 45.

To obtain cross sections, the pd $\rightarrow$ ^{3}He X data are normalized using the results on the proton-deuteron elastic scattering that was measured in parallel. For this purpose additional silicon-pad and scintillation detectors (S5 and $S5_{mon}$) in the target area are used to detect the elastically scattered deuteron in coincidence with the detected proton in the forward-detection system (D1&2, S1) [57], [58]. The complementary case of a deuteron in the forward direction and a coincident

proton in the monitor detector is allowed by kinematics. However, it is almost unobserved in the experiment because of the large momentum transfers in this case, that make deuteron breakup highly probable.

3.1.1 Storage Ring COSY

COSY is a cooler synchroton, aimed at the storage of protons and deuterons, in a race track shaped ring of roughly 184 m in circumference. Put into operation in 1993 it is part of the latest generation of accelerators using phase space cooling. Besides storing unpolarised protons it is also able to store polarised protons, both at momenta between 270 and 3650 MeV/c [52].

Due to its high precision, COSY is able to deliver a momentum resolution of $\delta p/p = 0.5$ ‰ and an emittance $\varepsilon = 2\pi$ mm rad, even when none of the two available cooling techniques are in use. With cooling enabled, the momentum resolution is improved up to 0.1 ‰ and the emittance is reduced to ~ 1π mm rad. The absolute beam mometum can be determined with an uncertainty of ~ 1‰ [59].

The following two cooling techniques are available:

1. Electron cooling, which is available up to beam momenta of roughly 650 MeV/c.

2. Stochastic cooling, available from 1,500 MeV/c up to the maximum beam momentum available at COSY.

The JULIC cyclotron, operated in continous mode, serves as a pre-accelerator to COSY. H^- ions are stripped at 45 MeV/c on a 20 $\mu g/cm^2$ thin carbon foil, before entering the storage ring [60]. COSY accelerates the injected protons to the desired energy and stores them for use by experiments such as COSY-11, that are installed directly in the COSY ring, or allows them to be extracted from the ring and guided to the various external experimental facilities in the adjacent target areas.

3.1.2 Cluster target device

In conjunction with the highly precise proton beam provided in the COSY storage ring, there is need for a windowless target of comparably low density, compared to solid state targets. This “low” density is necessary to keep the precision of the unscattered proton beam over storage time and not heat it up from energy loss by scattering on the target too much. As it is of course necessary to have an interaction between beam and target for experiment, it must not exceed the level of influcene it has on the beam, that can be compensated by the cooling mechanism build into the storage ring.

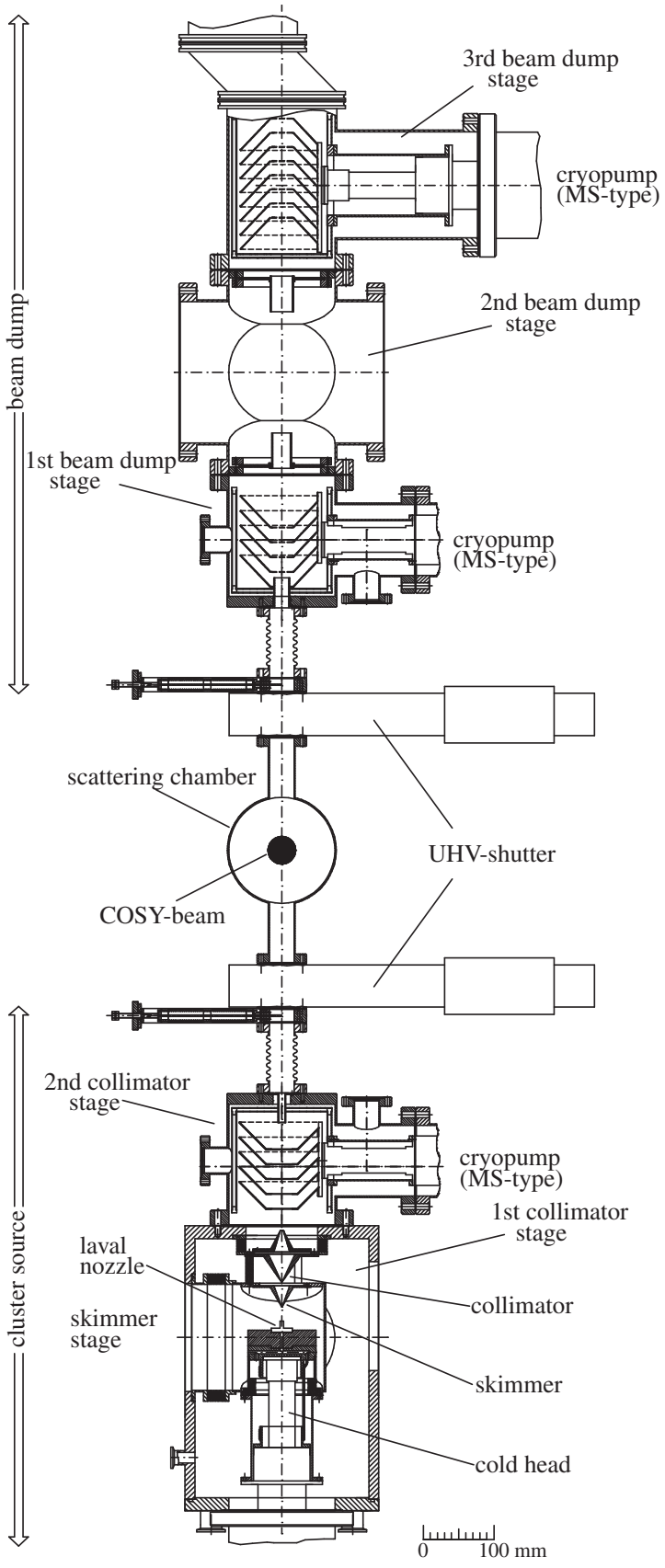

Figure 3.4 Construction of the Münster type cluster target at COSY-11

A cluster target is the ideal solution to these prerequisites, as it delivers a well defined interaction volume of homogenous density and very little background from secondary reactions [53]. It is in clear advantage of gas jet targets, as it has only negligible additional residual gas ballast in the scattering region and in contrast to solid state targets does not deteriorate due to radiation damage.

The Münster type cluster target at COSY-11 can be operated with both hydrogen and deuterium gas, that is cleaned by a palladium membrane purifier from any traceable impurities. Highly purified gas is necessary to guarantee a stable operation of the cluster target device and further exclude any secondary reaction due to impurities in the hydrogen or deuterium clusters.

The cluster device is separated in two pieces by the scattering chamber. The cluster source is installed below the COSY beamline, whereas the cluster beam dump is installed above the scattering chamber. As the name suggest, the cluster beam is produced in the cluster source, shaped to the desired shape and size and sent through the scattering chamber. In the beam dump the cluster beam is stopped after passing the scattering chamber by various vacuum pumps, preventing a build up of gasous residues from broken up clusters, that might contaminate the COSY vacuum.

3.1.2.1 Cluster source

The basis for a cluster beam is ultra-pure hydrogen or deuterium gas, provided by a palladium membrane purifier. At a pressure of twelve to eighteen bar it is precooled and guided through a convergent-divergent laval nozzle of 16 µm, that ist cooled down to 20 - 30 K.

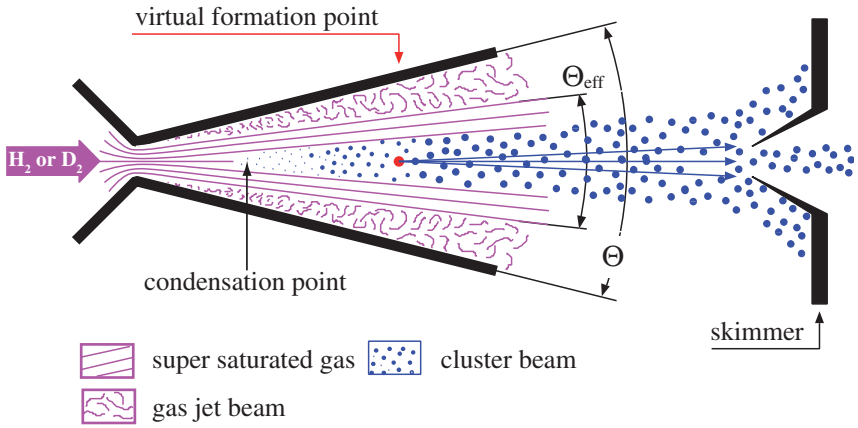

Figure 3.5 Clustering process inside a laval nozzle. Θ denotes the opening angle of the nozzle, whereas Θ_{eff} is the opening angle of the cluster beam and its surrounding gas jet. The latter is shaped off at the skimmer.

Due to the adibatic expansion of the gas through the laval nozzle, the gas temperature is further decreased and in conjunction with the high pressure a phase transition from the gasous to liquid state is performed beyond the boundaries of the vapour pressure curve.

In the region above the vapour pressure curve, the gas enters a supersaturated state before condensating into micro droplets, that form the so called clusters. More recent studies indicate, that in the region below the vapour pressure curve, a fluid of hydrogen passes the nozzle to form a spray of clusters [61]. A typical cluster consists of a thousand to hundered thousand atoms. Extensive studies on cluster formation [62], [63], [64], at the University of Münster allowed to develop the present Münster type cluster target that has been further improved for various target installations at COSY-ANKE and FAIR-PANDA [65], [66], [67].

Operating the cluster target in the supersatured mode, i.e. with supersaturated gas, allowed for a target density of ~ 10^{14} atoms/cm^2.

After the cluster beam was formed, it is shaped by a skimmer and collimator arrangement to the desired size. Additionally the skimmer and collimators separate the differential pumping systems that, in conjunction with specially designed cryopumps [68], prevents the contamination of the surrounding vacuum with residual gas, maintaing UHV conditions outside the cluster beam.

Leaving the cluster source, the monoenergetic cluster beam has a well defined direction and particle velocity and propagates through the scattering chamber according to intercept theorems, interacting with the circulation proton beam of COSY. At the point of interaction the cluster beam has a circular cross section with a diameter of 9 mm.

3.1.2.2 Cluster beam dump

After passing the scattering chamber the cluster beam enters the cluster beam dump, consisting of a three stage differential pumping system. Besides commercially available vacuum pumps, specially designed cryopumps are utilized to pump away the cluster material. This type of cryo pumps, also used in the cluster source, consist of conical shaped cooling plates that are mounted on top of cold heads along the cluster beam axis.

3.1.3 Scattering chamber

The scattering chamber for the COSY-11 installation fills the whole gap of the COSY-dipole used as the spectrometer magnet. Four exit windows allow reaction ejectiles to pass from the UHV environment inside the chamber into the detector system mounted inside the COSY tunnel. On the inside of the COSY ring, a column-free window, made of so called sandwich foil, that consists of two layers of crossed 150 μm carbon fiber and a 30 μm aluminum layer for vacuum tightness, causes only minimal multi-scattering effects on ejectiles inside the foil mate-

rial in the order of the detector resolution. All other exit windows are covered by stainless-steel foils. As detectors are mounted closely to these windows, angular inaccuraries due to scattering inside the foil material are negligible.

3.1.4 Detector system

3.1.4.1 Drift chambers D1 andD2

The two drift chambers D1 and D2 used for track reconstruction of positively charged particles, consist of two drift chamber packets [69], [70] with six and eight detection planes, respectively, at a distance of 70 cm. The detection area is 168 x 43.3 cm^2.

D1 consists of two planes of vertically oriented wires, two planes with wires inclined by -31 ° and two planes with wires inclined by +31°. D2 has additional two planes with vertical wires, as depicted in Fig. 3.6.

The distance between each pair of layers is 18 mm, layers of equal orientation are shifted by half a drift cell, to avoid left right ambiguity. This allows for a horizontal and vertical coordinate determination, even if multiple hits are recognized and thus leads to a drift chamber efficiency of almost 100 %.

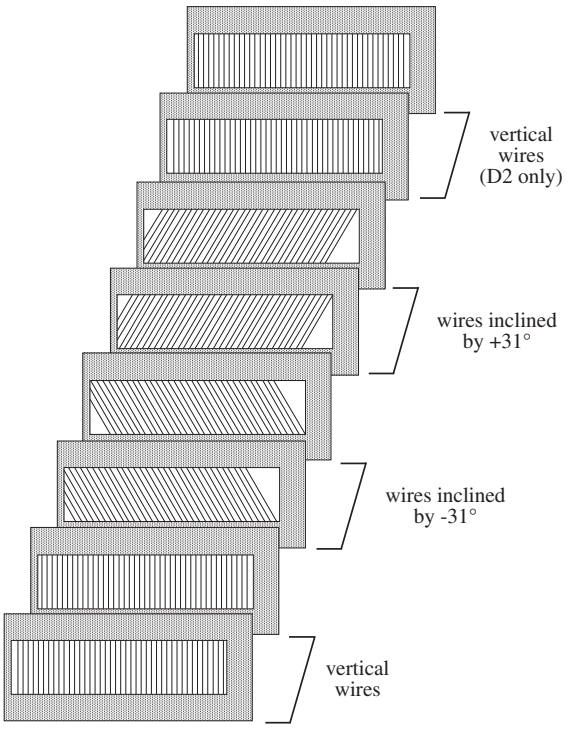

Figure 3.6 Schematic view of the wire layers making up drift chambers D1 and D2.

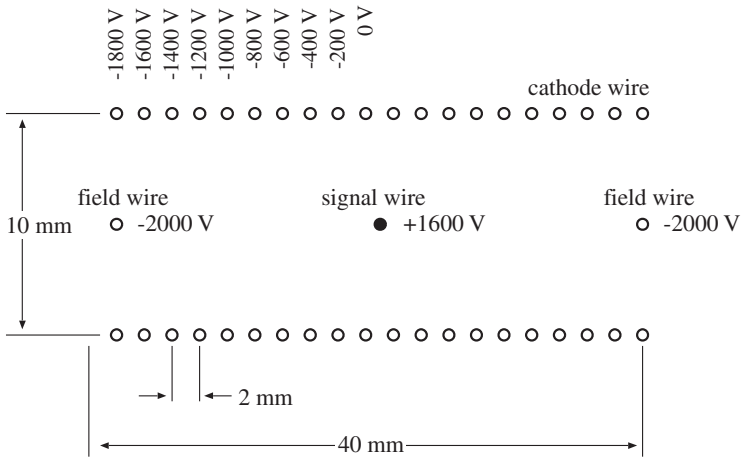

Figure 3.7 Design of a Graded-Field drift cell (schematic)

The drift cells are of Graded-Field type (Fig. 3.7) with a width of 40 mm, yielding a maximum drift time (half cell width) of 400 ns. It consists of two rows of cathode wires, with 20 wires per row, and two field wires in between the voltage -2000 V and one signal wire with the voltage +1600 V (Fig. 3.7). Charged particles traversing between the cathode wires invoke an ionization of the gas mixture of argon (50%) and ethane (50%) at athmospheric pressure [71]. The positively charged ions drift to the field wires and cathode wires with negative potential, while free electrons drift to the signal wire with the positive potential. The measurement of the smallest drift time of free electrons allows the determination of the distance between the sense wire and the particle track. Each of the drift planes gives the coordinates of the particle crossing point. To resolve the left-right ambiguity the neighboring planes of each pair are shifted by half of the cell size. The reconstruction procedure fits a straight line to those points, which is assumed to be the particle trajectory. For this the relation between the drift time and the drift path is needed, which, in turn, requires the time and space calibration of the D1 and D2 system. The detailed description of the necessary procedures can be found in [29].

When the particle trajectory is reconstructed, it is traced back to the target point through the known magnetic field in the dipole. Thereby, it gives the information about the momentum of the reconstructed particle. For a sufficient accuracy of the momentum determination, a good position resolution is needed. In the optimal case, i.e. when 1 GeV/c proton trajectories are perpendicular to the drift chamber planes, the position resolution amounts to about 100 μm [72] in the horizontal direction. In the data analysis, however, not only monoenergetic protons but also pions with different momenta are used for the calibration procedure. Their momenta are in majority below 1 GeV/c. Since small angle scattering effects are rising when the momentum of a charged particle traversing a medium is decreasing the typical value of the resolution in the horizontal direction for the COSY-11 drift chambers is about 250 μm [29]. The influence of the

temperature and humidity oscillations of the air surrounding the drift chambers on the drift time is described in [74]. In order to avoid the drift velocity fluctuation, the space-time calibration was done for each data file separately.

3.1.4.2 Scintillator hodoscope S1

When a charged particle interacts with matter its electrons are raised to excited levels directly or by secondary interactions of primary electrons. In scintillation materials the de-excitation energy is released in a small part as light. This light can be converted into an electric charge by a photomultiplier. The signal of the photomultiplier is proportional to the energy deposition in the scintillator and gives the time signal of the scintillator which is important for the particle velocity determination. Since in the COSY-11 setup scintillator detectors are mainly used for fast timing measurements, a good time resolution of the scintillation material is needed. For all scintillators at COSY-11 Bicron BC 404 plastic scintillator material is used [72], which is dedicated for fast counting purpose [73] .

The scintillator hodoscope S1 consists of sixteen 450 x 100 mm^2 scintillating laths, vertically arranged with about 1 mm overlap to adjacent modules and read out by photo-multipliers on the top and bottom of each lath. The sum signal for the energy deposited in the scintiallating material is independend of the hit position of the passing particle [75], [76]. Besides measurement of energy deposition of passing particles, S1 is also utilized as a start detector for a time-of-flight measurement in conjunction with the S3 detector described below. The time resolution of S1 is 160 - 220 ps.

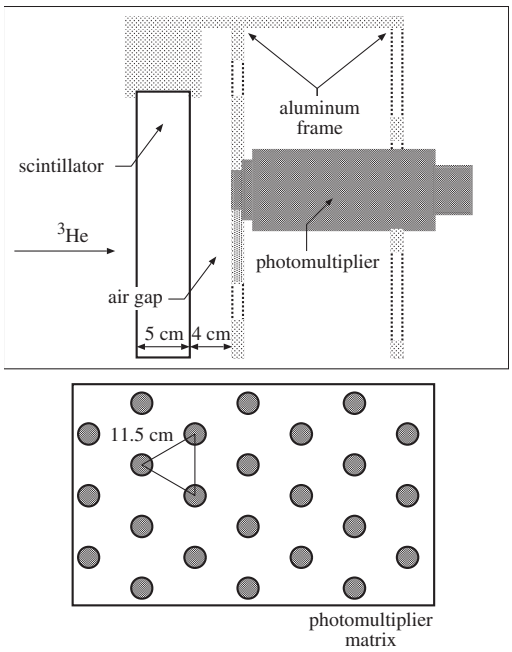

Figure 3.8 Design of the scintillation detector S3 and the photomultiplier assembly for matrix readout.

3.1.4.3 Scitillation wall S3

Scitillation detector S3 is modeled after the AMADEUS detector, designed by the University of Bonn [77]. It consists of a monolithic scintillator, 100 x 220 x 5 cm^3 in size, that is separated from its 217 photomultiplier readout by a 4 cm air gap. Utilizing a matrix readout method in conjunction with the restricted detection range of the photomultipliers, due to total-reflection at the scintillator/air interface, the angular dependend resolution is about 1 cm. S3 also acts as stop detector for a time-of-flight measurement between S1 and S3, which are situated at a distance of roughly 9 m [78], the time resolution is 195 - 265 ps.

3.1.4.4 Monitor scintillator S5

In the target region a single sided readout monitor scintillator, 72 x 230 x 4 mm^3 in size, is used in coincidence with S1 to detect backwards scattered protons and deuterons.

3.1.4.5 Monitor pad detector $S5_{mon}$

To achieve an angular dependend analysis of the elastically scattered protons detected in the target region by the monitor scintillator, a silicon pad detector [79] is installed behind the S5. With a total area of 20.86 x 5.98 cm^2, 144 silicon pads, of size 4.5 x 22.6 mm^2 each, are arranged in three overlapping rows of 48 pads each to avoid insensitive spots throughout the detection area. Every four pads are combined into a detector module. Readout is performed by AMPLEX-16 chips, also used for a second, larger silicon pad detector inside the dipol gap.

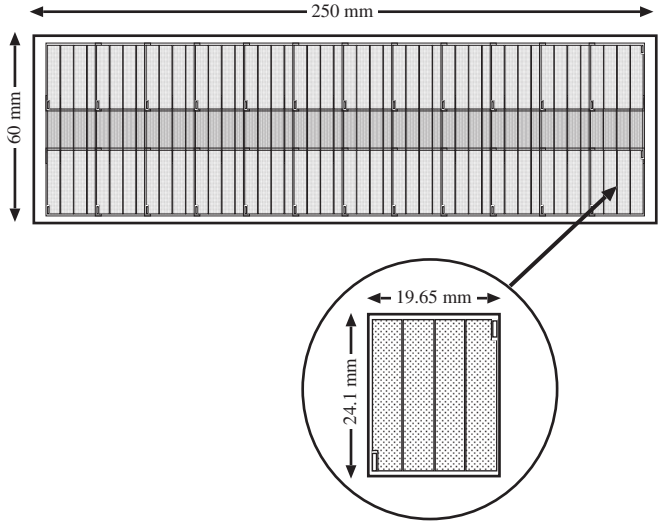

Figure 3.9 Make-up of a silicon pad detector. Each module, consisting of four pads, is inclined by 3.6° compared to the vertical and overlapps with adjacent modules by 1 mm horizontally and 4 mm vertically. The middle of the three rows is lowered by 2 mm.

3.1.5 Data acquisition

The COSY-11 data acquisition system (DAQ) is provided by the Zentrallabor für Elektronik (ZEL) of the Forschungszentrum Jülich. It has been completely changed in between the two measurement periods and both systems were based on the current hard- and software standards for COSY-experiment at the time they were developed [80].

Both systems were build according to the client/server concept, utilizing CAMAC and FASTBUS technology for digitizing of event data. During the first measurement period the server side was handeled by a VME system, with intelligent multi-processor controllers running the realtime operating system OS-9. Whereas the later DAQ was controlled by an industrial PC system running NetBSD.

The client side consisted of Digital Alpha Stations running Tru64 UNIX and communication with the server processes took place via TCP/IP over standard ethernet. For details see [58], [81], [82].

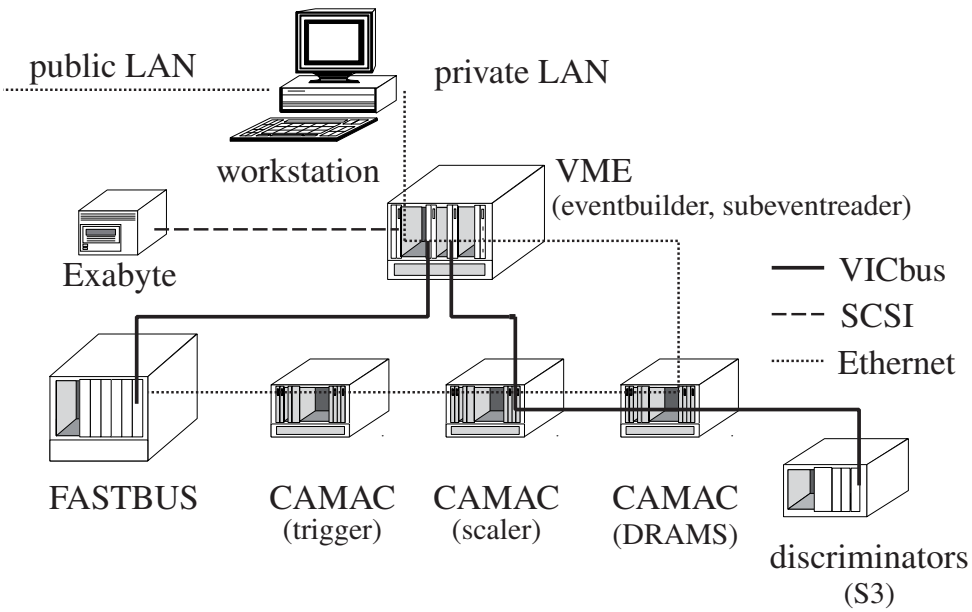

Figure 3.10 COSY-11 data aquisition system during the 11 and 40 MeV measurements.

3.2 Trigger

The wealth of data produced during experiment has to be filtered, before reading out the detection system, otherwise the deadtime of the data aquisition system would highly impede the measurement. Therefore the read out is only startet when certain conditions, called triggers, are met.

During this experiment individual triggers were used to acquire events from different reaction channels to be recorded by the data acquisition system.

$$T_9 = T_{He} \vee \frac{T_{pd_{mon}}}{2^n} \vee \frac{T_{t\pi^+}}{2^n} \vee \frac{T_{S1_{\mu=1}}}{2^n} \vee T_{pulser} \tag{3.2}$$

Besides the main trigger, for the reaction investigated in this analysis and an auxiliar trigger necessary for normalization purposes, both described below, three additional trigger were included.

T_{pulser} is a diagnostic trigger included in every experiment to have a periodic read out of the detectorsystem, as a time stamp information, even if there is a very low event rate.

$T_{t\pi^+}$ reads out the detector system, when conditions for reactions of type $pd \rightarrow t\,\pi^+\,X^0$ are met. As this reaction is only recorded in parallel for the opertunity of a later analysis, it is prescaled by 2^n, so only each 2^{nth} event of this reaction is recorded, not to put stress on the data acquisition system and not to interfere with the recording of the main reaction.

$T_{S1_{\mu=1}}$ is a generic trigger, also part of the main trigger, that records single track events, with only one hit in the scitillator hodoscope S1. Like the $T_{t\pi^+}$ trigger it is also prescaled.

3.2.1 Main Trigger

The primary trigger for the reaction $pd \rightarrow {}^3He\,\eta$, denoted as T_{He}, was adjusted to select events, where a ^{3}He-nucleus was produced (e.g. $pd \rightarrow {}^3He\,X^0$):

$$T_{He} = \{Sl_{\mu\geq 2} \vee (Sl_{\mu=high}^{1\ldots5} \wedge Sl_{\mu=1})\} \wedge \{S3_{\mu_{PM}\geq 3} \vee S(7_{\mu\geq 1} \vee S4_{S3})\} \tag{3.3}$$

As given in Eq. 3.3, the trigger condition was, according to acceptance, requesting either a single hit (multiplicity $\mu = 1$) in one of the first five segments of the scintillation detector S1. Furthermore with an energy deposition in the scintillating material above a certain threshold, the so called high-amplitude (μ = high) (Fig. 3.11). Alternatively a double-hit ($\mu \geq 2$) in S1 to accept additional hits in detector regions, where two adjacent scintillator laths overlap. In addition to these criteria, a hit in the stop detector system of the time-of-flight arrangement was requested. Therefore, a hit in the scintillator wall S3 with at least three photomultipliers firing ($S3_{\mu_{PM}\geq 3}$) was requested or a hit in the scintillation detectors S7 or $S4_{S3}$, which were used to extend the angular acceptance of the S3 detector for high momentum ^{3}He-nuclei.

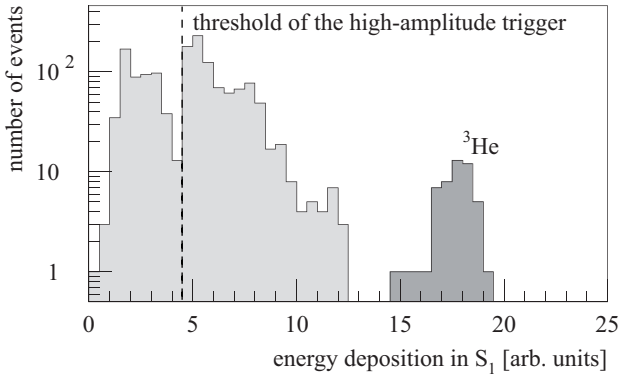

Figure 3.11 Raw events selected by the hardware triggers. The signal of the ^{3}He is already clearly visible in the raw data. Events recorded below the threshold of the high-amplitude trigger (dashed line) result either from overlap hits in the detector S1 or other triggers than T_{He}.

3.2.2 Auxiliar Trigger

Besides the main trigger several other triggers were used prescaled during the experiment to record additional reaction channels. One important auxiliary trigger is $T_{pd_{mon}}$ for recording the proton-deuteron elastic scattering pd → pd, used for normalization purposes to obtain total cross sections:

$$T_{pd_{mon}} = \frac{1}{2^n} \cdot (Sl_{\mu = 1} \wedge S5) \tag{3.4}$$

To detect events of elastically scattered protons and deuterons, a single hit in the scintillation detector S1 was requested in coincidence with a hit in the scintillation detector S5 (Eq. 3.4). Depending on the experimental situation, different prescaling factors (2^n) were chosen (Table 4.2 on page 74).

4 Data Analysis

The reaction channel pd $\rightarrow$ ^{3}He η was studied by detecting the emitted ^{3}He nuclei and identifying the η mesons through the missing-mass technique. To obtain cross sections, the pd $\rightarrow$ ^{3}He X data are normalized using the results on the elastic pd $\rightarrow$ pd scattering that was measured in parallel.

The values of particle masses used in this analysis are summarized in Tab. 4.1, presenting the value by the time the experiment was analyzed [83].

particle	**mass [GeV/c^2]**
p	0.93827231
d	1.87561339
^{3}He	2.808392
η	0.5473
$\pi^{\pm}$	0.13956995

Table 4.1 Particle masses used for this analysis [83], the mass of the ^{3}He nucleus has been calculated from [84] and [83].

4.1 Main Reaction

4.1.1 Event Selection

To separate ^{3}He events from background of pions, protons, deuterons and tritons the ΔE/p information was exploited. Although the ΔE information alone is sufficient to separate the ^{3}He events from background, as can be seen in the raw spectrum (Fig. 4.1), a special threshold for each of the segments of S1 would have been necessary. The reconstructed momentum information was used allowing a fine grained presentation in the ΔE/p plot. This leads to a clear ^{3}He signal due to its high-energy deposition in scintillating material [85]. This positive identification enables to determine the four-momentum vectors

$$P_{^3He} = \left(\sqrt{p^2_{^3He} + m^2_{^3He}}, \vec{p}_{^3He}\right) \tag{4.1}$$

of extracted ^{3}He events from background. The momentum $\vec{p}_{^3He}$, reconstructed by tracing back the tracks in the drift chambers through the well known magnetc field, is measured with a precision of better than 1% [42].

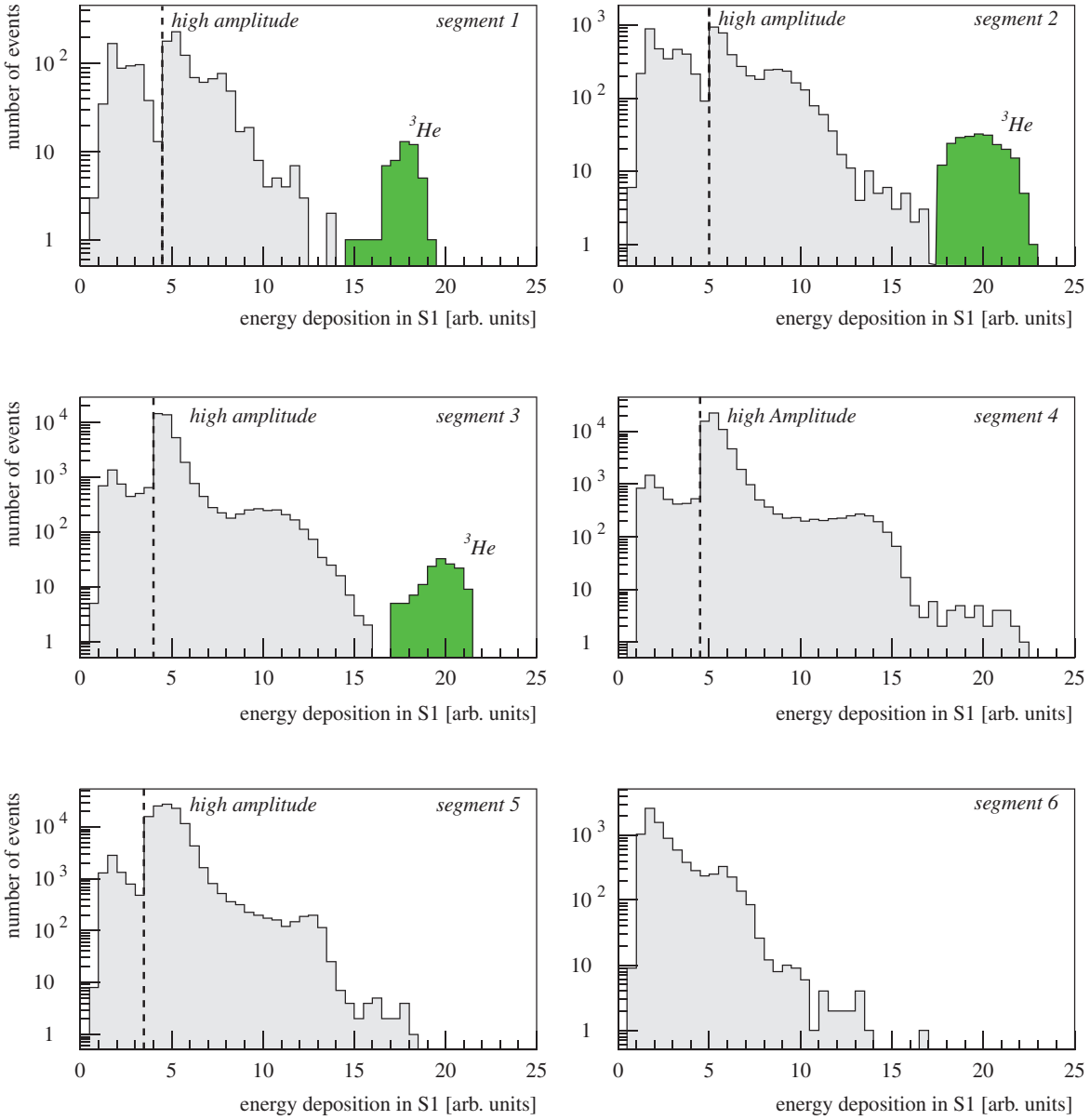

Figure 4.1 Hardware cuts during experiment in the first five segments of S1 (p_{beam} = 1.593 GeV/c). The dashed line indicates the so called high-amplitude of the $S1_{\mu=high}$ trigger. Events recognized below this threshold are due to the additional triggers used. As expected from Monte Carlo simulation, ^{3}He events originating from the reaction of interest only become prominent in the first segements of the S1 detector and degrade with higher segment numbers, correspondig to larger scattering angles. The value of the high amplitude threshold is not arbitrary, but has been determined during a short test measurement. It was choosen to be conservatively low, as can be seen from the safe distance between the ^{3}He signal and the threshold.

In Fig. 4.2 through Fig. 4.6 the event selection process for each of the five measured excess energies is presented in detail. The ^{3}He is identified purely by the energy deposition of passing particles in the scintiallator hodoscope S1 in correlation to the time-of-flight of the particles between the S1 and S3 as start and stop detectors or the reconstructed momentum of the particle from the track reconstruction in the drift chamber system D1 & D2. Panels a) and b) of each figure present the raw data with an energy deposition of more than 10 arb. units on the ordinate. The energy information from S1 has not been calibrated to provide absolute values of ΔE, as only the relative energy deposition of different particles in the detector is necessary to provide a solid event separation.

A peninsula of events is visible on top of a broad background spectum, arising from pions, protons, deuterons and tritons. At the same momentum, the ^{3}He deposits a larger amount of energy in the scintiallation material, than any of the background particles due to its higher charge and mass. In the ΔE/p presentation of panel b) the region of ^{3}He events can be easily choosen by the cut indicated as a white line. The success of such a cut can be visualized, when switching back to the ΔE/tof presentation, as was done in panel c), leading to a much cleaner spectrum. Nevertheless, a very small contamination from background particles among the selected ^{3}He-nuclei is evident, when calculating the reconstructed mass of the ^{3}He:

$$m_{^3\mathrm{He}} = \frac{p_{^3\mathrm{He}}}{\beta \cdot \gamma \cdot c} \tag{4.2}$$

as presented in panel d) and especially when comparing it to expectations from Monte Carlo simulations (simulation scaled to fit the height of the experimental signal). The time-of-flight is used to obtain the velocity information v that in turn is used to calculate the relativistic variables $\beta \cdot \gamma \cdot c$, with $\beta = v/c$ and $\gamma = 1/(\sqrt{1-\beta^2})$, c is the speed of light. The discrepancy in the mean of some of these plots to the ^{3}He mass of 2.808392 GeV/c^2 used for this analysis must be attributed to the lack of calibration performed on the time-of-flight measurement. The fact that this is only present in the Q = 10.8 MeV and Q = 40.6 MeV is well understood, as both measurements have taken place during the same beam time for a first pd $\rightarrow$ ^{3}He η measurement at COSY-11. Again, as with the ΔE information in S1, the time-of-flight is only used to see the relative behaviour off different particles detected. It does not impose any deficiency to the following missing mass analysis, as it is not used in that analysis.

The integrated missing mass spectrum for the selected pd $\rightarrow$ ^{3}He X^0 events is presented in panel e), where X^0 can be a single not detected particle, as the η meson, or a combination of different lighter particles (e.g. $\pi\pi$, $\pi\pi\pi$, $\pi\pi\pi\pi$), as energy permits. These backround reactions were investigated in detail during the angular dependend missing mass analysis and are presented in Sec. 4.1.2. In any case of the five excess energies, a signal in the range of the η mass

is visible on top of the background. The η signal is less clear visible at the highest and lowest energies, due to the limited statistics far from threshold (Q_η= 40.6 MeV) and closeness to the cinematical limit (Q_η= 5 MeV), respectively.

Besides the experiment data (gray shaded curve), also a Monte Carlo simulation for pd $\rightarrow$ ^{3}He η is included here. The simulation for panel e) has been scaled according to the number of η-events extracted after the background subtraction process in the summation of the angular dependend analysis.

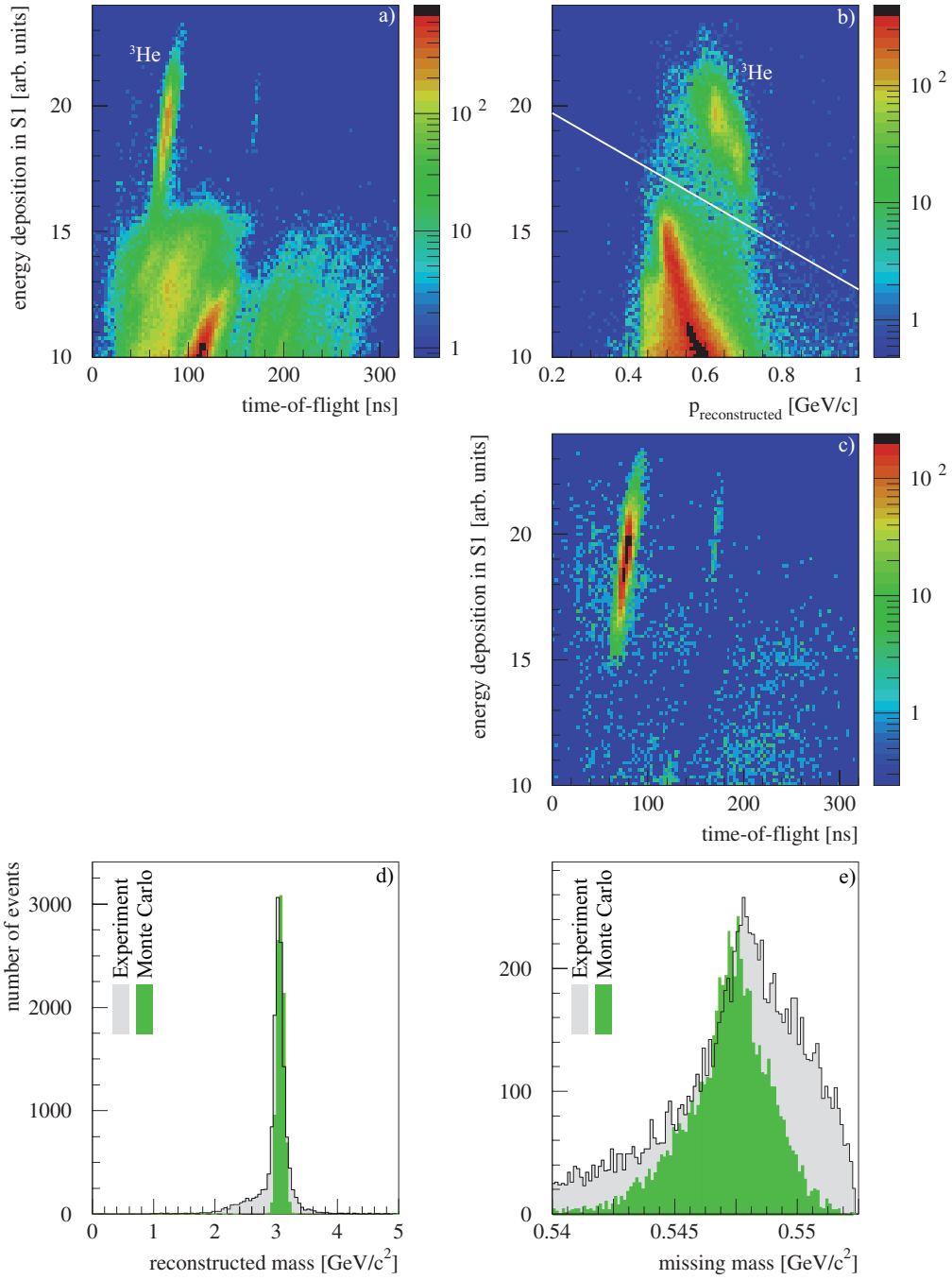

Figure 4.2 ^{3}He event selection for p_{beam} = 1.581 GeV/c (Q_η = 5 MeV). a) Raw spectrum of recorded data shown in the ΔE/tof presentation. An initial cut of 10 arb. units in the energy deposition in S1 has already been applied. The ^{3}He events are visible in the raw data already. b) Same data in the ΔE/p presentation. Again the ^{3}He signal is cleary visible, allowing to cut off background reactions, as indicated by the white line. c) ΔE/tof presentation after applying the ΔE/p cut. d) Reconstructed mass of the selected ^{3}He. The reconstruction is in good agreement with expectations from Monte Carlo simulations with only little remaining background. e) Missing mass calculated for the selected ^{3}He. A signal in the region of the η mass is visible on top of a large background, arising from multi-pion production, close to the cinematical limit. A small discrepancy in the position of the η peak between simulation and experiment is resolved almost completely in the angular dependend background subtraction analysis, as depicted in the result of Fig. 4.10.

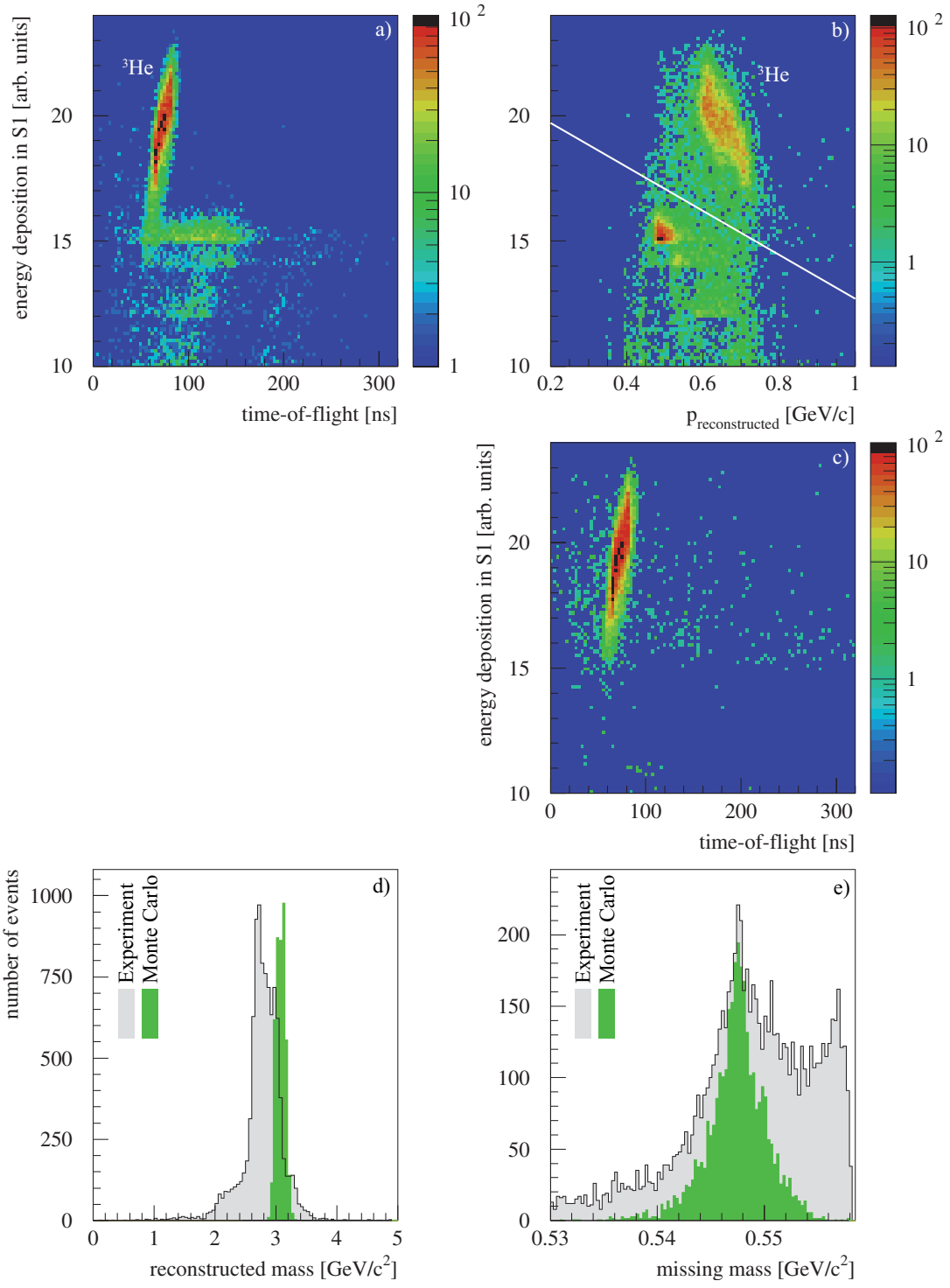

Figure 4.3 Same as Fig. 4.2, but for p_{beam} = 1.593 GeV/c (Q_η = 10.8 MeV). d) The reconstruction differs from expectations from Monte Carlo simulations and shows a higher level of remaining background. The difference in timing of the time-of-flight measurement can be attributed to an offset in the S1-S3 timing, but imposes no limitation on the accuracy of the analysis, as this information is not leveraged for the missing mass analysis. The same situation is found for the Q_η = 40.6 MeV data, taken during the same beam time. e) The position of the η peak in the calculated missing mass spectrum is in good agreement with the expectations from Monte Carlo simulations.

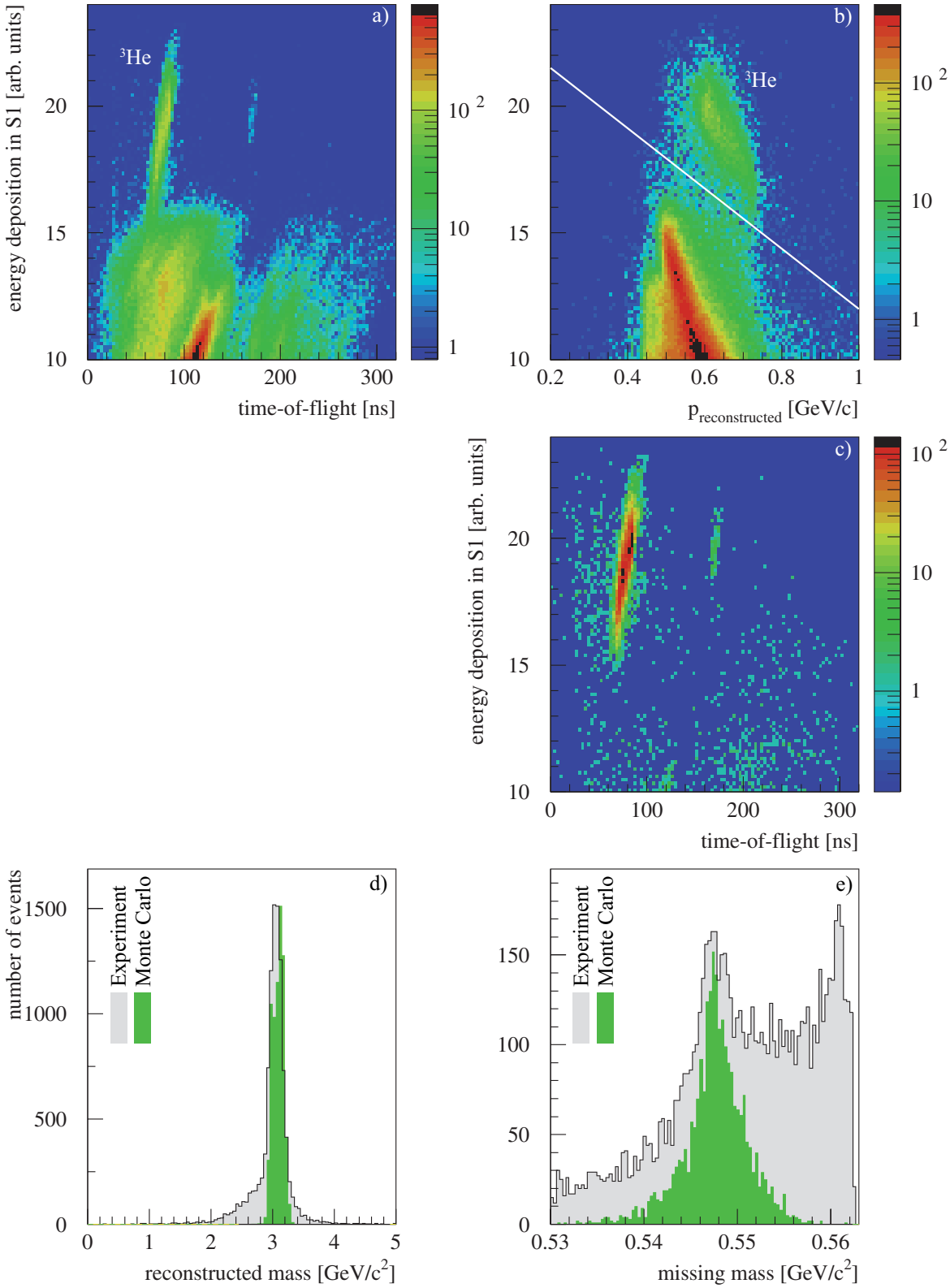

Figure 4.4 Same as Fig. 4.2, but for p_{beam} = 1.602 GeV/c (Q_η = 15.1 MeV). e) The position of the η peak in the calculated missing mass spectrum is in good agreement with the expectations from Monte Carlo simulations.

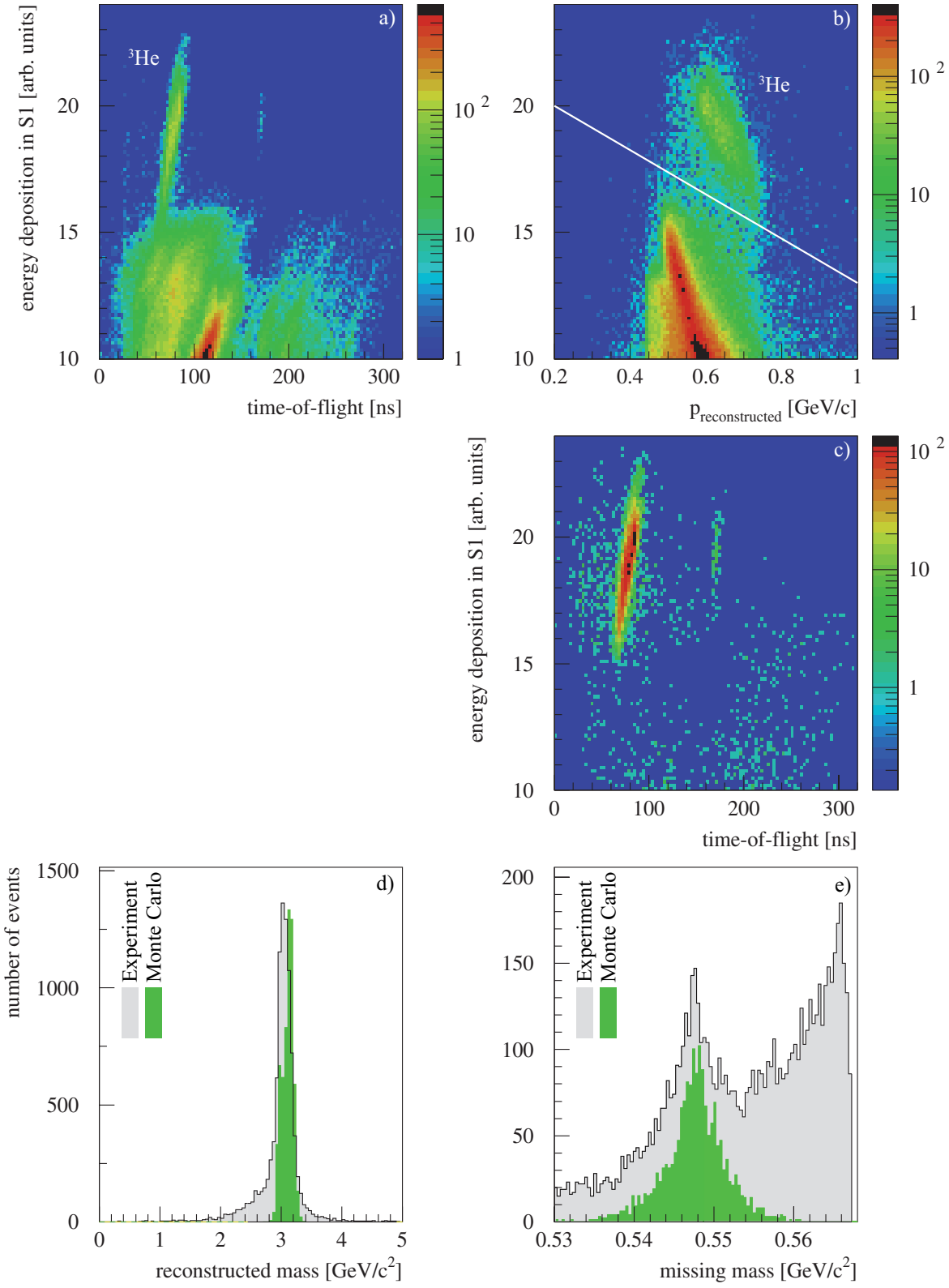

Figure 4.5 Same as Fig. 4.2, but for p_{beam} = 1.612 GeV/c (Q_η = 19.9 MeV). e) The position of the η peak in the calculated missing mass spectrum is in good agreement with the expectations from Monte Carlo simulations.

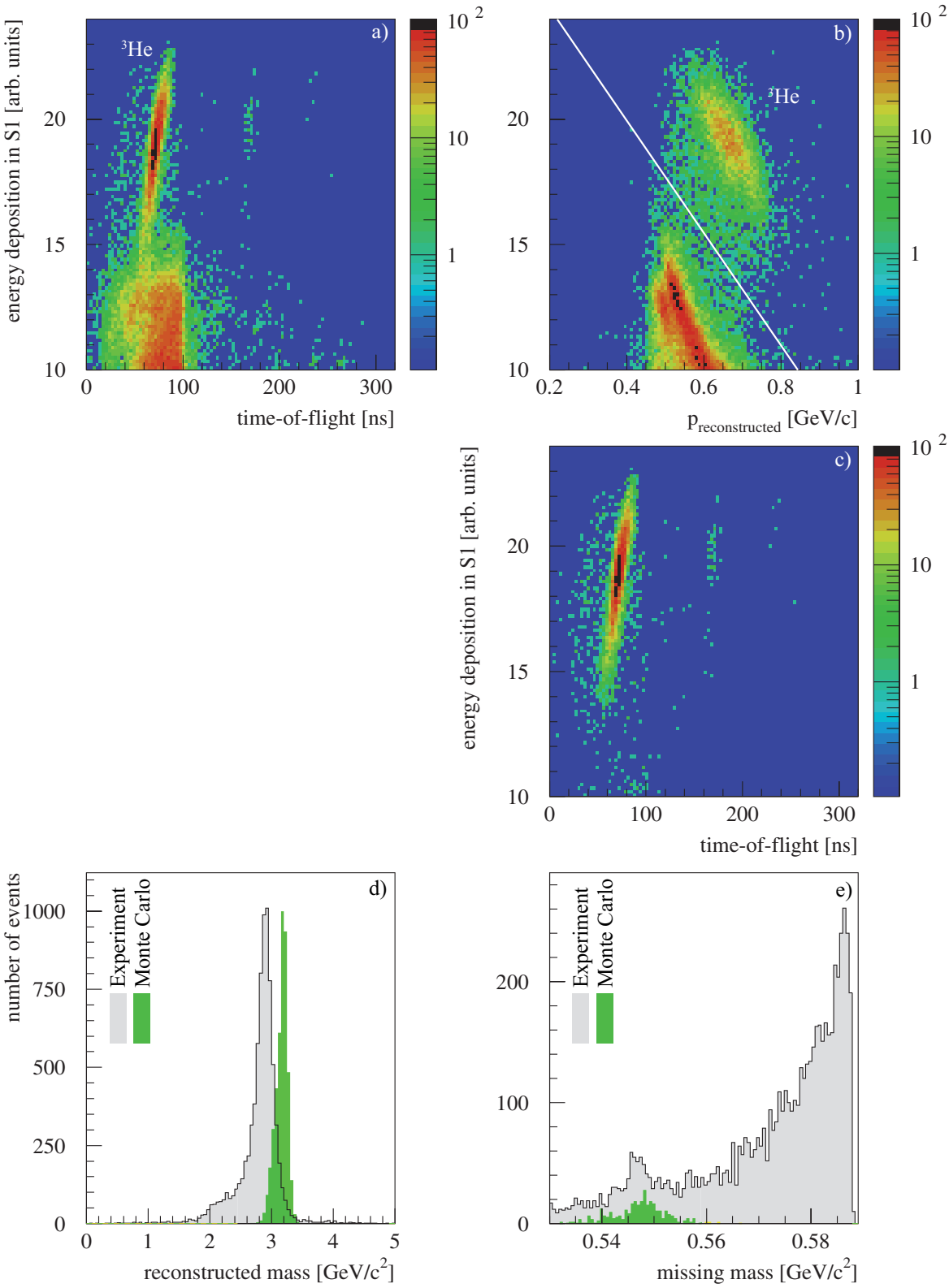

Figure 4.6 Same as Fig. 4.3, but for p_{beam} = 1.655 GeV/c (Q_η = 40.6 MeV).

4.1.2 Missing Mass Analysis

For pd $\rightarrow$ ^{3}He X reactions, the four-momentum vector P_X of the unobserved particle system X can be expressed by the known four-momentum vectors of the beam protons and the target deuterons (P_p, P_d) and the measured one of the detected ^{3}He-nuclei (P_{He}):

$$P_X = (P_p + P_d) - P_{He} \tag{4.3}$$

The (missing) mass of the unobserved system X results in:

$$m_X = |P_X| \tag{4.4}$$

The missing-mass plot of the pd $\rightarrow$ ^{3}He X reaction calculated for the selected ^{3}He events exhibits a clearly visible peak at the mass of the η meson on top of a background originating from multipion production. The results presented in Fig. 4.7 are the summation of the angular dependend missing mass analysis (presented later) that was performed for the determination of differential cross sections and angular distributions of each of the five measured energy points.

4.1.2.1 Investigation of the physical background

The background can be reproduced well by phase-space Monte Carlo simulations of the pd $\rightarrow$ ^{3}He n $\cdot$ π ($n \geq 2$) reaction channels at the corresponding beam energies (Fig. 4.7). The Monte Carlo simulation of two/three and four pion production was fit in magnitude to the experimental data in the region outside the η signal. The two- and three-pion production Monte Carlo pd $\rightarrow$ ^{3}He $\pi\pi/\pi\pi\pi$ were scaled to describe the leading tail of the data, whereas the four-pion Monte Carlo pd $\rightarrow$ ^{3}He $\pi\pi\pi\pi$ was scaled to describe the data at the kinematic limit.

The simulations, based on the GEANT 3.21 code [86], have been carried out separately for several charged and uncharged multipion channels in the angular bins chosen for the determination of the differential cross sections and angular distributions (example in Fig. 4.8). Neither the charge of the produced pions nor the two- and three-pion production process can be distinguished in the shape of the missing-mass distribution (Fig. 4.8, Fig. 4.9) in our limited range. This is because of the large excess energy for multipion production at the η threshold, where the shape is dominated by the acceptance of the detection system. In the case of the pp $\rightarrow$ pp η channel, this effect was discussed in [87].

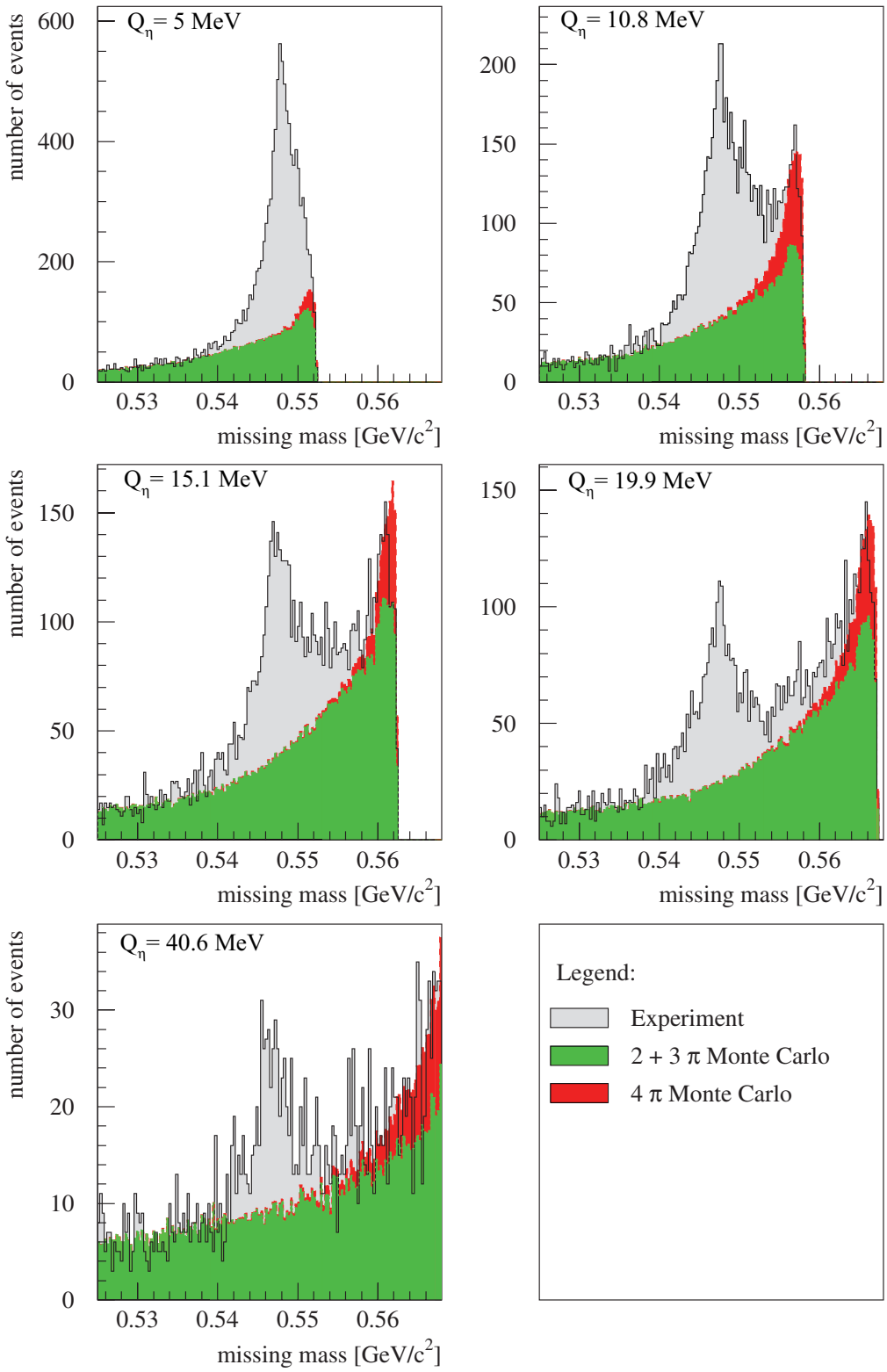

Figure 4.7 Missing-mass distribution obtained for ^{3}He events. On top of the background, a peak in the range of the eta-mass ($m_\eta = 0.5473$ GeV/c^2) is quite prominent. By combining Monte Carlo events from reactions of the type pd $\rightarrow$ ^{3}He n $\cdot$ π (n $\geq$ 2) the background observed in the experiment can be described very well. The simulation was fit in magnitude to the experimental data in the region outside the η signal; for details see text.

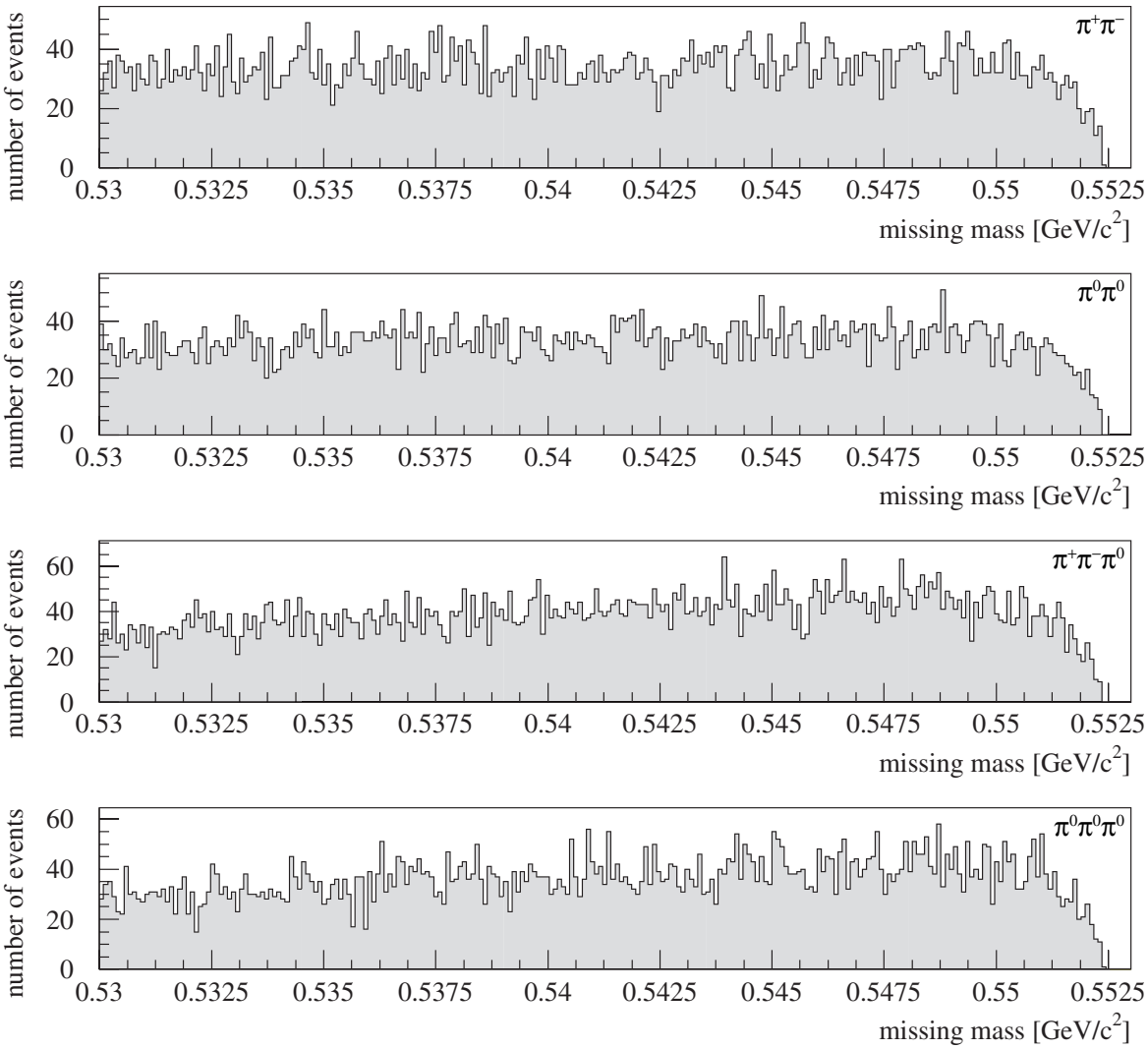

Figure 4.8 Phase space Monte Carlo simulation of different multipion channels at p_{beam} = 1.581 GeV and $-1 \leq \cos\theta^* < -0.8$ of the produced ^{3}He. The shape of each of the missing mass distributions for the possible combinations of charged and uncharged pions in the two and three pion channels of the pd $\rightarrow$ ^{3}He X reactions is similar, as is obvious from Fig. 4.9, where the ratio of the charged and uncharged channels is presented.

By subtracting the scaled Monte Carlo generated multipion data from the experimental distribution, a clean missing mass peak remains with a width of less than 6 MeV (full width at half maximum) which is in very good agreement with expectations from Monte Carlo simulations of the pd $\rightarrow$ ^{3}He η channel (Fig. 4.10). As presented in Fig. 4.7, the combined two- and three-pion production Monte Carlo simulation was scaled to describe the leading tail of the data, whereas the four-pion simulation was scaled to describe the data at the kinematical limit.

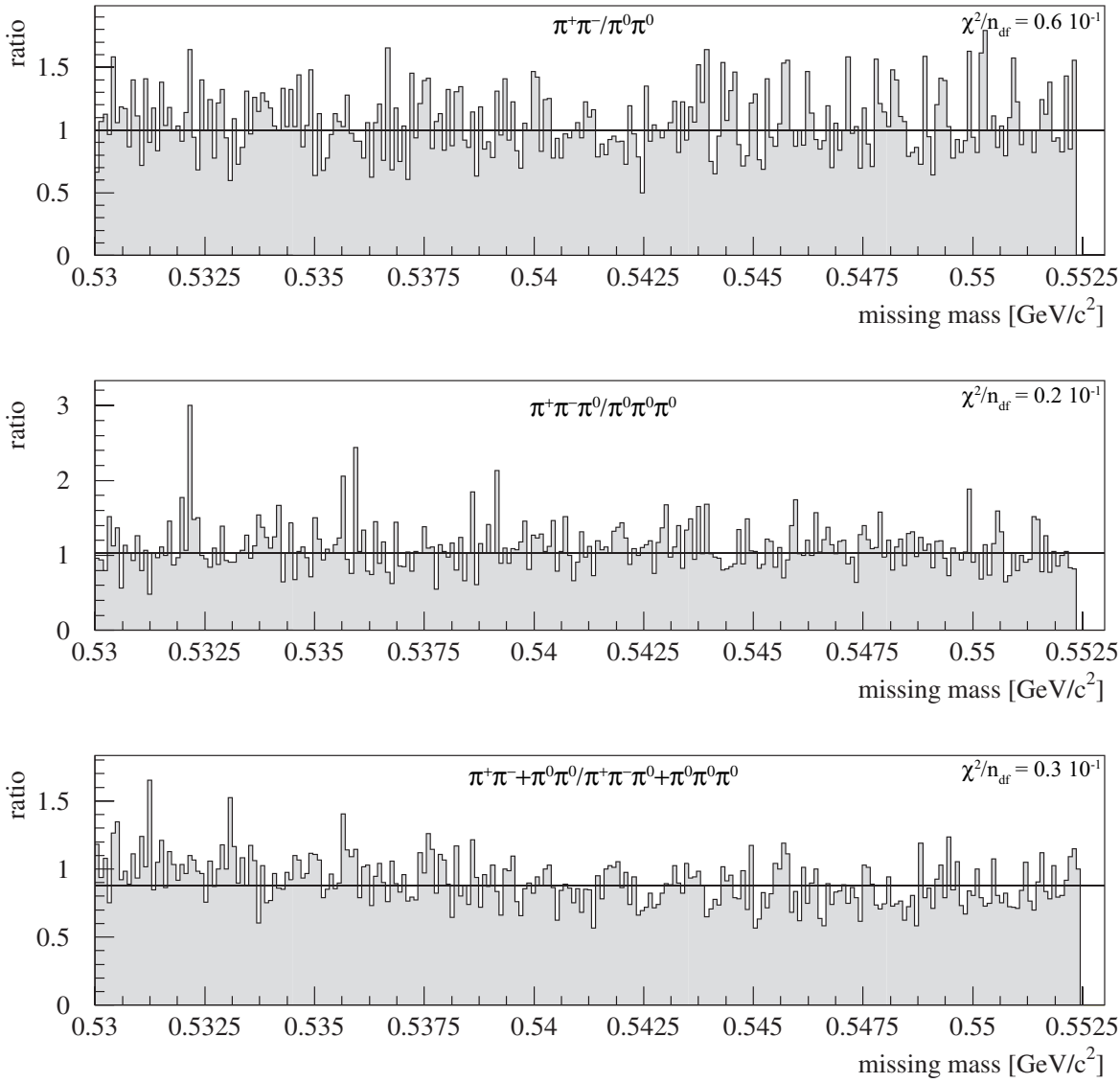

Figure 4.9 Ratio of the different multipion channels presented in Fig. 4.8. When deriving the ratio of the first and second missing mass distribution of Fig. 4.8, the ratio between the charged and uncharged two pion production is calculated, leading to a flat distribution in the order of 1, when fitting a straight line to the spectrum (upper panel). Same is done for the third and fourth missing mass distribution of Fig. 4.8, calculation the same ratio for the charged and uncharged three pion productions (mid panel). In the lower panel, the sum of the charged and uncharged two pion production is divided by the sum of the charged and uncharged three pion production, also leading in good approximation to a flat distribution.

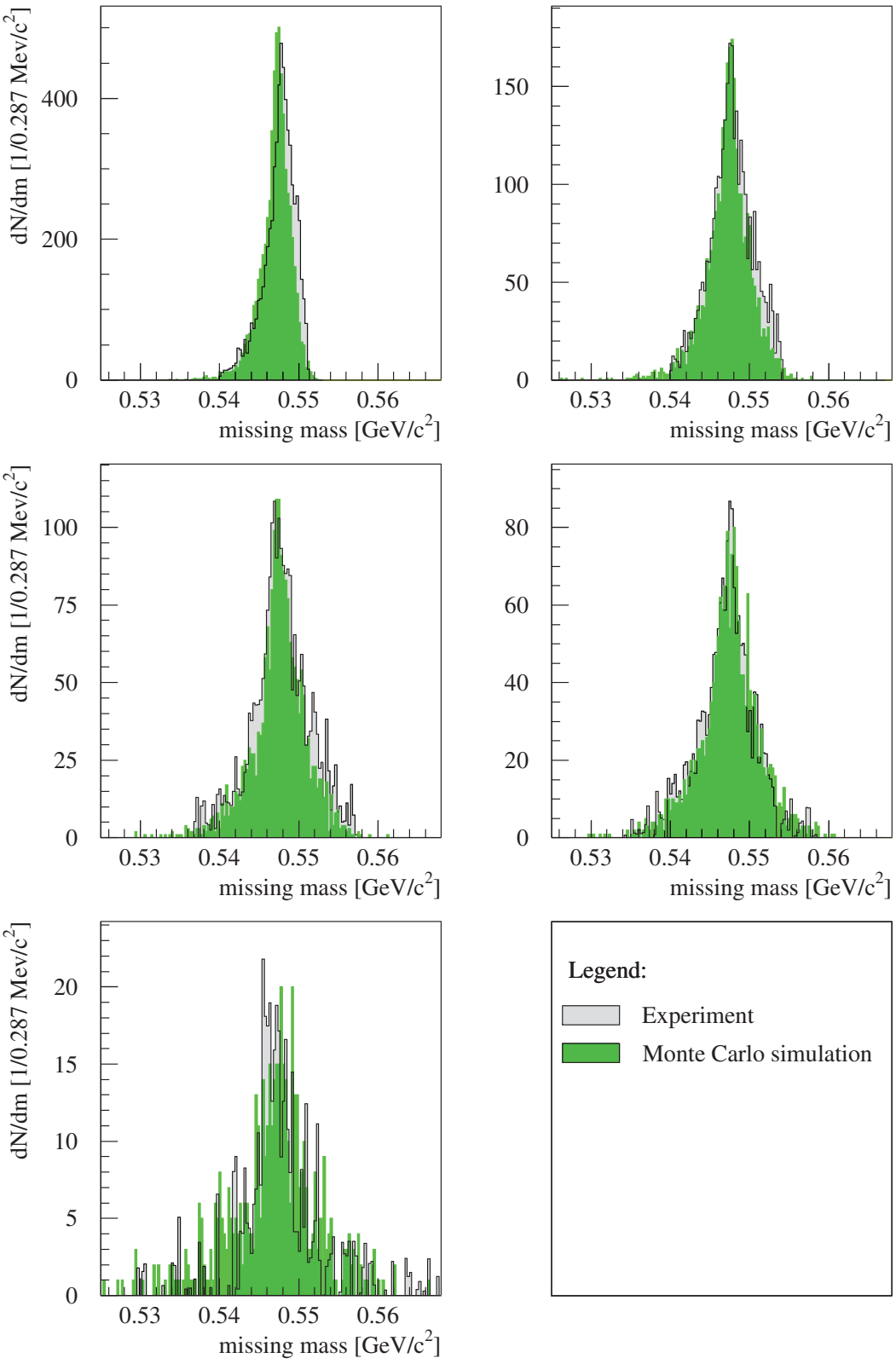

Figure 4.10 Missing-mass distribution for the pd $\rightarrow$ ^{3}He η reaction at different excess energies. The spectra have been obtained by a summing up the background-subtracted missing-mass spectra of the different angular bins in the differential cross section analysis.

4.1.2.2 Angular dependend analysis of the missing mass spectra

To evaluate differential cross sections, the missing-mass technique was used for each angular bin, and the number of detected η mesons was obtained separately by subtracting the background (Fig. 4.11 - Fig. 4.15, left hand side) as for the total spectrum of Fig. 4.7. The Monte Carlo results of both the combined two- and three-pion production (Fig. 4.11 - Fig. 4.15, green shaded curve) and the the results of the four pion production (Fig. 4.11 - Fig. 4.15, red shaded curve) were scaled to describe the experimental data (Fig. 4.11 - Fig. 4.15, grey shaded curve) outside the region of the η signal in the $-0.6 \leq \cos\theta^* < -0.4$ bin. The combined two- and three-pion production Monte Carlo simulations were scaled to describe the leading tail oft the data, whereas the four-pion Monte Carlo simulation was scaled to describe the data at the kinematic limit. The same scaling factors determined for this single bin were then used for every other bin at the same excess energy. As these are phase space Monte Carlos, and the energy range of the measurements is high above the respective pion production threshold, it was assumed that a angular dependend analysis of the background in each bin can be ommited. Due to the fact, that according to phase space, there are no angular dependencies in the emission of the produced ^{3}He, when moving so far above the production threshold it was ssumed that the shape is dominated by the acceptance of the detection system [87].

The ambiguity in the scaling factors for the background subtraction is reflected in the systematic uncertainty of the number of extracted η events and has been determined, by investigating the possible maximum and minimum scaling factors for two/three and four pion Monte Carlo separately. The means of the factors were choosen, presented in Fig. 4.11 through Fig. 4.15, and the deviation from the mean for each pion production was chosen as uncertainty. By summing up the background subtracted experimental data, as well as the scaled two/three and four pion Monte Carlo simulation respectively, of all angular bins, the presentation of Fig. 4.7 was achieved.

On the right hands side of Fig. 4.11 - Fig. 4.15 the results of the background subtraction in every bin is presented (grey shaded curve) and compared to the expectation from Monte Carlo simulations (magenta shaded curve) on the pd $\rightarrow$ ^{3}He η reaction at respective beam energies and angles. The simulation was scaled to have the same number of events in the Monte Carlo peak as in the experimental data. By comparing the experimental data to the simulation, it is obvious that both are in good agreement in most cases and only differ significantly in angular bins were the statistics are very limited, e.g. in the forward and backward bin at the highest excess energy (Fig. 4.15, first and last bin). This allowed to set additional cuts on the missing mass for each bin and exclude regions (Fig. 4.11 - Fig. 4.15, yellow hatched areas) for which it is ovious, that they do not belong to the η signal. The position of the η peak in some angular bins, for example at $Q_\eta = 5$ MeV, $0 \leq \cos\theta^* < 1$ (Fig. 4.11, lower right), differs from expectations by Monte Carlo simulations. But as only the sum spectra are utilized in the determination of the total cross sec-

tion and the big width of this bin already adds a „large“ uncertainty in the determination of the differential cross section, this has only very limited influence on the result of this analysis, as is obvious from the integrated spectra (Fig. 4.10).

The background subtraction based on phase space Monte Carlo simulation is not a perfect description for the background in every angular bin, for example for the $0 \leq \cos\theta^* < 1$ bin at $Q_\eta = 10.8$ MeV (Fig. 4.12, lower right), the four pion background seems to be set to low as a shark tail is still visible after the backgrund subtraction. The best way to solve this would be to carry out an additional measurement of the pd $\rightarrow$ ^{3}He X reaction, analyzing data consistently to the presented analysis just below the η threshold. This would remove the dependency on phase space Monte Carlo to describe the background and no a priori assumption of the background reactions would be neccessary. It would however cause a not easily justifiable additional experimental effort, with only limited improvement of the results of the procedure. Therefore the more efficient way of limiting the range of the η peak by cuts on the accepted missing mass region was chosen, to overcome this challenge.

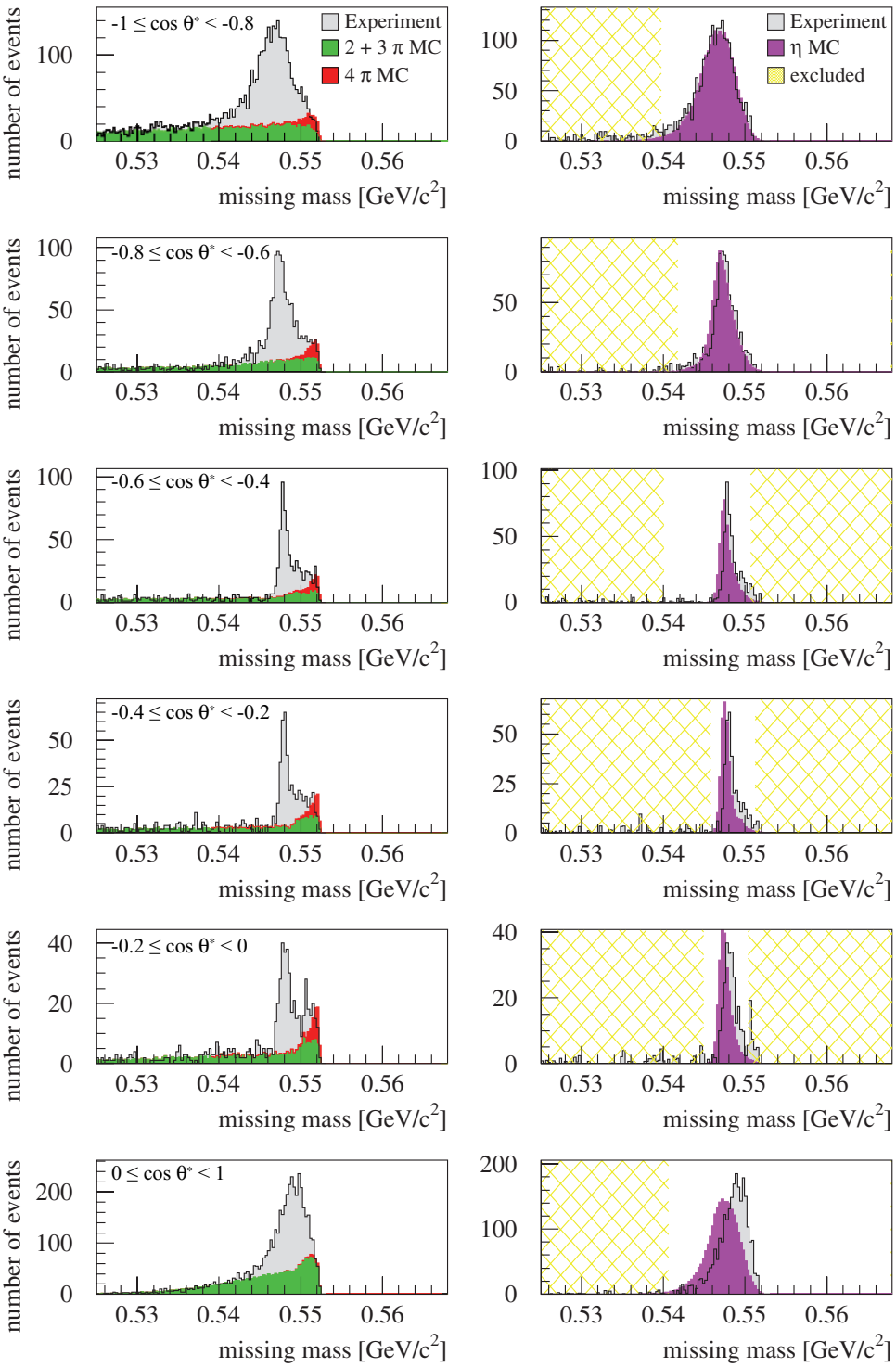

Figure 4.11 Background subtraction in the angular bins at p_{beam} = 1.581 GeV/c (Q_η = 5 MeV). Left hand side: The combination of two/three (green shaded curve) and four (red shaded curve) pion Monte Carlo simulations scaled to fit the experimental data (grey shaded curve) outside the η signal describes the background quite good in each of the angular bins. Right hand side: The background subtracted η signal (grey shaded curve) is in good agreement with the expectation from Monte Carlo simulations (magenta shaded curve). Based on the comparison of data and simulation, the yellow hatched region was excluded from the differential cross section evaluation. For details see text.

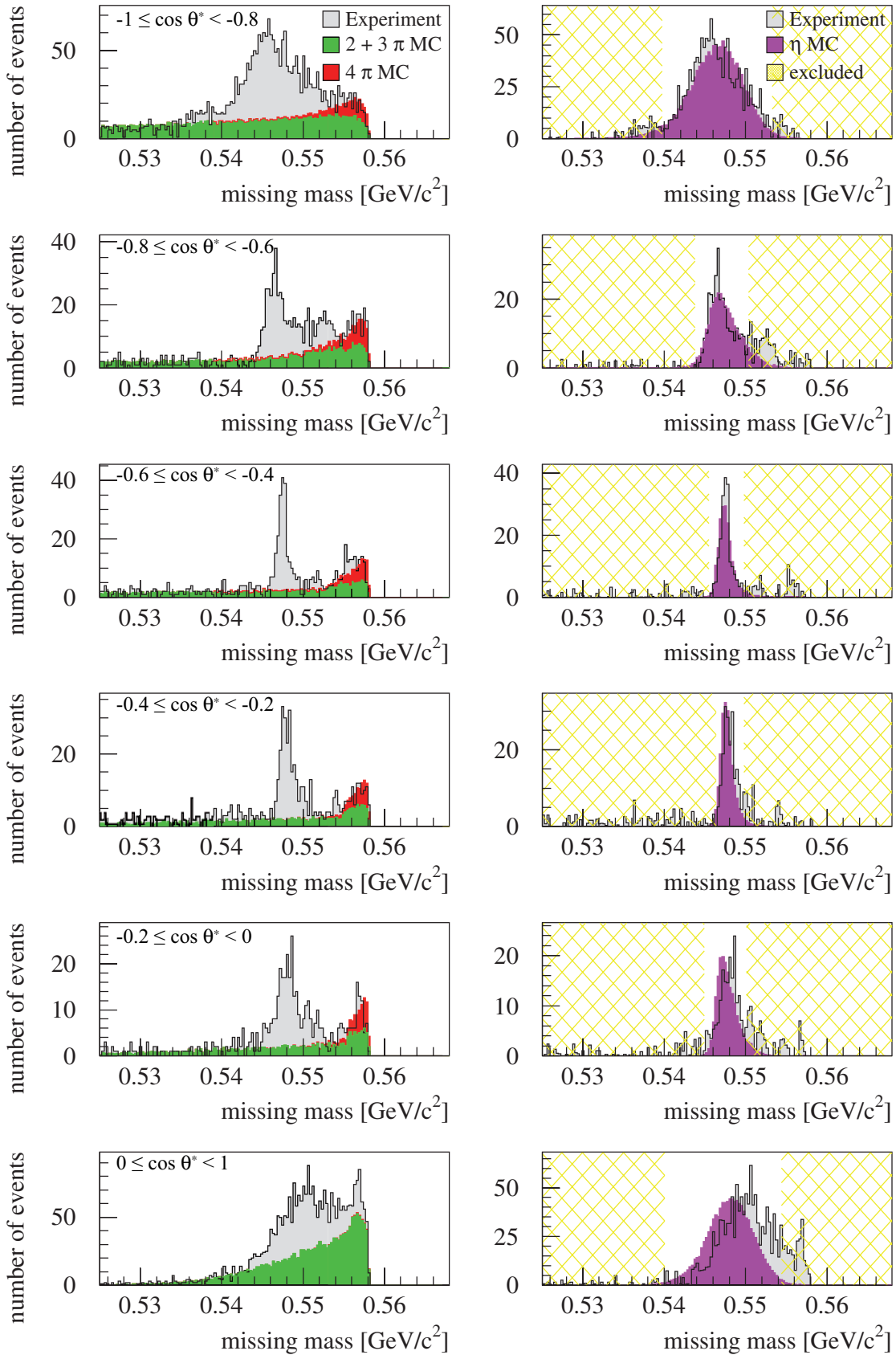

Figure 4.12 Same as Fig. 4.11, but at p_{beam} = 1.593 GeV/c (Q_η = 10.8 MeV).

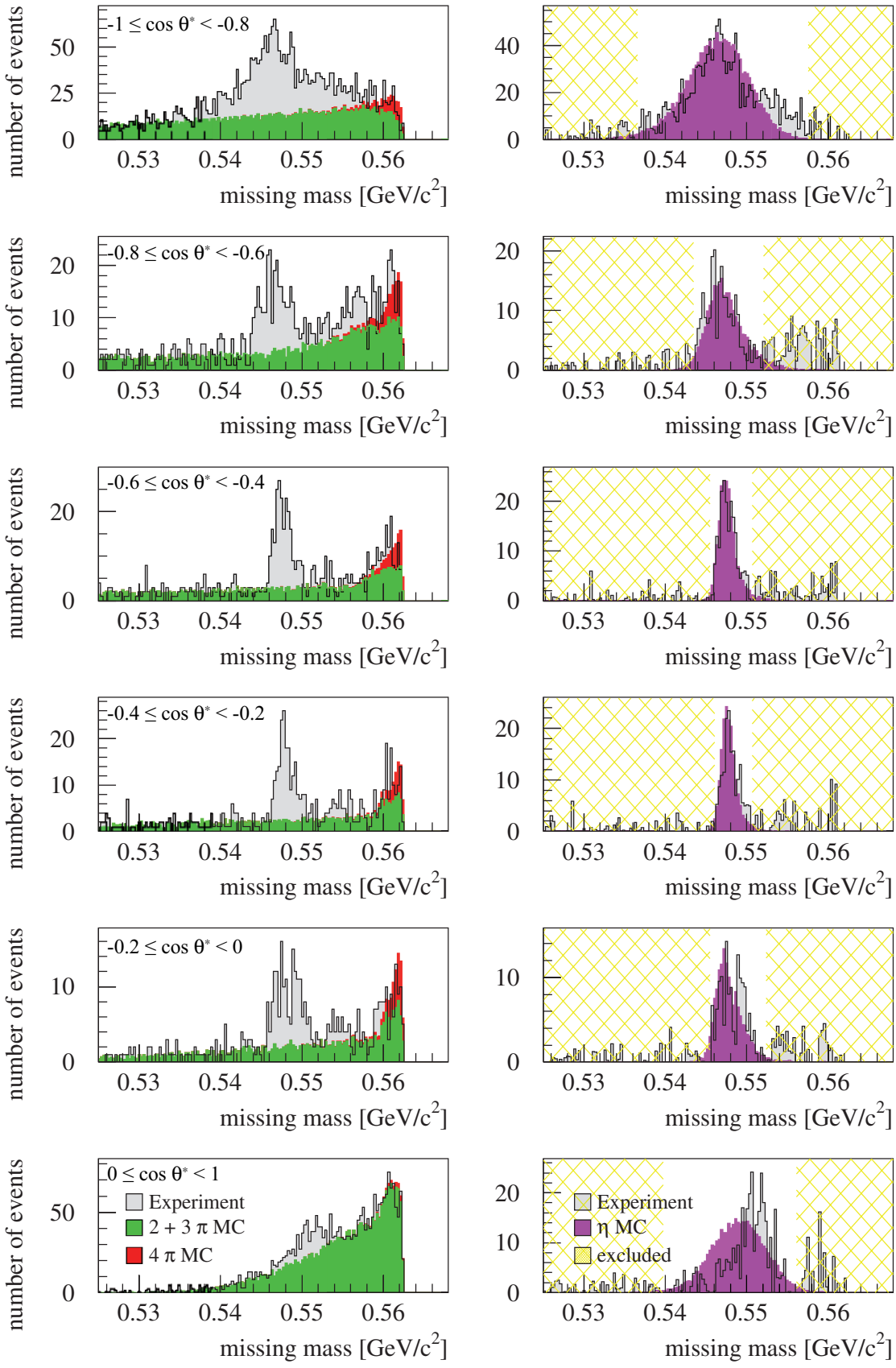

Figure 4.13 Same as Fig. 4.11, but at p_{beam} = 1.602 GeV/c (Q_η = 15.1 MeV).

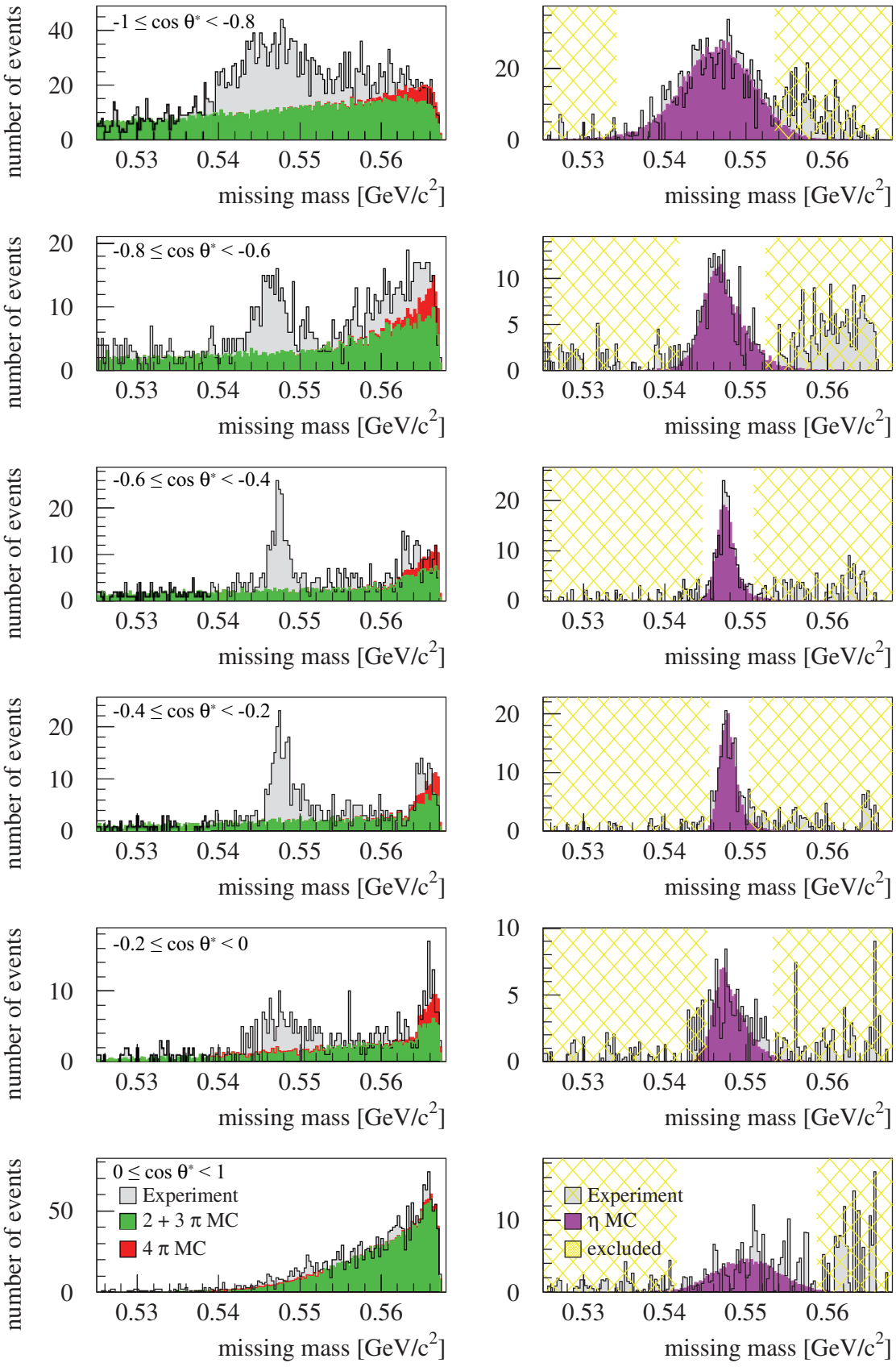

Figure 4.14 Same as Fig. 4.11, but at p_{beam} = 1.612 GeV/c (Q_η = 19.9 MeV).

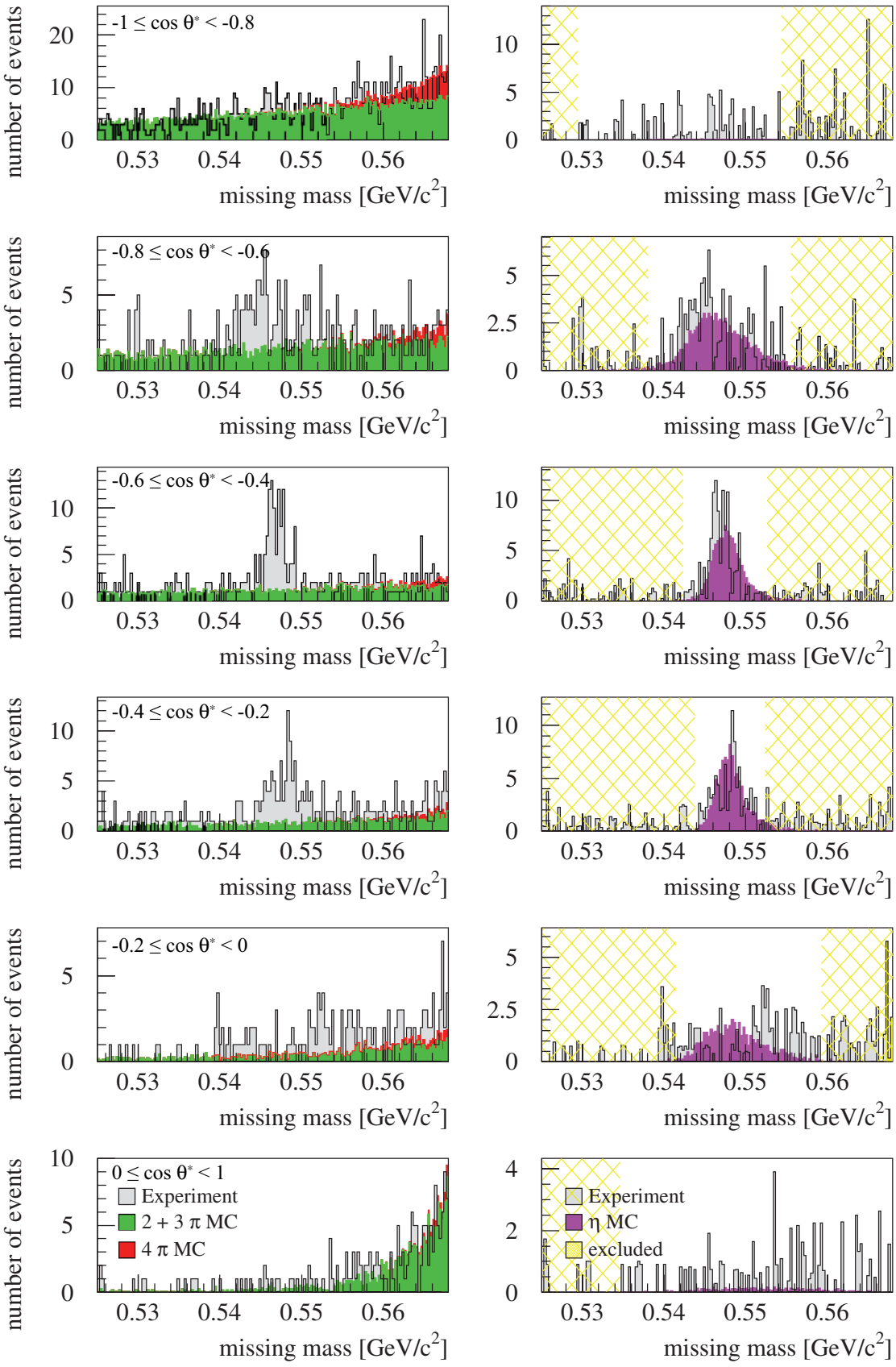

Figure 4.15 Same as Fig. 4.11, but at p_{beam} = 1.655 GeV/c (Q_η = 40.6 MeV).

4.2 Data Normalization

To calculate the total cross section $\sigma_{tot.}$, as given in Eq. 4.5, from the number of η events (N) in the missing mass spectrum, the acceptance of the detection system for a specific reaction ($\varepsilon_{reaction}$), the dead time (ε_{dead}), and the luminosity (L) times the time span of measurement τ have to be known:

$$\sigma_{tot.} = \left(\frac{N}{\varepsilon_{reaction}} \cdot \frac{1}{L \cdot \tau \cdot \varepsilon_{dead}} \right) \tag{4.5}$$

Assuming a complete beam-target overlap, the luminosity L itself is given by the number of stored particles in the accelerator (N_{beam}) over time and the areal target density(N_{target}/F):

$$L = \frac{dN_{beam}}{d\tau} \cdot \frac{N_{target}}{F} \tag{4.6}$$

Some of these values have in turn to be derived from other variables (Eq. 4.7, Eq. 4.8):

$$\frac{dN_{beam}}{dt} = \frac{I_{beam}}{e} = N_{beam} \cdot \nu \tag{4.7}$$

$$\frac{N_{target}}{F} = \rho_{target} \cdot \frac{N_A}{A} \cdot \frac{V}{F} \tag{4.8}$$

Here I_{beam} is the average beam current, e the elementary charge, ν the accelerators revolution frequency, ρ_{target} the target density, N_A the Avogadro constant, A the molecular weight of the target material and V the target volume.

The acceptance ($\varepsilon_{reaction}$) was determined by Monte Carlo studies. For the integrated luminosity however, since information concerning the beam-target overlap over time are only known with insufficient precision and N_{beam} and N_{target} vary over time as well, the integrated luminosity ($L \cdot \tau \cdot \varepsilon_{dead}$) of Eq. 4.5 for each of the the five measurements is deduced from the analysis of proton-deuteron elastic scattering:

$$L \cdot \tau \cdot \varepsilon_{dead} = \frac{N_{pd \to pd}(|t|)}{\varepsilon_{pd \to pd}} \Big/ \frac{1}{\frac{d\sigma_{pd \to pd}}{dt}(|t|) \cdot \Theta} \tag{4.9}$$

($N_{pd \to pd}(|t|)$) denotes the number of detected events of the reference reaction in a certain interval of momentum transfer (t), $(d\sigma_{pd \to pd}/dt)(|t|)$ the differential cross section for the reference reaction as function of the momentum transfer, $\varepsilon_{pd \to pd}$ the acceptance correction for each of the bins in the momentum transfer distribution and Θ the width of the t-bin:

$$\Theta = \left| \int_0^{t_{max}} dt \right| \tag{4.10}$$

The momentum transfer t in Eq. 4.10 is derived from the c.m.s. momentum p* and emission angle θ^* of the detected proton:

$$t = -2p^{*2} \cdot (1 - \cos\theta^*) \tag{4.11}$$

$$dt = 2p^{*2} d(\cos\theta^*) \tag{4.12}$$

$$\int dt = 2p^{*2} \int_0^{\pi} d(\cos\theta^*) = -4p^{*2} \tag{4.13}$$

4.2.1 Extraction of events of the pd → pd reaction

Fig. 4.16, presents events of the pd elastic scattering, visible as a narrow band (pd). Additionally, a broad distribution, which in part originates from the quasi-free proton-proton elastic scattering is visible (pp quasi-free). In the latter case, the neutron in the target deuteron acts only as a spectator to the scattering process. Both reactions can be used to determine the integrated luminosity and both inherit some aspects to be taken into account, when selecting one or the other as a reference reaction for luminosity determination. For the proton-deuteron elastic scattering there is only a limited set of data available, where in turn much data is available in the proton-proton case. As the proton-proton elastic scattering in proton-deuteron reaction, is only a quasi-free process, the fermi-motion between the two deuteron constituents leads to a broad distribution rather than a narrow band. Therefore, this channel can only be separated from background with limited precision. Furthermore, the fermi-motion has also to be considered in the description of this the quasi-free process [88], [89], [90]. Different to this the proton-deuteron elastic scattering shows up as a comparatively sharp and clean band of events in the spectra, that allows for a precise identification of this process. Therefore, this reaction was chosen for normalization purposes.

To extract the pd elastic events from the plots presented in Fig. 4.16, the plots were sliced into eight momentum transfer bins of $\Delta t = 0.1$ $(GeV/c)^2$ width in the range of -1.2 to -0.4 $(GeV/c)^2$.

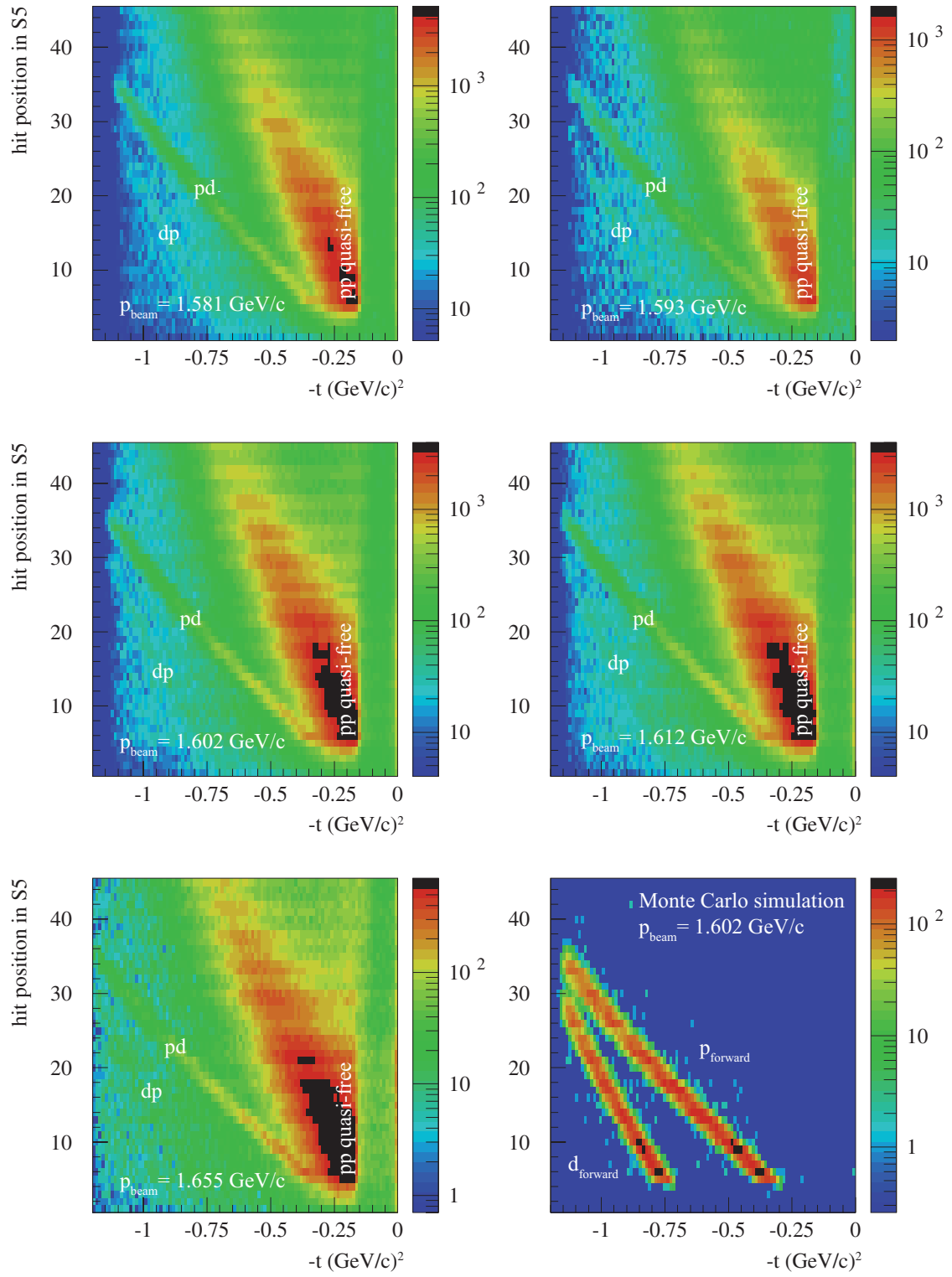

Figure 4.16 Proton-deuteron elastic scattering as correlation of the hit position in the monitor detector S5 versus the reconstructed momentum transfer. All but the lower right panel: Events recorded by means of the $T_{pd_{mon}}$ trigger. The fine lower band originates from proton-deuteron elastic scattering. Lower right: Monte Carlo simulation for the proton-deuteron elastic scattering at p_{beam}= 1.602 GeV/c. Due to deuteron breakup, the band of deuterons in the forward direction is only poorly visible in experiment, as compared to the simulation.

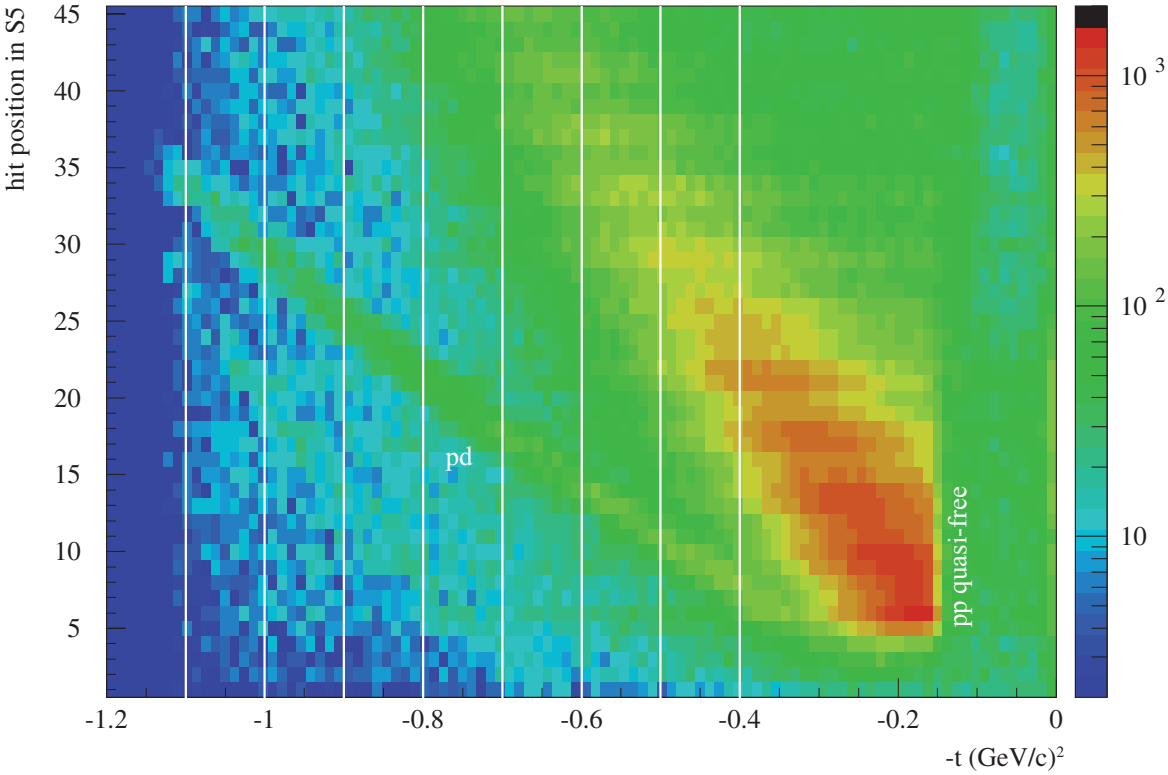

Figure 4.17 The momentum transfer spectrum of the pd-elastic scattering at p_{beam} = 1.593 GeV/c. The spectrum from each of the measured beam momenta is sliced into eight bins of equal width $|\Delta t| = 0.1$ (GeV/c)^2. Each slice is then projected on the ordinate, as shown in the example of Fig. 4.18, to extract the pd-elastic scattering events from the background by events of pp quasi-free scattering.

Fig. 4.18 shows as example the projection to the ordinate for p_{beam} = 1.593 GeV/c. In the bins of momentum transfers lower than $|-0.4\ (\mathrm{GeV/c})^2|$, the signal from the pd elastic scattering is hidden inside the pp-quasi-free scattering. Therefore, data below this momentum transfer was omitted.

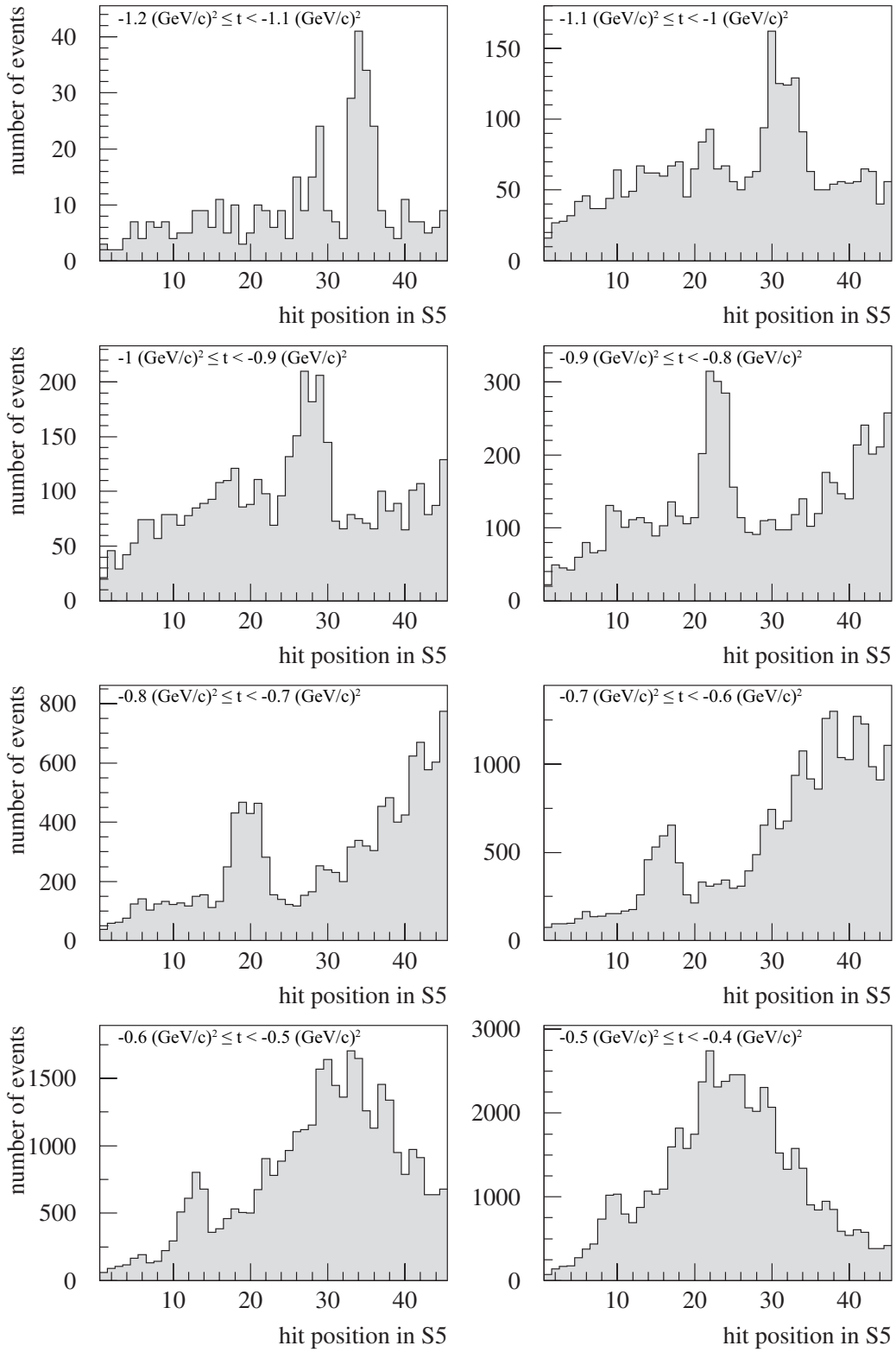

Figure 4.18 Hit distribution in the monitor detector at p_{beam} = 1.593 GeV/c. For reconstructed momentum transfers between -1.2 to -0.4 $(GeV/c)^2$ the data has been sliced into $|\Delta t|$ = 0.1 $(GeV/c)^2$ bins acording to Fig. 4.17. A clear signal of scattered deuterons is visible in every bin, mounted on top of a smooth background originating from the quasi-free pp scattering.

For each of the slices the background under the pd-signal can be described by a polynomial of no higher than third order, as indicated by the solid green and blue lines in Fig. 4.19, showing the p_{beam} = 1.602 GeV/c data. To determine the systematic uncertainty (Tab. 4.2, experimental results, $\sigma_{syst.}$) for the fitting procedure, a highest and lowest reasonable fit to the proton-proton background was set up. The arithmetic mean of both fits ($N_{pd}(\Delta t)$, Eq. 4.14) was used as a result for calculating the extracted number of events (Eq. 4.15, Tab. 4.2, experimental results, number of events), taking into account the prescaling factor of the trigger $T_{pd_{mon}}$ (Tab. 4.2, experimental results, prescaling factor).

$$N_{pd}(\Delta t) = \frac{(N(\Delta t) - N_{background,\,max.}(\Delta t)) + (N(\Delta t) - N_{background,\,min.}(\Delta t))}{2} \tag{4.14}$$

$$\text{number of events}(\Delta t) = N_{pd}(\Delta t) \cdot \text{prescaling factor} \tag{4.15}$$

The number of proton-proton background events was extracted in the same way (Eq. 4.16), it was used for calculating the statistical uncertainty of the extraction of the number of events in a peak arising from a background (Eq. 4.17, Tab. 4.2, experimental results, $\sigma_{stat.}$)[91].

$$n_{background}(\Delta t) = \frac{N_{background,\,max.}(\Delta t) + N_{background,\,min.}(\Delta t)}{2} \cdot \text{prescaling factor} \tag{4.16}$$

$$\sigma_{stat.} = \sqrt{\text{number of events}(\Delta t) + 2 \cdot n_{background}(\Delta t)} \tag{4.17}$$

Additionally to fitting the background, the pd-peak was limited to the region marked by the dashed red lines in Fig. 4.19 for determination of the peak and background content. The results, presented as grey shaded peaks in Fig. 4.20, for the p_{beam} = 1.593 GeV/c data, have been compared to Monte-Carlo simulations (Fig. 4.20, green shaded peaks), revealing a good agreement of the position of the pd-peak in each of the momentum transfer intervalls. The same holds true for the respective situations at the other beam momenta.

The results of the described extraction are presented in Tab. 4.2 with the respective uncertainties, both systematical and statistical, as described above for the experimental results. For the Monte Carlo simulation, the statistical uncertainty was only limited by the number of generated events as derived in Eq. 4.18 [91].

$$\sigma_{stat.} = \sqrt{\text{number of events}} \tag{4.18}$$

For this analysis a sample of four million events for each beam momentum has been generated and analyzed.

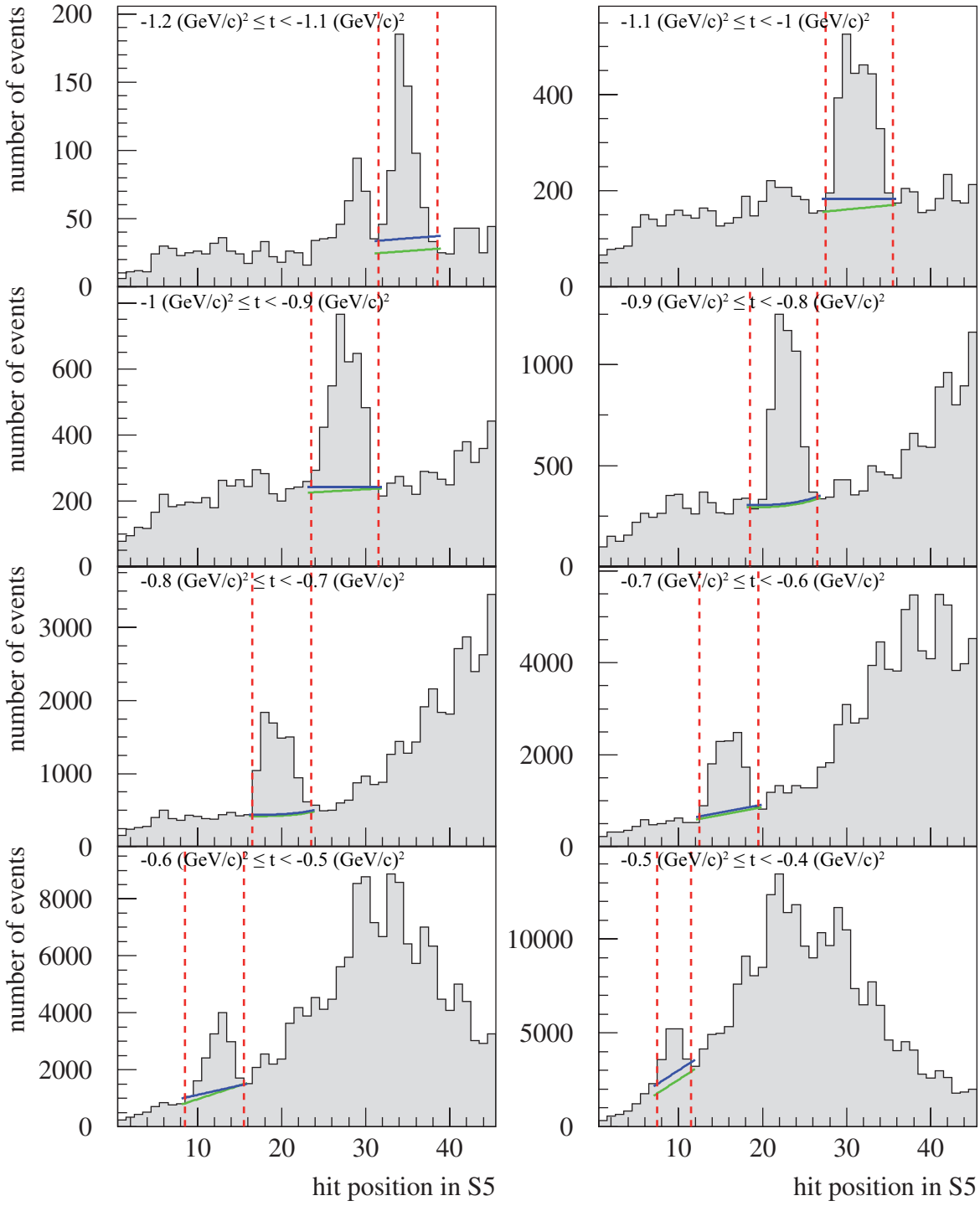

Figure 4.19 Subtraction of the proton-proton (quasi-free) background at p_{beam}= 1.602 GeV/c. For reconstructed momentum transfers between -1.2 and -0.4 $(GeV/c)^2$ the data has been sliced into $|\Delta t|$= 0.1 $(GeV/c)^2$ intervalls acording to Fig. 4.17. The solid green (blue) line represents the lowest (highest) accepted fit to the pp-quasi-free background, the dashed red lines indicate the cuts used to isolate the silicon pads of the detector containing the pd-peak.

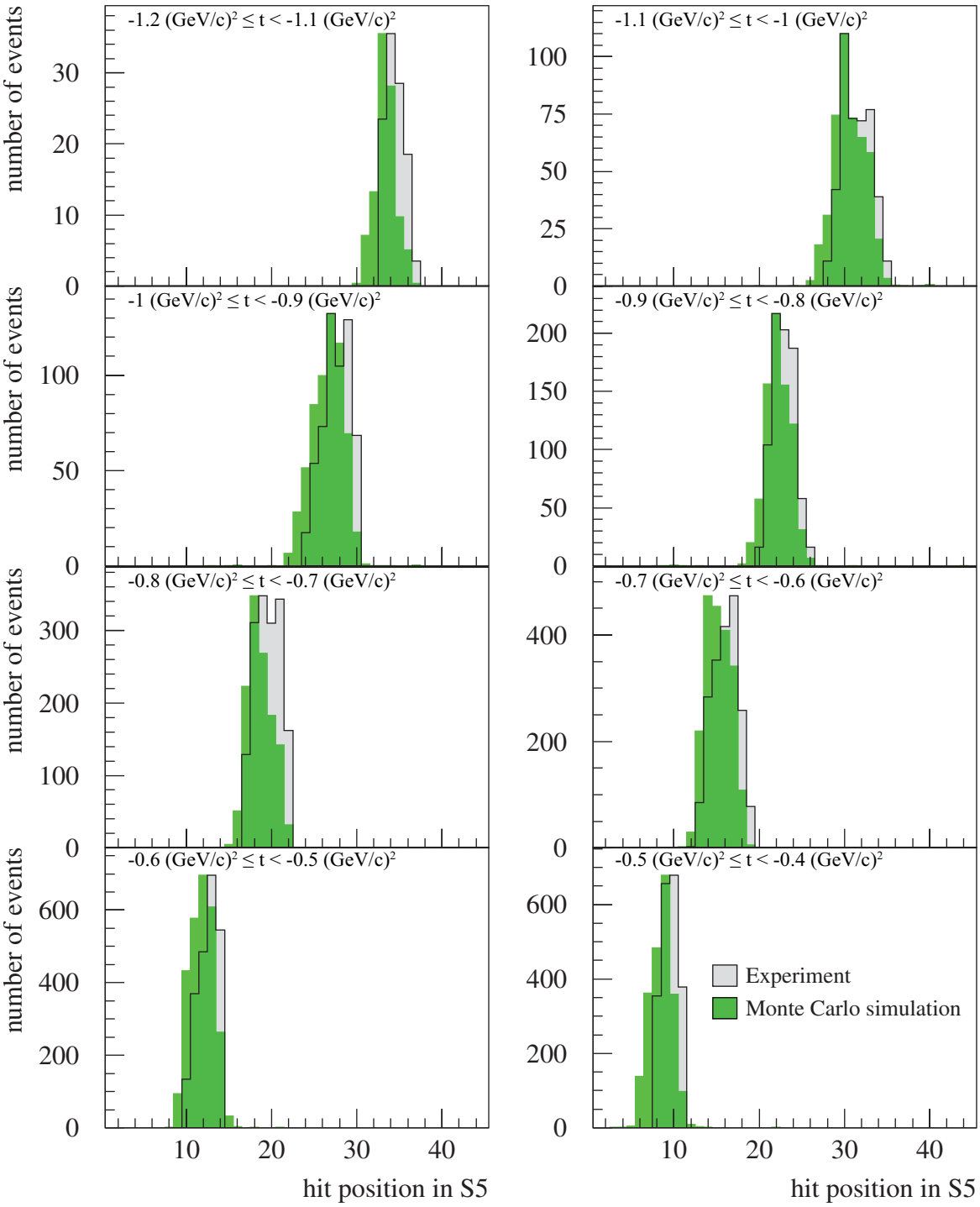

Figure 4.20 Background subtracted pd → pd peaks in the Δt-bins at p_{beam} = 1.593 GeV/c. The position of the experimental signal from the pd → pd reaction (grey shaded curve) is in reasonable agreement with the expectation from Monte Carlo simulations (green shaded curve). The observed shift by one bin might be attributed to the alignment of the detector S5 and is of no relevance, since only information of the protons in the drift chambers is utilized for the analyzing process.

p_{beam}	Δt region	experimental results				Monte Carlo simulation	
[GeV/c]	[(GeV/c)^2]	prescaling factor	number of events	$\sigma_{stat.}$ [%]	$\sigma_{syst.}$ [%]	number of events	$\sigma_{stat.}$ [%]
1.581	$-1.2 \le t < -1.1$	2^3	1220	3.3	0.3	371	5.2
	$-1.1 \le t < -1$	2^3	10784	1.5	2.7	3024	1.8
	$-1 \le t < -0.9$	2^3	13960	1.6	3	2654	1.9
	$-0.9 \le t < -0.8$	2^3	22644	1	3.1	3151	1.8
	$-0.8 \le t < -0.7$	2^3	41344	0.7	1.9	3875	1.6
	$-0.7 \le t < -0.6$	2^3	50520	0.7	5.6	4131	1.6
	$-0.6 \le t < -0.5$	2^3	64960	0.6	2.9	4114	1.6
	$-0.5 \le t < -0.4$	2^3	62348	0.7	14.4	4270	1.5
1.593	$-1.2 \le t < -1.1$	2^5	3360	2.2	4.8	727	3.7
	$-1.1 \le t < -1$	2^5	13984	1.4	0.5	3062	1.8
	$-1 \le t < -0.9$	2^5	19280	1.2	0.6	2532	2
	$-0.9 \le t < -0.8$	2^5	24736	1.1	3.6	3245	1.8
	$-0.8 \le t < -0.7$	2^5	50592	0.6	1.4	3857	1.6
	$-0.7 \le t < -0.6$	2^5	68576	0.6	1.9	4097	1.6
	$-0.6 \le t < -0.5$	2^5	79552	0.5	7	4068	1.6
	$-0.5 \le t < -0.4$	2^5	78304	0.6	2.6	4205	1.5
1.602	$-1.2 \le t < -1.1$	2^3	3456	2.4	7.2	1090	3
	$-1.1 \le t < -1$	2^3	12496	1.5	2.9	3029	1.8
	$-1 \le t < -0.9$	2^3	17008	1.3	1.6	2484	2
	$-0.9 \le t < -0.8$	2^3	27504	0.9	1.2	3259	1.8
	$-0.8 \le t < -0.7$	2^3	48856	0.6	1.1	3882	1.6
	$-0.7 \le t < -0.6$	2^3	65780	0.6	2.2	4051	1.6
	$-0.6 \le t < -0.5$	2^3	75500	0.6	5	4049	1.6
	$-0.5 \le t < -0.4$	2^3	82384	0.5	9.7	4144	1.6

Table 4.2 Results of the background subtracted peaks of the pd → pd elastic scattering. The number of events for the experimental results takes into account the prescaling factor used in experiment, as denoted in the respective column. For the Monte Carlo analysis, a sample of four million simulated events was used at each of the five beam momenta.

p_{beam}	Δt region	experimental results				Monte Carlo simulation	
[GeV/c]	[(GeV/c)^2]	prescaling factor	number of events	$\sigma_{stat.}$ [%]	$\sigma_{syst.}$ [%]	number of events	$\sigma_{stat.}$ [%]
1.612	$-1.2 \le t < -1.1$	2^3	5040	2	1.1	1421	2.7
	$-1.1 \le t < -1$	2^3	13960	1.4	2	2953	1.8
	$-1 \le t < -0.9$	2^3	16360	1.4	2.2	2427	2
	$-0.9 \le t < -0.8$	2^3	21544	0.8	0.8	3340	1.7
	$-0.8 \le t < -0.7$	2^3	51360	0.6	2.8	3849	1.6
	$-0.7 \le t < -0.6$	2^3	69560	0.5	1	3970	1.6
	$-0.6 \le t < -0.5$	2^3	89840	0.5	5.3	3962	1.6
	$-0.5 \le t < -0.4$	2^3	81592	0.5	5	4187	1.5
1.655	$-1.2 \le t < -1.1$	2^5	11600	1.6	7	2699	1.9
	$-1.1 \le t < -1$	2^5	13104	1.6	2.8	2850	1.9
	$-1 \le t < -0.9$	2^5	15648	1.5	4.5	2428	2
	$-0.9 \le t < -0.8$	2^5	33904	0.8	1.7	3434	1.7
	$-0.8 \le t < -0.7$	2^5	48288	0.7	2.2	3741	1.6
	$-0.7 \le t < -0.6$	2^5	67488	0.6	0.9	3806	1.6
	$-0.6 \le t < -0.5$	2^5	79680	0.5	3.1	3903	1.6
	$-0.5 \le t < -0.4$	2^5	89280	0.5	3.3	4019	1.6

Table 4.2 Results of the background subtracted peaks of the pd → pd elastic scattering. The number of events for the experimental results takes into account the prescaling factor used in experiment, as denoted in the respective column. For the Monte Carlo analysis, a sample of four million simulated events was used at each of the five beam momenta.

With this information available, it is possible to derive relative differential cross sections ($d\sigma/dt$, Eq. 4.19) for the proton-deuteron elastic scattering (Fig. 4.21), by applying an acceptance correction based on Monte Carlo simulations.

$$\frac{d\sigma}{dt}(\Delta t) = \text{num. of events}_{\text{exp. results}}(\Delta t) \cdot \frac{\text{num. of events}_{\text{Monte Carlo simulation}}(\Delta t)}{\text{num. of Monte Carlo events generated}} \qquad (4.19)$$

However, the absolute scale of this measured differential cross sections is arbitrary and has to be determined by comparing these cross sections to reference data from literature, as described in the next section. The horizontal error bars in Fig. 4.21 represent the chosen Δt-bin in the

analysis, rather than matching the uncertainty in the determination of the momentum transfer in $(GeV/c)^2$.

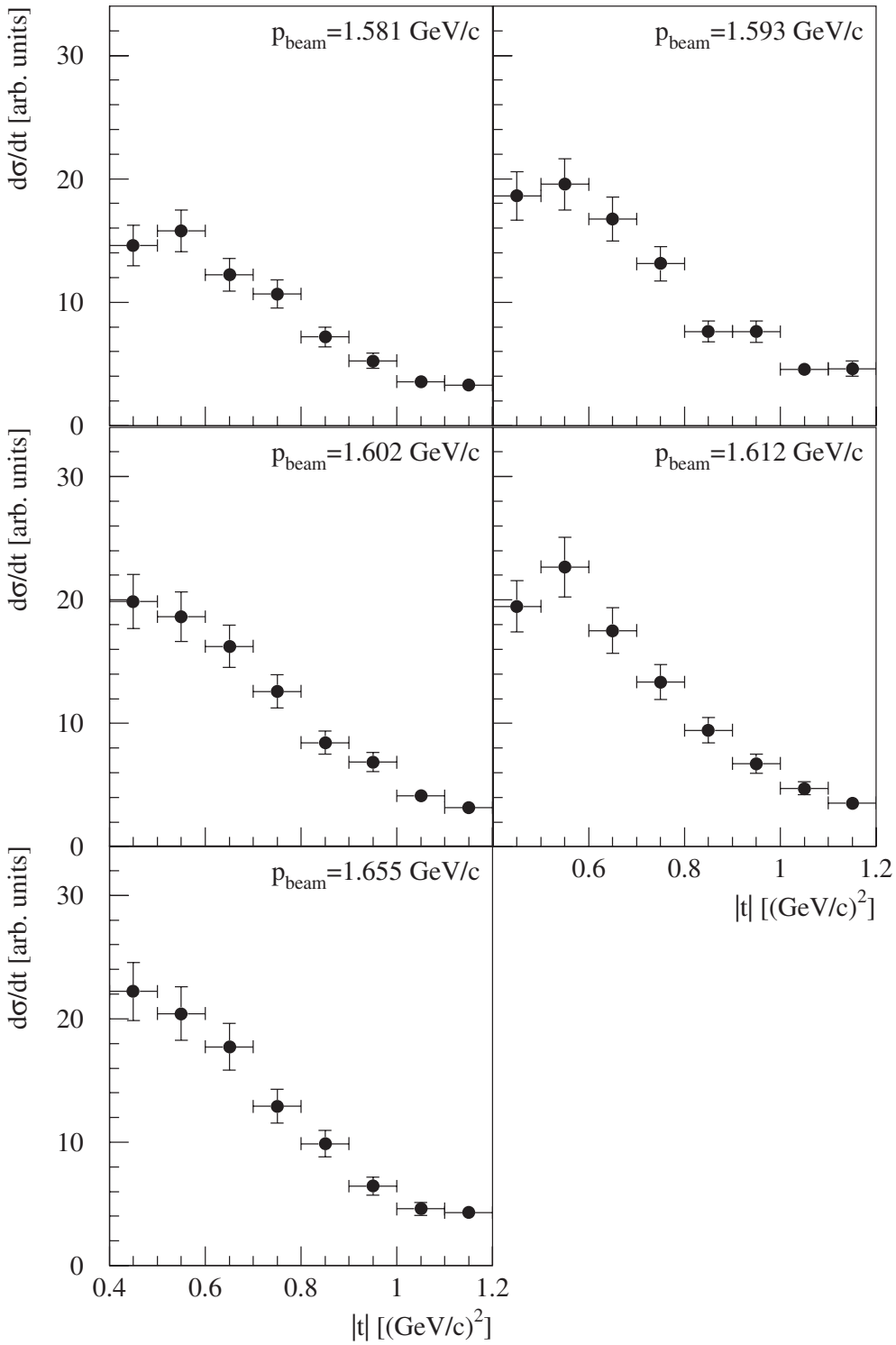

Figure 4.21 Relative differential cross section dσ/dt for the pd elastic scattering obtained at COSY-11 (p_{beam} = 1.581 GeV/c up to p_{beam} = 1.655 GeV/c). Obviously, the shape of the differential cross sections in the range of the observed momentum transfers is similar at least over the range of beam momenta measured.

4.2.2 Determination of the pd → pd cross section

Compared to the pp elastic scattering in the vicinity of the investigated proton beam momenta and relevant momentum transfers for the pd elastics scattering there is no such wealth of data available. Therefore, the differential cross sections needed for normalization have to be derived by the interpolation of energetically close data.

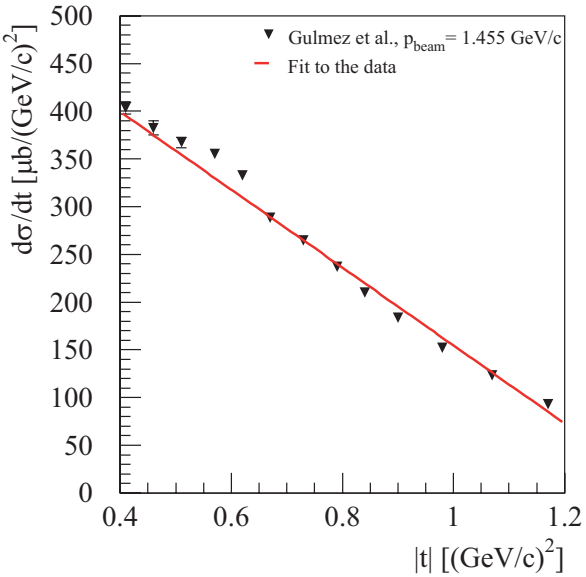

Figure 4.22 Fit to the differential pd → pd cross sections dσ/dt (|t|). The momentum transfer dependence of the differential pd → pd cross section dσ/dt (|t|) is described well by a first order polynomial fit (solid red line). Presented are data taken from [92], measured bei Gülmez et al. at a beam momentum of p_{beam} = 1.455 GeV/c. This data set was chosen as a reference, because a second data set measured at a ~ 180 MeV/c lower beam momentum is available from the same experiment. This allows to directly check the quality of the approximation, described in the text, to interpolate the beam momentum dependency of the differential cross section in the momentum transfer spectrum.

As shown in Fig. 4.22 at a beam momentum of p_{beam} = 1.455 GeV/c the pd elastic scattering is described well in the momentum transfer region of interest by a first order polynomial fit:

$$\frac{d\sigma}{dt}(|t|, p = 1.455\,\mathrm{GeV/c}) = h(|t|) = a + b \cdot |t| \tag{4.20}$$

For a and b values of a = 563 ± 6 μb/(GeV/c)^2 and b = 408 ± 7 μb/(GeV/c)^4 have been determined. The function h(|t|) can now be used to describe other differential cross section data in the same region of momentum transfers, obtained at different beam momenta p_i. For this purpose the function h(|t|) was scaled by a beam momentum correction factor $\alpha_i(p_i)$:

$$\frac{d\sigma}{dt}(|t|, p_i) = \alpha_i(p_i) \cdot h(|t|) \tag{4.21}$$

In Fig. 4.23 the result of the momentum transfer fit (Eq. 4.20) for p_{beam} = 1.455 GeV/c is shown as a solid red line together with the scaled beam momentum fits (Eq. 4.21, dashed green lines) for three other data sets.

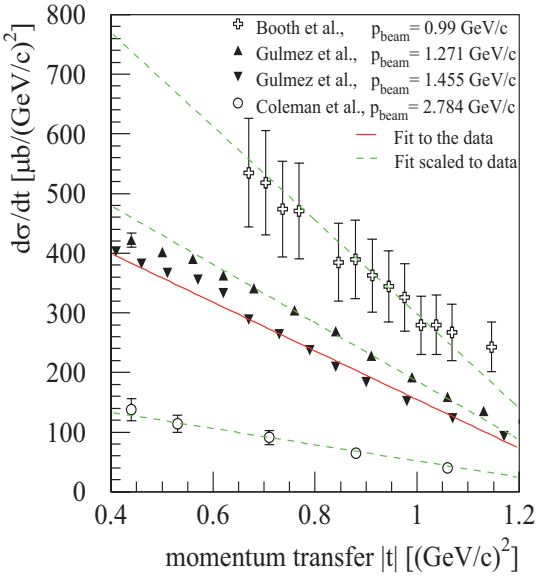

Figure 4.23 Beam momentum correction for the momentum transfer dependence of the differential pd $\rightarrow$ pd cross section $d\sigma/dt$ ($|t|$). The momentum transfer function fits very well, when scaled by a factor $\alpha_i(p_i)$, to high and low beam momentum data available from literature [93], [92], [94]. Presented are fits to the second data set from [92] at 1.271 GeV/c and data sets from different experiments at the highest (2.784 GeV/c, [94]) and lowest (0.99 GeV/c, [93]) beam momenta available.

Obviously, this method is able to describe different cross sections for beam momenta between p_{beam} = 0.99 GeV/c and p_{beam} = 2.784 GeV/c. The correction factors $\alpha_i(p_i)$ derived using Eq. 4.21 are presented in Fig. 4.24 as function of the beam momentum p. The momentum dependency can be described by an exponential function of type

$$A(p) = \exp(\lambda + \beta \cdot p + \gamma \cdot p^2) \tag{4.22}$$

(solid red line) with independent parameters λ, β and γ. These parameters have been determined to: $\lambda = 2.40 \pm 0.04$, $\beta = (2.2 \pm 0.1)$ $(GeV/c)^{-1}$ and $\gamma = (0.32 \pm 0.07)$ $(GeV/c)^2$.

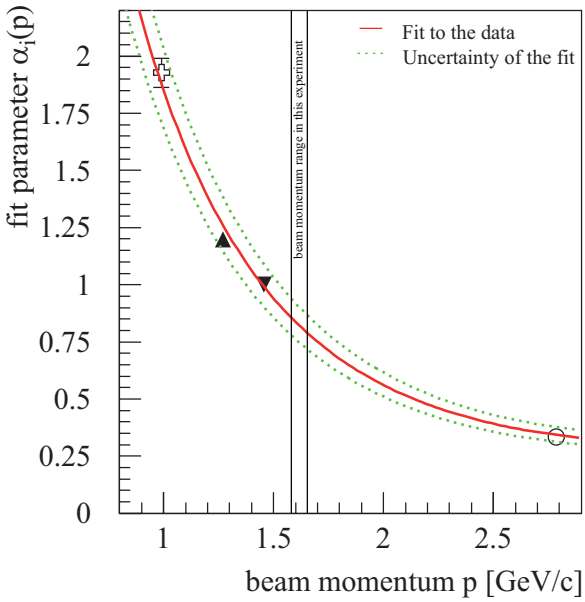

Figure 4.24 Beam momentum dependence of the differential cross sections. The parameters $\alpha_i(p_i)$ can be described by an exponentional function (solid red line); the dotted green curves indicate the uncertainties of the fitting procedure, accounted for in the overal systematic uncertainty of the luminosity determination.

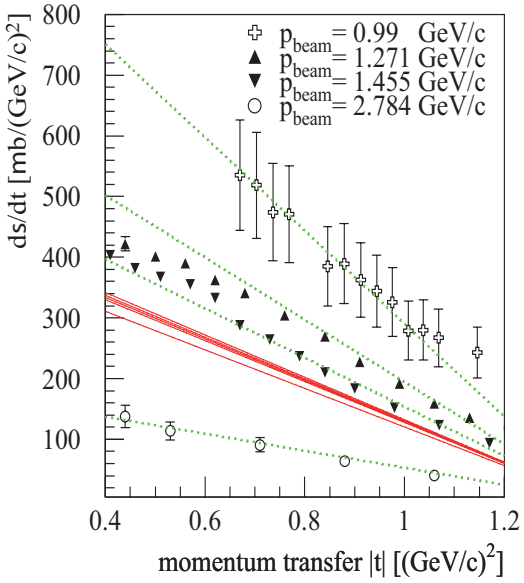

Figure 4.25 Beam momentum interpolation for the differential cross sections. The description of the differential cross sections (dashed green lines) is in good agreement with the data taken from [92], [94], [95] (lowest to highest beam momentum). The interpolated differential cross sections for the five beam momenta of this experiment are indicated by solid red lines.

This results in a description of the interpolated differential cross section of:

$$\frac{d\sigma}{dt}(|t|, p) = A(p) \cdot h(|t|) = \tag{4.23}$$

$$\exp\left[(2.4 \pm 0.04) - \left(2.2 \pm 0.1 \frac{1}{\mathrm{GeV/c}}\right) \cdot p + \left(0.32 \pm 0.07 \frac{1}{(\mathrm{GeV/c})^2}\right) \cdot p^2\right] \cdot$$

$$\left[(563 \pm 6) \frac{\mu b}{(\mathrm{GeV/c})^2} - (408 \pm 7) \frac{\mu b}{(\mathrm{GeV/c})^4} \cdot |t|\right]$$

The function $d\sigma/dt\,(|t|,p)$ describes data from literature within the experimental uncertainties (Fig. 4.25 dashed green lines) and therefore allows to interpolate the differential cross sections for the integrated luminosity determination at the studied beam momenta in this experiment (Fig. 4.25, solid red lines). The results are listed in Tab. 4.3.

beam momentum [GeV/c]	**integrated luminosity [1/nb]**	$\sigma_{stat.}$	$\sigma_{syst.}$
1.581	53.5	± 0.8%	± 8.9 %
1.593	67.8	± 0.7 %	± 8.9 %
1.602	64.8	± 0.7 %	± 8.9 %
1.612	70.2	± 0.7 %	± 8.9 %
1.655	72.2	± 0.7 %	± 8.9 %

Table 4.3 Integrated luminosity determined from the proton-deuteron elastic scattering. The systematic uncertainty is dominated by the exponential fit to the beam momentum dependency.

As the differential cross section at each measured beam momentum was determined separately for each Δt-bin, and the interpolation technique also describes not only the beam momentum dependency, but also the momentum transfer dependency in each beam momentum, eight independent measurements of the integrated luminosity exist. To extract the integrated luminosity with high accuracy, as presented in Tab. 4.3, the best estimates [91] have been calculated from the eight measurements at each beam momentum:

Given a sample of measured values x_i with uncertainties $\pm\sigma_i$, its best estimate $\bar{x}$ and the corresponding uncertainty $\pm\bar{\sigma}$ are determined by Eq. 4.24 and Eq. 4.25, respectively.

$$\bar{x} = \left(\sum_i \frac{x_i}{\sigma_i^2}\right) \Big/ \left(\sum_i \frac{1}{\sigma_i^2}\right) \tag{4.24}$$

$$\bar{\sigma} = \sqrt{\frac{1}{\sum_i 1/\sigma_i^2}} \tag{4.25}$$

5 Results

5.1 Differential cross section and angular distributions

Based on the missing mass analysis, pd → ^{3}He η differential cross sections have been extracted for all measured excess energies, with the results displayed in Fig. 5.1.

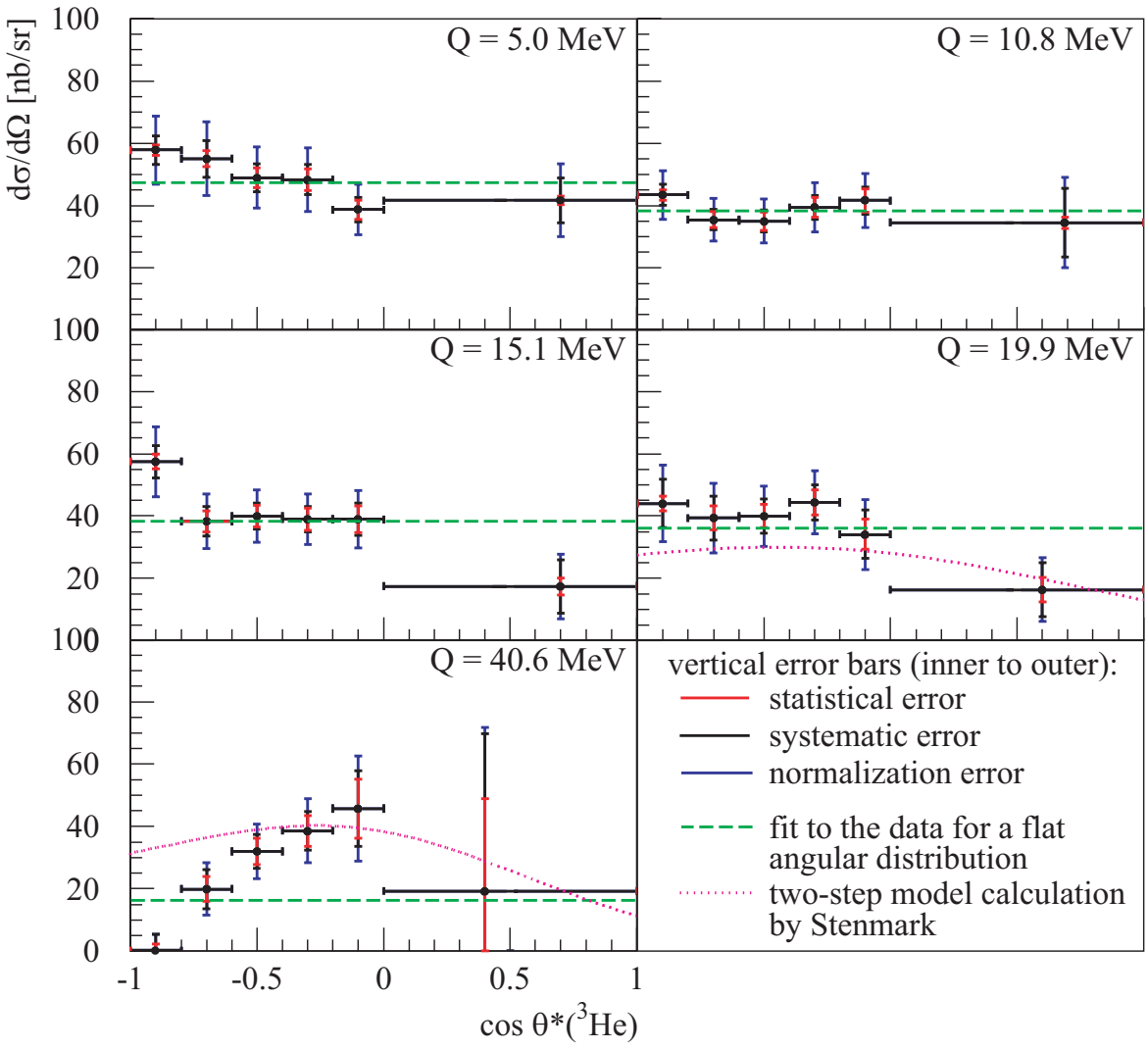

Figure 5.1 Differential cross sections determined at five different excess energies. The angular distributions of the produced ^{3}He-nuclei in the center of mass system show a transition from a rather flat shape (Q = 5.0, 10.8 MeV) to a highly anisotropic distribution (Q = 40.6 MeV), as compared to phase space (dashed green line). The uneven width of the bins chosen for the analysis is due to the limited statistics of the experiment and does not reveal any deficiency in the detection system. For a description of the dotted lines, see text.

The bin width in the backward hemisphere was limited by the accuracy of the center-of-mass angle reconstruction. In the forward hemisphere, the statistics allowed only for one bin. However, the SPES data resulted in angular distributions compatible with pure s-wave emission, and also the WASA/PROMICE studies presented slowly varying angular distributions for the lower excess energies. Hence, we concentrated on taking data at several excess energies, with limited statistics, rather than aiming at the extraction of high statistics angular distributions. Nevertheless, the angular distributions obtained are sufficient to extract total cross sections.

Over the range of excess energies investigated a transition is seen from a rather flat angular distribution at the two lowest energies, as observed in [2], to a highly anisotropic behavior for the highest measured excess energy of 40.6 MeV, as in [14], [19]. Therefore, it is plausible to assume a dominance of s-wave production from threshold up to excess energies in the range between 11 and 15 MeV. This behavior differs from that of the pd $\rightarrow$ ^{3}He π^0 reaction, where already very close to threshold significant contributions of higher partial waves have been reported [1]. Besides showing the deviation from s-wave production for the Q = 19.9 and 40.6 MeV measurements, Fig. 5.1 presents also the prediction of two-step model calculations from Stenmark [96].

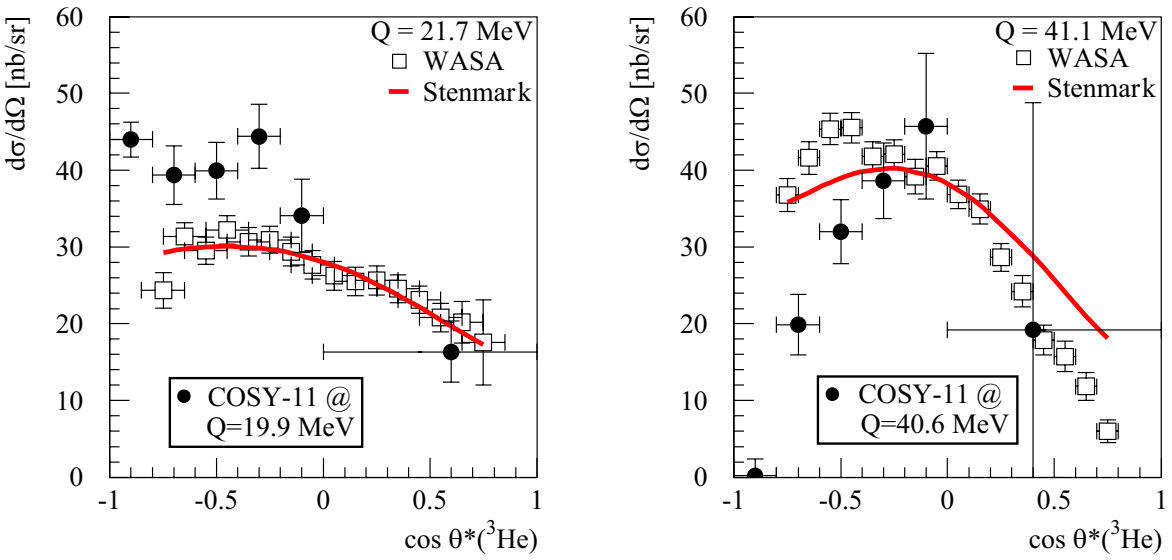

Figure 5.2 Acceptance-corrected differential cross sections in cos θ^*(^{3}He) at the two lowest beam energies of [19]. Dashed line is the calculation by Stenmark, based on a two-step model [96]. Solid circles are the present COSY-11 measurements at nearby, but slightly lower excess energies, as denoted in the legend.

The latter were performed to describe the WASA/PROMICE data [19] (Fig. 5.2), while the predictions in Fig. 5.1 were calculated at the corresponding COSY-11 excess energies [97].

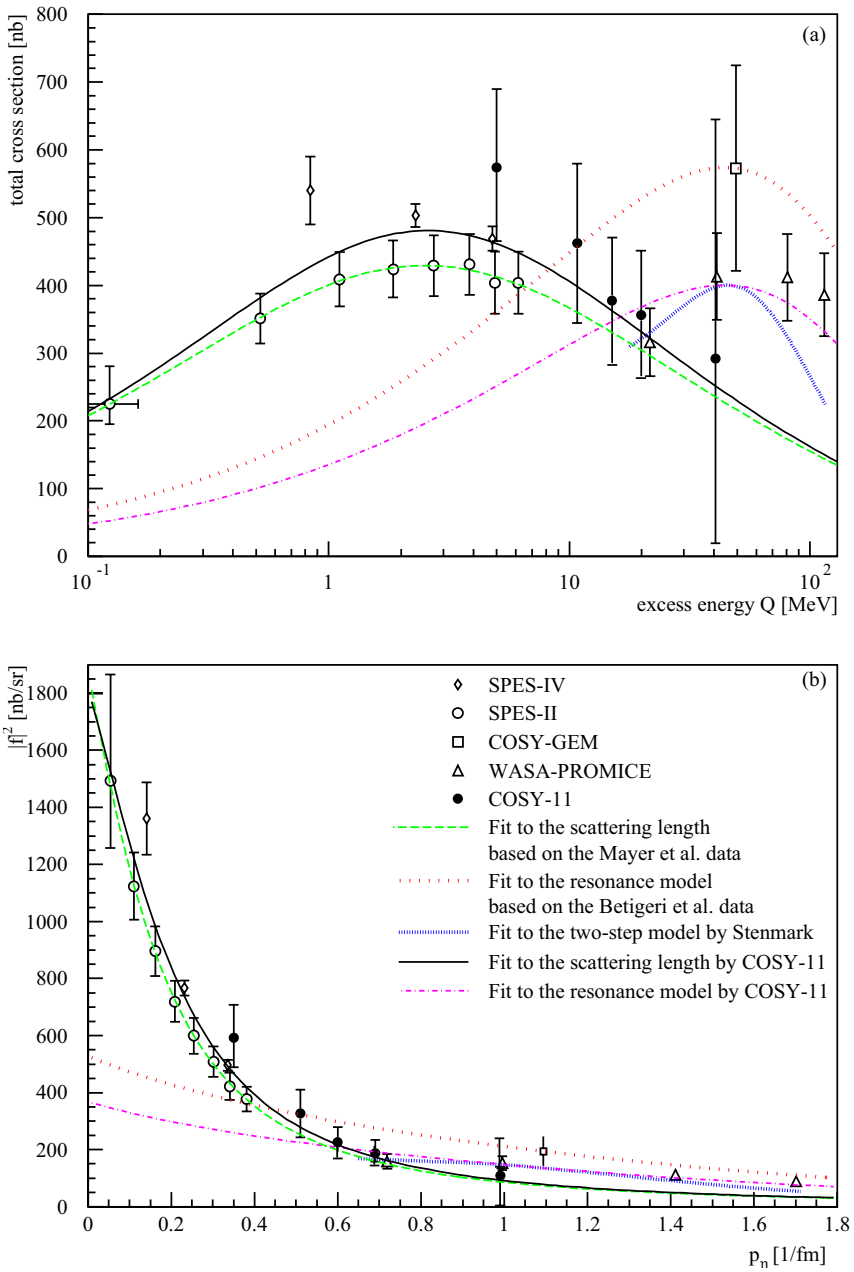

Figure 5.3 Excitation function of the pd → ^{3}He η production. Upper: Total cross section as function of the excess energy Q. Lower: Squared production amplitude as function of the η-momentum. The uncertainty in the η-momentum/excess energy is in the order of the symbol size [98]. The lines present fits to the data based on the two proposed reaction models: The fit to the Mayer et al. data was taken from [2], the fit to the Betigeri et al. data was taken from [14] and the fit to the two-step model by Stenmark was taken from [96].

The result is in reasonable agreement with the COSY-11 data at Q = 19.9 MeV. However, at Q = 40.6 MeV, the shape of the angular distribution in the backward hemisphere does not agree as well. Such a deviation shows up also at the WASA/PROMICE measurements at Q = 41.1 MeV (Fig. 5.2, r.h.s). Furthermore, the results from COSY-11 at excess energies of

Q = 19.9 MeV and Q = 40.6 MeV show a behavior of the differential cross section similar to that of the WASA/PROMICE data.However, the data sets differ significantly in the backward hemisphere (Fig. 5.2). To clarify this situation, precision data on this topic would be desirable.

5.2 Total cross sections and production amplitudes

Utilizing the determination of the integrated luminosity via pd elastic scattering the total cross section was extracted for each of the measured excess energies, and shown in Fig. 5.3 and Tab. 5.1. The normalization uncertainty $\sigma_{norm.}$ is principally due to the luminosity determination from the pd $\rightarrow$ pd reaction. The systematic error from the extraction of the η signal from background is only of minor relevance in this respect and only becomes significant at Q=40.6 MeV, where the statistics are low. The error bars presented, e.g. in Fig. 5.3, represent the total error as a sum of the systematic, statistical, and normalization error given in Tab. 5.1.

p_{beam}	Q	E_{kin}	p_η^*	production amplitude $\|f\|^2$				total cross section $\sigma_{tot.}$			
[GeV/c]	[MeV]	[MeV]	[1/nb]	[nb/sr]	$\sigma_{stat.}$	$\sigma_{syst.}$	$\sigma_{norm.}$	[nb]	$\sigma_{stat.}$	$\sigma_{syst.}$	$\sigma_{norm.}$
1.581	5.0	900	0.35	592	± 12	± 38	± 64	574	± 12	± 8	± 62
1.593	10.8	911	0.51	327	± 10	± 41	± 34	462	± 14	± 9	± 47
1.602	15.1	918	0.6	227	± 12	± 22	± 24	378	± 20	± 7	± 40
1.612	19.9	927	0.69	187	± 14	± 16	± 19	356	± 27	± 9	± 37
1.655	40.6	964	0.99	109	+ 71 − 45	+ 49 − 45	± 11	292	+ 191 − 121	+ 132 − 121	± 30

Table 5.1 Extracted values for the production amplitude squared and the total cross section for the pd $\rightarrow$ ^{3}He η reaction. The uncertainty in the beam momentum p_{beam} is in the order of 1 ‰.

Eliminating the phase space factor from the data, the mean of the absolute square of the production amplitudes $|f|^2$ is obtained from the differential cross section $d\sigma/d\Omega$ data using

$$|f|^2 = \frac{p_p^*}{p_\eta^*} \cdot \frac{d\sigma}{d\Omega} \tag{5.1}$$

where p_p^* and p_η^* are the momenta of the initial proton and final state η meson in the c.m.s., respectively. This allow an alternative presentation of the data which stresses the underlying special features of the reaction process (Fig. 5.3 (b), Tab. 5.1). These new values of the production amplitudes close the open gap between the SPES data [1], [2] at low energies and the higher energy data from WASA/PROMICE [19] and COSY-GEM [14] (Fig. 5.3), confirming the strong decrease of the production amplitude from threshold with increasing excess energies. Furthermore, the excitation function was found to decrease monotonically over the range of

5 to 40.6 MeV excess energy and does not exhibit any enhancement at higher Q-values, as quoted in [19]. Therefore all predictions of model calculations, who rely on an enhancement in this region of excess energies can be ruled out. A closer look at the different reaction models in view of this new data points is presented in the next section.

5.3 Reaction model fits

Fits to the data based on the two proposed reaction models to describe the energy dependence are presented in Fig. 5.3, as well as data points available in the close to threshold region up to Q = 120 MeV.

5.3.1 Resonance model

The dotted line with wide gaps represents a Breit-Wigner fit to a purely resonant production mechanism, as proposed by Betigeri et al. [14]. The total cross section as function of the η excitation energy E is derived (Eq. 5.2) by a matrix element M(E) for the Breit-Wigner approximation (Eq. 5.3), which was applied in calculations for photoproduction of neutral mesons [99]:

$$\sigma(E) = \frac{p^*_\eta}{p^*_p} \cdot |M(E)|^2 \tag{5.2}$$

In the Breit-Wigner description of [14] the values of the mass and width of the resonance N*(1535) where fixed to $m_R = 1540$ MeV/c^2 and $\Gamma_R = 200$ MeV, similar as it was done in [99], keeping only the strength A as a free parameter.

$$|M(E)|^2 = \frac{A \cdot \Gamma_R^{\,2}}{(E - m_R)^2 + \Gamma(E)^2} \tag{5.3}$$

$$\Gamma(E) = \Gamma_R \cdot \left(b_\eta \cdot \frac{p^*_\eta}{p^*_{\eta,R}} + b_\pi \cdot \frac{p^*_\pi}{p^*_{\pi,R}} + b_{\pi\pi} \right) \tag{5.4}$$

The values of the branching ratios $b_\eta = 0.46$, $b_\pi = 0.49$ and $b_{\pi\pi} = 0.05$ of the resonance decay channels are averages taken from [101] and the p_i^* are the momenta of the respective particles in the center of mass system [14]. Each value with a lower index R stands for the respective value at the position of the center of the resonance.

In [14] the strength A was scaled to fit one single data point obtained in [14]. This approach was supposed to describe data at higher excess energies and obviously fails completely to describe the excitation function close to threshold (Fig. 5.3).

Scaling the Breit-Wigner fit for an optimized description of all data, including the present COSY-11 measurements above 15 MeV excess energy, yields the dash-dotted line of Fig. 5.3. Especially in the total cross section plot of Fig. 5.3, it is obvious that this approach is able to describe the high-energy data, but fails completely to reproduce the shape of the excitation function below Q = 20 MeV. Furthermore, the angular distributions presented here, as well as in [14] and [19], show that at excess energies above 10-20 MeV one can not assume pure s-wave scattering and, therefore the predominant contribution of an S_{11}-resonance is highly unlikely.

5.3.2 Two-step model + FSI

The dashed line corresponds to the application of an $\eta-{}^3$He FSI ansatz (Eq. 5.5) to the data from SATURNE [2], as proposed by Wilkin [10], to refine the energy dependence of the two-step model of Kilian and Nann:

$$|f|^2 = \left|\frac{f_B}{1 - i \cdot p^*_\eta \cdot a}\right|^2 = \frac{f_B^2}{1 + 2 \cdot p^*_\eta \cdot \Im(a) + p^{*2}_\eta \cdot \Im(a)^2 + p^{*2}_\eta \cdot \Re(a)^2} \tag{5.5}$$

As well as neglecting the effective range contribution, the implicit assumption here is that f_B varies only slowly with energy.

Although this approach is only valid in the near-threshold region, for demonstration purposes the curve has been extended up to higher excess energies. In addition to the data from [2], this curve also describes our highest energy data points within the error bars and the lowest energy WASA/PROMICE data point, but fails to describe any of the data from WASA/PROMICE and COSY-GEM at higher excess energies. However, as already pointed out in [102], the χ^2/n_{df} of such a fit to the results of [2] alone is inconsistent with the quoted statistical uncertainty of the data.

A different calculation by Stenmark [96], also exploiting a two-step model approach, is included in Fig. 5.3 as a dotted line with narrow gaps. This prediction is only valid for higher excess energy data (Q > 18 MeV), where higher partial waves contribute to the reaction process. According to [96], when including FSI effects and assuming that the FSI affects p and d waves by the same amount as it affects s waves, this model is able to roughly reproduce the energy dependence of the WASA/PROMICE data but overestimates the differential cross section.

5.4 $\eta-{}^3$He scattering length

With the additional data from COSY-11, a fit based on the $\eta-{}^3$He-scattering length approach has been performed (Fig. 5.3, solid line). In this fit only the present results up to an excess

energy of 10.8 MeV (p_η = 0.51 fm^{-1}) and the data from [1], [2] have been included, as the FSI-calculation from [6] is only valid for pure s-waves and the angular distributions of data above Q = 10.8 MeV reveal contributions of higher partial waves, as is obvious in Fig. 5.1. Based on this data selection, the scattering length a was determined to be $|\Re(a)|$ = 4.2 ± 0.5 fm, $\Im(a)$ = 0.4 ± 1.9 fm and f_B = 39.6 ± 7.6 nb/sr (Fig. 5.3, solid line).

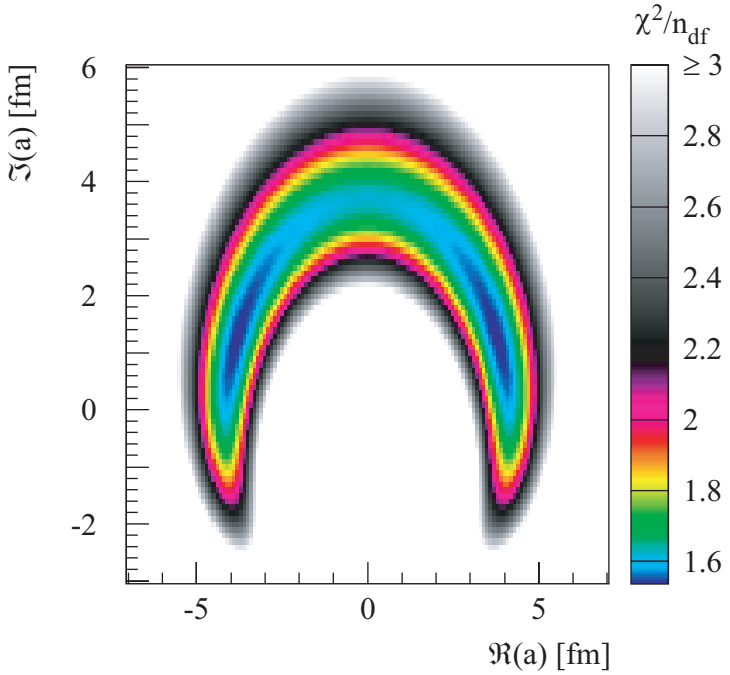

Figure 5.4 Fit of the scattering length in the strong η–^{3}He FSI model approach to all available data from threshold up to the COSY-11 Q = 10.8 MeV measurement. While the real and imaginary parts are binned in 0.1 fm intervals, the amplitude f_B is fitted and the corresponding χ^2/n_{df} is plotted on the z-axis. For a better visualization the range of the z-axis is limited to values below 3. The inner dark (blue) areas correspond to the the best χ^2 values.

Although pure s-wave scattering was found to be valid up to excess energies in the range between 11 and 15 MeV, it is interesting to note that the s-wave prediction is able to describe the shape of the excitation function even for higher excess energies up to at least Q = 40 MeV, corresponding to $p_\eta \approx 1$ fm^{-1}. This might indicate a dominance of s-wave production even at these high energies. For more quantitative informationon the contribution of higher partial waves, measurements with either a polarized beam or target or both are required. Such measure-menments are scheduled at COSY [100].

Despite the good description of the shape, the curve does not fit perfectly the SPES-II/IV or the COSY-11 data, because of a discrepancy in the absolute scale of the extracted total cross sections. This might be attributed to the normalization discrepancy when combining any of the data sets. Only the COSY-11 and WASA/PROMICE data, which are not so close to threshold,

are in agreement in the absolute scale of the extracted absolute cross section and production amplitude. Whereas the COSY-11 and the SPES-IV data, that are rather close to threshold, only agree within the error bars. Nevertheless, the observed shape of the COSY-11 data strongly supports the predictions for a very strong final state effect and rule out the reaction model proposed by COSY-GEM.

In Fig. 5.4, the results of the fitting procedure are presented in a topological view, showing the direct correlation of the real and imaginary parts and the restriction to only extract the absolute value of the real part of the scattering length (Eq. 5.5) but not its sign. Presented is the χ^2/n_{df} (z-axis) for the fit to the data, as function of the $\Re(a)/\Im(a)$ combinations within the selected range ($\chi^2/n_{df} < 3$). This presentation allows direct insight into the uncertainty of the fit to the data. In [102] the η–^{3}He scattering length was extracted using only the data from [1], [2], yielding $|\Re(a)| = 4.3 \pm 0.3$ fm and $\Im(a) = 0.5 \pm 0.5$ fm. Within the uncertainty of the fitting procedures, these values agree with the scattering length extracted from the extended data base that included the COSY-11 results.

5.5 Comparison to photoproduction data

Another hint that the observed excitation function is determined in large part by an FSI effect can be obtained by comparing the results presented in Fig. 5.3 with photoproduction data for γ ^{3}He $\rightarrow$ ^{3}He η (Fig. 5.5).

Such measurements have been carried out [103], investigating the excitation function from a few MeV above threshold up to the highest WASA/PROMICE excess energies. When scaled arbitrarily to fit the lower energy points to the scattering-length-fit curve to the proton deuteron data, the shape of the excitation function is consistent with the close-to-threshold data and with the η–^{3}He FSI description.

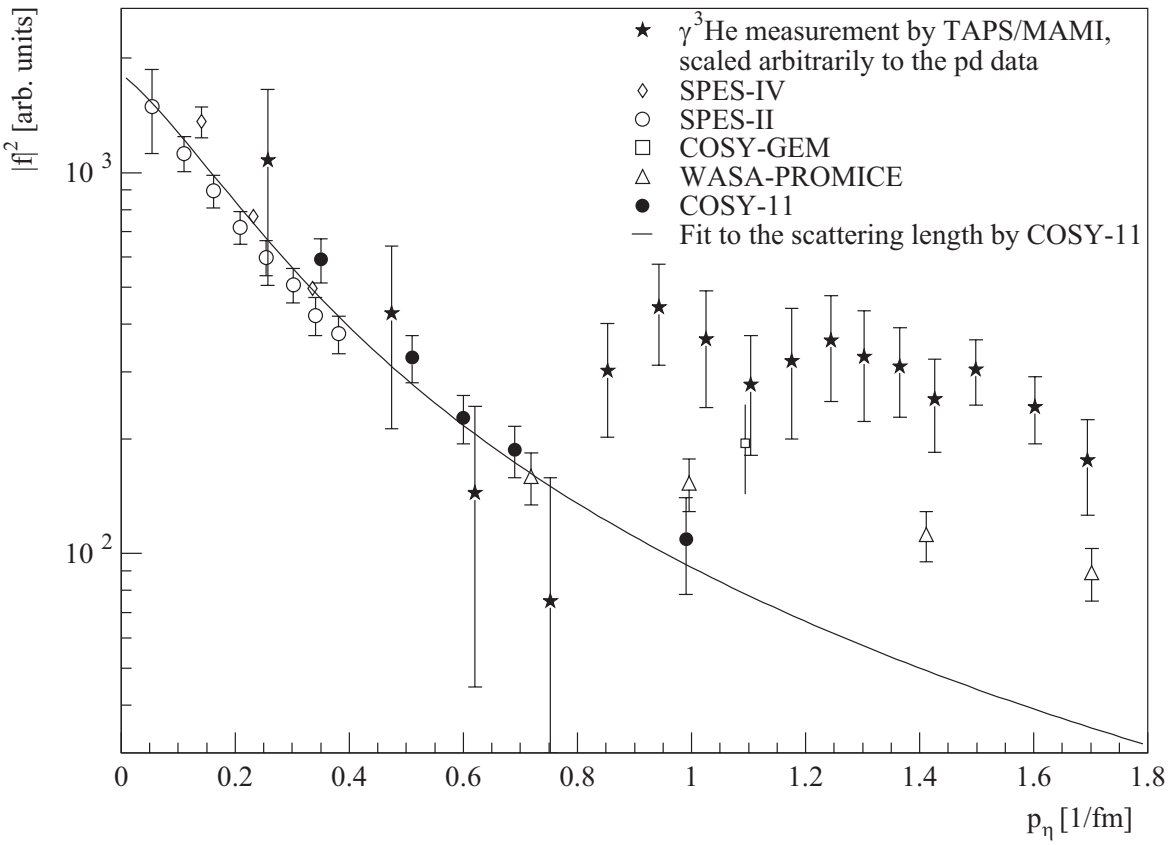

Figure 5.5 Squared absolute production amplitude for the η–^{3}He final state in $\gamma\,^3$He- and pd-collision. The photoproduction data (stars) have been scaled arbitrarily to fit the proton deuteron data at $p_\eta < 0.8$ fm^{-1}.

The photoproduction data [103] reveal an enhancement in the excitation function, as indicated at a lower level by theWASA/PROMICE data [19]. However, when moving on to higher excess energies ($p_\eta > 0.8$ fm^{-1}), the different underlying production processes also have to be taken into account. This enhancement might be taken as an indication for an η bound to a ^{3}He, where the real part of the scattering length would have to become relatively large and negative to allow for such a state [104]. However, the sign of the real part of the scattering length is not directly accessible, and the experimental data are not sufficient yet to draw final conclusions, from these $\gamma\,^3$He measurements alone.

The limited statistics in [103] leave an ambiguity in the results that makes them compatible with zero [105] and therefore does not allow the differentiation between a bound or a virtually bound state [106]. Even when combining all the available data from different reaction processes that produce the η, as has been done in [103], there are still no constraints in their interpretations of the data that allow the extraction of the sign of $\Re(a)$.

6 Conclusion and Outlook

Measurements of η meson production in proton-deuteron collisions have been performed using the COSY-11 facility at COSY (Jülich). Results on total and differential cross sections for the $pd \rightarrow {}^3He\,\eta$ reaction have been obtained at five excess energies between Q_η = 5.0 and Q_η = 40.6 MeV. This measurement closes the gap between earlier measurements very close to threshold up to Q_η= 6 MeV, carried out by SPES-II and -IV experiments at Saturne in Saclay and measurements by COSY-GEM (Q_η= 49.3 MeV) and WASA/PROMICE above Q_η= 21.7 MeV. The angular distributions extracted as part of this work show a transition from an almost isotropic emission close to threshold, as observed in the SPES-II measurements, to a highly anisotropic distribution at higher excess energies, as first observed by COSY-GEM. The total cross sections reveal a strong η–^{3}He final state interaction, corresponding to a scattering length of $|\Re(a)| = (4.2 \pm 0.5)$ fm and $\Im(a) = (0.4 \pm 1.9)$ fm.

At the SPES-IV and SPES-II spectrometers at the Saturne laboratory, the η-production cross section close to the $pd \rightarrow {}^3He\,\eta$ reaction threshold revealed remarkable features. In addition to the unexpectedly large cross section for this channel, which is in the order of that of $pd \rightarrow {}^3He\,\pi^0$, the excitation function has a maximum very close to the production threshold. The production amplitude then drops significantly with increasing energy within only a few MeV, which is in complete contrast to expectations based upon phase space. Furthermore, the center-of-mass angular distributions of the η mesons emitted near threshold were reported to be consistent with s-wave production and exhibit no major contributions from higher partial waves. This behavior differs from the corresponding data on the π^0-production cross section, where a strong p-wave contribution is present even very close to threshold.

In order to describe this near-threshold behavior, a classical two-step mechanism was proposed by Kilian and Nann. Quantum mechanical calculations by Fäldt and Wilkin within this model succeeded in reproducing the square of the production amplitude at threshold to within a factor of 2.5. To achieve this level of accuracy, they had to include a strong η–^{3}He final state interaction (FSI) into their model calculation, to describe the observed rapid drop of the production amplitude with increasing energy.

The measurements, performed at a higher excess energy of Q ~40 MeV by the COSY-GEM collaboration, yielded a highly nonisotropic angular distribution. The two-step/FSI description for the close to threshold data significantly underestimated the value of the total cross section for that measurement. Therefore, a different reaction mechanism, based on the excitation of the $N^*(1535)$ resonance has been suggested. However, that model prediction, scaled to fit the

COSY-GEM data point, failed to reproduce the observed shape of the previously determined excitation function in the near-threshold region.

Studies carried out by the WASA/PROMICE collaboration at η excess energies between Q ~22 MeV and Q ~120 MeV, yielded anisotropic angular distributions for all the measurements, in agreement with the GEM results. However the total cross sections determined in that measurement can neither be described by the η–^{3}He FSI nor the predicted shape of the resonance model excitation function.

With the data presented in this work, covering the range of intermediate excess energies, the gap between the previous data sets is closed. This enables further experimental and theoretical studies to improve the model description of the underlying production processes in the $pd \rightarrow {}^3\mathrm{He}\,\eta$ reaction. The resonant production mechanism could be ruled out as a result of this work, supporting the presence of a final state effect. The two-step process model calculations however require additional work to be done.

6.1 Conclusion of this work

The data presented in this work clearly support a strong effect of the η–^{3}He FSI and confirm a strong decrease of the production amplitude $|f|^2$ with increasing excess energy in the region below 20 MeV. Furthermore, an overall fit to the available data below 11 MeV excess energy allows one to extract information on the real and imaginary parts of the scattering length. However, the data, especially in the near-threshold region, are not sufficient to determine with high precision both the real and imaginary parts. This leads to the conclusion that extraction of the η–^{3}He scattering length with high accuracy from the excitation function requires very precise near-threshold data from a single experimental facility. Such additional measurements have been performed recently at COSY [107], [108] and their results have been published in [109], [110], respectively.

Furthermore, it is seen that up to now, none of the theoretical models can describe the excitation function over the whole range of measured beam momenta. A two-step model approach, such as that in [96] for higher excess energies, when combined with a final state refinement [6] to account for the special energy dependence in the near-threshold region is a promising candidate for a comprehensive description of the excitation function. Further theoretical and experimental work in this field will be of great value.

6.2 Outlook on more recent experiments and results

The newer results of COSY-11 [109] and ANKE [110] are excellent examples of studies, leveraging the presented results as well as the new experimental opportunities. With the availability of a deuteron beam at COSY, improved and advanced studies have been caried out, extending the results on the pd $\rightarrow$ ^{3}He η reaction presented here.

Both experiments are using the inverse kinematics reaction dp $\rightarrow$ ^{3}He η, making use of the higher luminosity now available with the deuteron beam. This further enables them to use the continous beam energy ramp technique, changing the deuteron beam momentum slowly during the storage cycle. It is therefore possible to extract several excess energy measurements (COSY-11: 19, ANKE: 195) in the off-line analysis according to the precision of the beam energy determination and the luminosity of the experiment.

COSY-11 thereby measured over an excess energy range corresponding to
$Q_\eta = -9.7$ ... $+9.5$ MeV and ANKE covers $Q_\eta = -5$ ... $+11$ MeV.

With both experiments including subthreshold measurements into their range of choosen beam momenta, subtraction of physical background to the ^{3}He η reaction is no longer subject to a priori knowledge on the underlying reaction processes, nor the use of phase space Monte Carlo simulation, as recommended in Sec. 4.1.2.2, but out of the scope of this work.

Furthermore, with the high number of data points provided especially by the ANKE measurment, the request in Sec. 6.1, to have high precission data from a single experimental facility, is fullfilled. The ANKE measurement enables to extract not only a high precission excitation function with nearly 200 independent measurements at an accuracy of 9 keV in the determination of the excess energy, but also enables to perform a reliable fit to the η–^{3}He scattering length, as suggested in Sec. 6.1. This reveals an enormous real part $|\Re(a)| = 10.7 \pm 0.8$, that largely masks any effects arising from the imaginary part $\Im(a) = 1.5 \pm 2.6$ of the scattering length [110], however the sign of the real part remains inaccessible due to the type of experiment, as discussed in Sec. 2.1.5 [10]. Additionally with the high statistics measurement of differential cross sections, ANKE determines a contribution from higher partial waves to the production process (i.e. a non-flat angular distribution) already as low as $Q_\eta = 4$ MeV.

The latter result is consistent with the COSY-11 analysis presented in [109] finding deviations from pure s-wave behaviour in the range of $Q_\eta = 3$ MeV. The scattering length analysis of COSY-11 in [109] reveals no such strong real part of the scattering length, with fitted values of $|\Re(a)| = 2.9 \pm 0.6$ and $\Im(a) = 3.2 \pm 0.4$. While the imaginary part of both extractions is in agreement, within the cited uncertainties they differ significantly in the real part.

As pointed out in Sec. 6.1, in this case the richer data set of ANKE enables for a more accurate analysis.

To improve the experimental database even further, additional polarized measurements have been proposed to be carried out only at ANKE [100], as COSY-11 finished its experimental program. Besides the close to threshold polarized measurements, ANKE also analyses high statistics data for the higher energy region at Q= 15, 20, 40, 60 MeV [111].

The η-meson stays subject of several experimental and theoretical analyses and even the η-mass is still open for debate, resulting in yet another ANKE η-measurement [112].

References

[1] J. Berger et al., Phys. Rev. Lett. 61, 919 (1988).

[2] B. Mayer et al., Phys. Rev. C 53, 2068 (1996).

[3] Berthet et al., Nucl. Phys. A 443, 589 (1985).

[4] J.-F. Germond and C. Wilkin, J. Phys. G: Nucl. Part. Phys. 15, 437 (1989).

[5] K. Kilian and H. Nann, Particle Production Near Threshold, AIP Conf. Proc. 221, 185 (1990).

[6] G. Fäldt and C. Wilkin, Phys. Lett. B 354, 20 (1995).

[7] M.A. Pickar et al., Phys. Rev. C 46, 397 (1992).

[8] G. Fäldt and C. Wilkin, Nucl. Phys. A 587, 769(1995).

[9] J.D. Bjorken and S.D. Drell, Relativistic quantum mechanics, McGraw-Hill, New York (1964).

[10] C. Wilkin, Phys. Rev. C 47, 938 (1993).

[11] M. Goldberg and K.M. Watson, Collision theory, Wiley, New York (1964).

[12] M.A. Beg, Ann. Phys. 13, 110 (1961).

[13] G. Fäldt, Nucl. Phys. A 333, 357 (1980).

[14] M. Betigeri et al., Phys. Lett. B 472, 267 (2000).

[15] J. Banaigs et al., Phys. Lett. B 45, 394 (1973).

[16] W.-M. Yao et al. (Particle Data Group), J. Phys. G 33, 1 (2006) and 2007 partial update for the 2008 edition.

[17] E. Loireleux, Doctoral Thesis Universite Paris, Orsay (1990).

[18] T. Kirchner, Doctoral Thesis Universite Paris, Orsay (1993).

[19] R. Bilger et al., Phys. Rev. C 65, 44608 (2002).

[20] H.-H. Adam et al., Phys. Rev. C 75, 014004 (2007)

[21] A. Kupsc, AIP Conf. Proc. 950, 165 (2007).

[22] A.H. Rosenfeld, Ann. Rev. Nucl. Part. Sci. 25, 555 (1975).

[23] S. Sakata, Prog. Theor. Phys 16, 686 (1956).

[24] C. Caso et al. (Particle Data Group), Eur. Phys. Journal C3, 1 (1998) and 1999 partial update for edition 2000 (URL: http://pdg.lbl.gov).

[25] M. Gell-Mann, The Eightfold Way: A theory of strong interaction symmetry (1961).

[26] A. Pevsner et al., Phys. Rev. Lett. 7, 421 (1961)

[27] P.L. Bastien et al., Phys. Rev. Lett. 8,11416(1962).

[28] C. Amsler et al. (Particle Data Group), Phys. Lett. B 667, 1 (2008).

[29] P. Moskal, PhD. thesis, Jagellonian University Krakow, Berichte des FZ-Jülich; Jul-3685, 1998.

[30] Q. Haider and L. C. Liu, Phys. Lett. B 172, 257 (1986).

[31] L. C. Liu and Q. Haider, Phys. Rev. C 34, 1845 (1986).

[32] G. L. Li, W. K. Cheng and T. T. S. Kuo, Phys. Lett. B 195, 515 (1987).

[33] H. C. Chiang, E. Oset and L. C. Liu, Phys. Rev. C 44, 738 (1991).

[34] S. Wycech, A. M. Green and J. A. Niskanen, Phys. Rev. C 52, 544 (1995).

[35] S. A. Rakityansky et al., Phys. Lett. B 359, 33 (1995).

[36] S. A. Rakityansky et al., Phys. Rev. C 53, 2043 (1996).

[37] K. Tsushima et al., Phys. Lett. B 443, 26 (1998).

[38] R. S. Hayano, S. Hirenzaki, A. Gillitzer, Eur. Phys. J. A 6, 99 (1999).

[39] Q. Haider and L. C. Liu, Phys. Rev. C 66, 045208 (2002)

[40] R. Bhalerao and L. C. Liu, Phys. Rev. Lett. 54, 865 (1985).

[41] A. M. Green and S. Wycech, Phys. Rev. C 71, 014001 (2005).

[42] P. Moskal et al., Phys. Rev. C 69, 025203 (2004).

[43] S. D. Bass and A. Thomas, http://xxx.lanl.gov/abs/hep-ph/0507024.

[44] S. S. Wu and T. T. S. Kuo, Nucl. Phys. A 430, 110 (1984).

[45] R. E. Chrien et al., Phys. Rev. Lett. 60, 2595 (1988).

[46] V.B. Belyaev and J. Wrzecionko, Sov. Journal of Nucl. Phys. 28, 78 (1978).

[47] P.A.M. Guichon, Phys. Lett. B 200, 235 (1988).

[48] K. Saito, K. Tsushima, A.W. Thomas. Nucl. Phys A 609, 339 (1996).

[49] B.D. Serot and J.D. Walecka, Adv. Nucl. Phys. 16, 1 (1986).

[50] O. Morimatsu and K. Yazaki, Nucl. Phys. A 435, 727 (1985).

[51] W. Oelert et al., COSY Proposal No. 11, IKP-KFA (1988).

[52] R. Maier, Nucl. Instr. and Meth. A 390, 1 (1997).

[53] H. Dombrowski et al., Nucl. Phys. A 626, 427c (1997).

[54] M. Rook, Dissertation, Universität Bonn, Berichte des FZ Jülich; Jül-2922, 1994; ISSN 0944-2952.

[55] M. Rook, Diploma thesis, Universität Köln, Berichte des FZ Jülich; Jül-2407, 1990; ISSN 0366-0885

[56] COSY-11 Collaboration, Annual Report, IKP FZ Jülich, 1996 (unpublished), p.38.

[57] P. Moskal et al., Nucl. Instr. & Meth. A 466, 488 (2001).

[58] P. Wüstner, Doctoral Thesis Universität Bochum, 1998.

[59] G. Schepers, Doctoral Thesis Universität Münster, 1998.

[60] W. Bräutigam et al., European Particle Accelerator Conference, Proc. EPAC88, Rome, 317 (1988).

[61] A. Khoukaz, private communication and A. Täschner, Doctoral thesis in preparation

[62] C. Quentmeier, Diploma Thesis Universität Münster, 1997.

[63] A. Khoukaz et al., Eur. Phys. J. D 5, 275 (1999).

[64] C. Thomas, Diploma Thesis Universität Münster, 1998.

[65] T. Rausmann, Diploma Thesis Universität Münster, 2006

[66] J. Otte, Diploma Thesis Universität Münster, 2007

[67] S. General, Diploma Thesis Universität Münster, 2008

[68] A. Khoukaz, Diploma Thesis Universität Münster, 1992.

[69] G. Charpak, Journ. de Phys. 30, C2-86 (1969).

[70] A. H. Walenta et al., Nucl. Instr. & Meth. A 376, 373 (1971).

[71] B. Gugulski et al., KFA-IKP(I)-1992-3 Jülich, 1992.

[72] S. Brauksiepe et al., Nucl. Instr. & Meth. A 376, 373 (1996).

[73] G. F. Knoll, Radiation detection and measurement, 3rd edition New York: John Wiley & Sons, Inc., 1999.

[74] T. Sefzick, Annual Report, IKP FZ Jülich, Jul-4052, 2002.

[75] R. Bröders et al., Annual Report IKP-KFA 1992, 397 (1993).

[76] P. Moskal, Jül-2825 Jülich, 1993.

[77] G. Anton et al., Nucl. Inst. & Meth. A 310, 631 (1991).

[78] M. Wolke, Jül-2825 Jülich, 1993.

[79] M. Köhler et al., Jül-3071 Jülich, 1995.

[80] K. Zwoll et al., IEEE Trans. Nucl. Sci. 41(1), 37 (1994).

[81] M. Drochner, Doctoral Thesis Jül-3218, 1996.

[82] M. Wolke, Doctoral Thesis Universität Bonn, 1998.

[83] C. Caso et al. (Particle Data Group), Particle Physics Booklet July 1998.

[84] WebElements^{2000}, the periodic table on the WWW (http://www.shef.ac.uk/chemistry/web-elements/webelements/elements/text/isot/He.html), link no longer exists.

[85] H.-H. Adam, Diploma Thesis Universität Münster, 2000.

[86] GEANT-detector description and simulation tool, CERN Program Library Long Writeup W5013, CERN, 1211 Geneva 23, Switzerland.

[87] P. Moskal et al., J. Phys. G 32, 629 (2006).

[88] P. Moskal et al., Phys. Lett. B 517, 295 (2001).

[89] P. Moskal, M.Wolke, A. Khoukaz, W. Oelert, Prog. Part. Nucl. Phys. 49, 90 (2002).

[90] P. Moskal et al., http://xxx.lanl.gov/abs/nucl-ex/0507033.

[91] L. Lyons, Statistics for nuclear and particle physicists, Cambridge University Press, 1986

[92] E. Gülmez et al., Phys. Rev. C 43, 2067 (1991).

[93] N. Booth et al., Phys. Rev. D 4, 1261 (1971).

[94] E. Coleman et al., Phys. Rev. 164, 1655 (1967).

[95] E. Winkelmann et al., Phys. Rev. C 21, 2535 (1980).

[96] M. Stenmark, Phys. Rev. C 67, 034906 (2003).

[97] M. Stenmark, private communication, 2005.

[98] P. Moskal et al., Phys. Lett. B 474, 416 (2000).

[99] B. Krusche, Acta Phys. Polonica B 27, 3147 (1996).

[100] A. Khoukaz, private communication, COSY-Proposal #157 (2006)

[101] S. Eidelman et al., Phys. Lett. B 592, 1 (2004).

[102] A. Sibirtsev et al., Eur. Phys. Journal A 22, 495 (2004).

[103] M. Pfeiffer et al., Phys. Rev. Lett. 92, 252001 (2004).

[104] V. Baru et al., Phys. Rev. C 68, 035203 (2003).

[105] A. Sibirtsev et al., Phys. Rev. C 70, 047001 (2004).

[106] C. Hanhart, Phys. Rev. Lett. 94, 049101 (2005).

[107] J. Smyrski et al., COSY Proposal No. 99 (2001).

[108] A. Khoukaz et al., COSY Proposal No. 137 (2004).

[109] J. Smyrski et al., Phys. Lett. B 649, 258 (2007).

[110] T. Mersmann et al., Phys. Rev. Lett. 98, 242301 (2007).

[111] A. Khoukaz, private communication and T. Rausmann, doctoral thesis in preparation

[112] A. Khoukaz, private communication and COSY-Proposal #187 (2006)

List of Tables

List of Figures

Acknowledgements

At last, I would like to say just *Thank You!* to all of those, who helped one way or the other, that this work has finally been finished. I specially thank all the people I might have forgotten to mention in the following few sentences.

I owe a great debt to Prof. Rainer Santo for his generous support, allowing me not only to work at the Institut für Kernphysik (IKP) and the Forschungszentrum Jülich (FZJ), but also to participate in international conferences and workshops and most crucially to finish this work, although the experiment, analysis and publication are almost at a distant past now.

I am also greatly indebted to Priv.-Doz. Dr. Alfons Khoukaz for his continued support and interest in finishing these studies over the past years and especially finalizing this work, well beyond the publication of the results in a journal.

I thank all the colleagues, who are no longer at IKP Münster, but who introduced me into all the secrets of cluster targets, COSY-11 and the process of data analysis: Dr. Thomas Lister and Dr. Christoph Quentmeyer.

For the excellent working conditions at the IKP in Münster, I would like to thank Dr. Norbert Lang, Dr. Timo Mersmann, Siegfried Steltenkamp, Alexander Täschner and all the other members of the large then Santo, now Wessels group.

For the countless number of pleasant stays at our experiments in Jülich, I would like to thank the COSY-11 and ANKE collaborations. Specifically I would like to thank Dr. Magnus Wolke, Dr. Pawel Moskal, Dr. Thomas Sefzick, Dr. Peter Winter, Dr. Peter Wüstner, Dr. Georg Schepers, Dr. Dieter Grzonka, Dr. Jurek Smyrski and Prof. Walter Oelert, who made each stay a nice and valuable excursion from the daily work in Münster. Without their indispensable help nothing would have gone into the first place at COSY-11.

I would like to thank the COSY-crew for providing such an excellent beam for the experiment and Prof. Colin Wilkin, Dr. Marten Stenmark and Dr. Christoph Hanhart for their contributions, fruitful discussions and support during the preparation of the publication preceding this work.

Beside my colleagues at IKP and FZJ, I also would like to thank all the people at *my other institute*, who give me „a home“ for so many years already.

I had and have the extraordinary luck to work together with Dr. Wolfgang Zierau, who offers me every degree of freedom I need to get any work done, let it be physics or *real work*.

The other person I have had the great pleasure to work together with was Dr. Richard Glasow, whose seamingly endless experience and knowledge was the greatest source of inspiration, not only when thinking about the next generation of IT. Even more, when dreams are put into reality by hard work.

Additionally I would like to thank Thomas Bauer for taking over all the *little things*, that I normally spend most of my time for.

I acknowledge the support me and my colleagues have received for carrying out these and other studies by the European Community - Access to Research Infrastructure Action of the Improving Human Potential Programme (Hadron-Physics, contract number RII3-CT-2004-506078), of the FFE grants (41266606 and 41266654) from the Research Centre Jülich, of the DAAD Exchange Programme (PPP-Polen), of the Polish State Committe for Scientific Research (grant No. 2P03B07123 and PB1060/P03/2004/26), and of the RII3/CT/2004/506078 - Hadron Physics-Activity - N4:EtaMesonNet.

I acknowledge the support of the IVV Naturwissenschaften and Zentrum für Informationsverarbeitung for providing the computational power, expertise and supporting infrastructure to run all the necessary analyses and calculations on the Tru64 UNIX servers in and outside the IKP. Furthermore providing the Windows, Mac and Linux tools necessary to make the results of the experiment presentable in publications, talks and this work.

Finally I would like to thank the two most important people in my life:

My mother, without her support I would have, besides the obvious, never had the opportunity to follow any of my studies nor other plans and projects in- and outside of the university.

Petra, whose love and patience I very much appreciate.

I can't change the laws of physics.
Scotty from Star Trek – The Original Series, Episode „The Naked Time"